2011-12-01

A Search for and Characterization of Young Stellar Objects in N206, An H II Complex in the Large Magellanic Cloud

Tabitha Christi Buehler
Brigham Young University - Provo

A Search for and Characterization of Young Stellar Objects in N206, An H II Complex in The Large Magellanic Cloud

Tabitha Christi Buehler

A dissertation submitted to the faculty of
Brigham Young University
in partial fulfillment of the requirements for the degree of

Doctor of Philosophy

Dr. Denise C. Stephens, Chair
Dr. Eric G. Hintz
Dr. Benjamin Taylor
Dr. J. Ward Moody
Dr. David Allred

Department of Physics and Astronomy

Brigham Young University

December 2011

ABSTRACT

A Search for and Characterization of

Young Stellar Objects in N206,

An H II Complex in

The Large Magellanic Cloud

Tabitha Christi Buehler

Department of Physics and Astronomy

Doctor of Philosophy

I have identified 51 young stellar object candidates in N206, an H II complex in the nearby Large Magellanic Cloud galaxy. Using archival images from the *Spitzer Space Telescope*, supplemented with other infrared and optical images, I located point sources in this region. I distinguished possible young stellar objects based on their spectral energy distributions, morphologies, and locations in color-magnitude space. I classified the young stellar object candidates based on their likelihood of being young stellar objects and based on their apparent evolutionary stages. The spatial distribution of these young stellar object candidates in N206 indicates that star formation is being triggered in a giant molecular cloud in the region.

Keywords: star formation, young stellar objects, Large Magellanic Cloud

ACKNOWLEDGMENTS

There are so many people to acknowledge and thank: my advisor, Dr. Denise Stephens, for her example, help, and guidance; Dr. Eric Hintz for having his office door open to a freshman interested in astronomy; Dr. Benjamin Taylor, for his wisdom and humor; Dr. Mike Joner, for the opportunities he has given me and the things I have learned from him; Dr. Jeannette Lawler, for her good sense of reality and her willingness to work with me; Dr. J Ward Moody for his good advice and words of encouragement. I would also like to thank Dr. You-Hua Chu, Dr. Robert Gruendl, and Dr. Rosie Chen for giving me a chance and collaborating with me in my research. Thanks to all of my committee members and others who have read drafts and made suggestions along the way.

I thank my colleagues and friends in the department that I have worked with over the years, particularly Dr. Kathleen Moncrieff, alongside whom I have had the distinct privilege of working throughout my academic career thus far.

I thank my family: my dad, Joseph Fels Bush Jr., for instilling his love of learning in me; my mom, Georgeanne Bush, for always believing in the best in me; my sister, Jessica Bush, for always being a good friend and encouraging me; and my brother, Joey Bush, for always making me feel more awesome than I actually am.

I especially thank my husband and best friend, David Buehler. I learn so much from him and feel his love and support every day. I dedicate this thesis to him.

Lastly, I acknowledge that all light and truth have a Divine source:

"For the word of the Lord is truth, and whatsoever is truth is light, and whatsoever is light is Spirit, even the Spirit of Jesus Christ." (Doctrine and Covenants 84:45)

Contents

List of Figures

Chapter 1

Introduction

Why do we study star formation? Stars are a fundamental part of the observable universe. Most of the dense matter in the universe is in the form of stars, and there is great variety among these stars.

The star-formation process plays a role in many areas of astrophysics. On a relatively small scale, the formation of planets and planetary systems is directly linked to the process of star formation. There is much effort going into searching for extra solar planets right now, particularly habitable planets, which may only be possible in orbit around stars of certain masses. We can better understand, then, where we might find habitable planets if we know under what conditions stars of different masses form.

Star formation is also tied to studies of the interstellar medium (ISM). Gravitational collapse converts gas and dust in the ISM into stars. When massive stars are formed, they produce strong stellar winds and outflows that alter their environments. These outflows can compress more gas and dust to form further stars or they can disperse interstellar clouds, possibly halting the formation of future, lower-mass stars. Stars create heavier elements from the gas and dust that created them, and they release these elements into the ISM through winds, planetary nebulae, and supernovae, enriching their surrounding environments. These

enriched materials can then go on to form the next generation of stars.

On an even larger scale, the content, structure, and dynamics of galaxies are affected by the star-formation process. Star-formation rate and history are key components in the evolution of a galaxy. The star formation histories of galaxies at different redshifts are being studied now in an effort to more fully constrain the possible geometry and future expansion of the universe. It is foundational, then, from planetary studies to cosmology, to understand how stars form.

Through identifying and characterizing young stellar objects, along with the remaining material from which they are forming, we can address several questions in star-formation theory development. On a local scale these questions involve small-scale star-formation efficiency, the impact of the local environment on star formation, and identifying which mechanism(s) are triggering star formation in a region. To understand star formation on this scale, we can start by studying the physical parameters of forming stars in their environments. Each star has a set of physical parameters that uniquely define the star: temperature, mass, luminosity, metallicity, outflow, etc. Determining these parameters for a group of forming stars allows us to better understand the conditions under which different types of stars form. Combining several small-scale star formation studies can also answer more global questions, such as how much of an effect local star formation triggering has over large scales, or how star formation is affecting the overall structure and evolution of a galaxy.

It has recently become possible to study individual, small-scale star-forming regions outside of our Galaxy, specifically in the Large Magellanic Cloud (LMC), a nearby galaxy. This is due to the capabilities of the infrared *Spitzer Space Telescope* [3] and to the close proximity of the LMC. *Spitzer* overcomes a couple of challenges to observing individual star-forming regions. One of these is that a young stellar object (YSO) that is going to evolve into a Solar-mass star typically starts out as an object 0.1 parsec in diameter [4]. This requires high-resolution observations, especially if the observations are of forming stars in another

galaxy. These objects are emitting primarily in infrared wavelengths which inherently yield poorer resolution than shorter wavelength, visible light. The turbulence in Earth's atmosphere makes angular resolution even poorer, and the atmosphere also blocks large portions of the infrared spectrum between 1 and 40 microns. From space, a telescope is able to overcome much of this. The proximity of the LMC helps to make it possible to study individual star-forming regions there; it is relatively nearby, technically within the boundaries of our own Galaxy. The LMC is also advantageously tilted to our line-of-sight so that we can basically see across the whole galaxy, something we can't do across the Milky Way. This allows for a more global view of star formation across an entire galaxy.

The LMC is an interesting place to study star formation, because it is very different from our own Galaxy. The LMC has a significantly lower proportion of heavy elements than the Milky Way, and its mass is only about one tenth of the mass of our Galaxy. The LMC is an irregular galaxy, which means that it does not have a regular shape or symmetric structure. Our Galaxy has a spiral structure, and the spiral arms are created by density waves that travel around the Galaxy's center. These spiral density waves also induce much of the star formation in our Galaxy, but these are absent in the LMC, so there are different mechanisms triggering most of the star formation there. With the help of *Spitzer*, we can now study individual star-forming regions in this nearby galaxy which is very unlike our own.

In this thesis, I utilize data taken by the *Spitzer Space Telescope*, supplemented by data from other telescopes, to identify and characterize young stellar objects in a star-forming region in the LMC called N206. I identify and present 51 candidate young stellar objects in N206 along with estimates of some of their different properties such as mass, temperature, and age. Most of these candidate young stellar objects have not previously been identified. I also show how the spatial distribution of these YSO candidates in N206 illustrates the star-formation history of the region and supports previous theories of how star-formation can be triggered in such a region.

Chapter 2

Background: Star Formation and the Large Magellanic Cloud

2.1 Star Formation

Star formation begins with a self-gravitating cloud or clump of gas and dust. Something disrupts this cloud and causes it to begin to collapse under the influence of its own self-gravity. It is still not well understood how a self-gravitating cloud becomes gravitationally unstable. The models that attempt to approximate a collapsing cloud are very complex; therefore, theories for how star formation is induced are still being developed and are not very definitive. Several authors, including Larson (1981) [5], Blitz & Williams (1999) [6], and Elmegreen & Scalo (2004) [7], report observations of structures found moving at supersonic speeds inside of giant molecular clouds (GMCs). Possible external mechanisms for driving these supersonic motions are shocks from OB associations (groups of young, blue, massive stars), shocks from galactic spiral density waves, and shocks from Type II supernovae [8]. It may be these supersonic motions in the GMCs that drives the collapse that begins the star-formation process.

Gravity is the driving mechanism in the collapse of giant gas clouds that begins the star-formation process. There are several forces that can act against gravity to disperse the cloud and keep it from collapsing, including thermal turbulence and magnetism. According to the Jeans theory, cloud collapse happens when the gravitational force overcomes these dispersive forces. A simple case in the Jeans theory involves basic potential and kinetic energies. If the potential energy of the cloud is more than twice the kinetic energy, the cloud collapses. If the kinetic energy is greater, the cloud expands or disperses. The most basic criterion for star formation to occur, then, is that the mass of the collapsing cloud must be larger than the Jeans mass. Without the influence of magnetic fields, the Jeans mass is found with Equation 2.1:

$$m_J \approx 1.4 \times 10^{-10} (T^{1.5}/\rho^{0.5}) M_\odot \tag{2.1}$$

where T is temperature, ρ is density, and $M_\odot$ is Solar masses [8].

Almost all star formation occurs in GMCs [9], which are usually found in the arms of spiral galaxies. Figure 2.1 shows a picture of the "Pillars of Creation", a part of a molecular cloud in the Eagle Nebula in our Galaxy. Molecular clouds have opacities that don't allow many ultraviolet photons to penetrate them; therefore, they are primarily made of hydrogen (H_2) molecules. Molecules made up of heavier elements are also in the clouds, and these are mostly involved in the heating and cooling mechanisms going on inside these clouds. GMCs have masses that range from about 10^5 to 10^6 $M_\odot$, and they can be larger than 10 pc across. The temperatures of these clouds usually range from about 10-100 K. Ortega et al. (2004) [10] say that molecular clouds that form stars tend to be inhomogeneous and irregularly shaped. They have density gradients in them, and the stars form in the denser areas. Small structures with masses of a few Solar masses or less have been found embedded in these clouds. These are protostellar cores at a very early stage of star formation in the clouds.

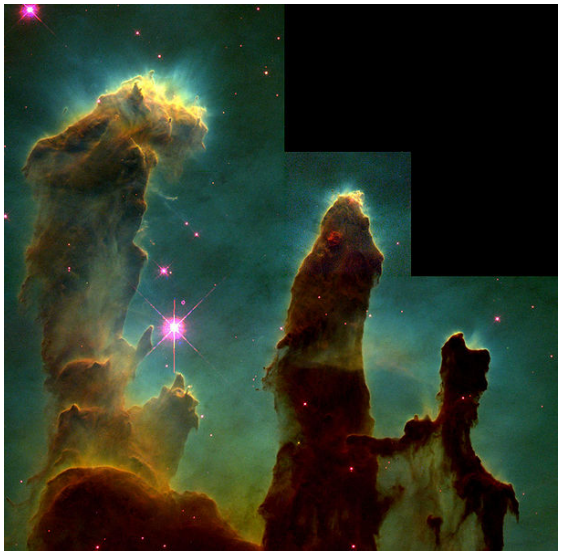

Figure 2.1 "The Pillars of Creation" in the Eagle Nebula. Imaged by the *Hubble Space Telescope.*

Many studies are being done in order to gain greater understanding of the dynamic behavior and fragmentation of GMCs. There are different ideas about what could cause the gravitational instabilities that trigger cloud-collapse. There are theories that specify both internal and external triggers. Internal cloud-collapse triggers include feedback from star formation inside the clouds [7]. External triggers include galactic spiral shock waves and shock waves from supernovae [8].

2.2 Young Stellar Objects

A young stellar object (YSO) is a star in its earliest stage of evolution. YSOs are collapsing fragments of molecular clouds that are accreting mass and are on their way to becoming stars.

YSOs include protostars, which are still gravitationally collapsing and are still accreting a lot of mass, and pre-main-sequence stars, which have finished accreting most of the mass that they will have as main-sequence stars, but are not yet fusing hydrogen to helium in their cores. YSOs are large and luminous, but they are relatively cool, so they are emitting light primarily in the infrared. Additionally, YSOs are still surrounded by dust cocoons that they are forming in, and this heated dust emits in the infrared. YSOs, therefore, exhibit an infrared excess, which means that when we look at the light coming from them, we see more infrared light than we would see coming from a normal star, such as our Sun. We learn the most about YSOs, then, by observing them at infrared wavelengths (∼1-100 microns).

The basic model for how a YSO evolves involves three components of the object: a central source, a gravitationally infalling envelope, and a protostellar disk [4]. Initially, a YSO is surrounded by a large accreting envelope that has bipolar cavities. A disk forms around the central source due to the collapse of the envelope and the rotation of the object [11]. The envelope dissipates over time as the bipolar cavity opening angle increases, and the central source eventually is exposed. The envelope clears, leaving the central source surrounded by the disk, also called a protoplanetary disk, or proplyd [2]. Figure 2.2 shows a few such proplyds that have been imaged in the nearby Orion Nebula. This disk is also eventually dispersed, leaving behind the star only.

2.3 The Large Magellanic Cloud

The Large Magellanic Cloud (LMC) is an irregular galaxy about 50 kpc away from the center of the Milky Way [12]. The LMC has three main components: a bar, a thick disk, and an outer halo, as seen in Figure 2.3. The bar is asymmetric, located near the center of the galaxy's disk and made up of older and younger stars. The bar may be offset from the plane of the disk by about 2 kpc [13] [14]. The disk of the LMC has stellar and gaseous

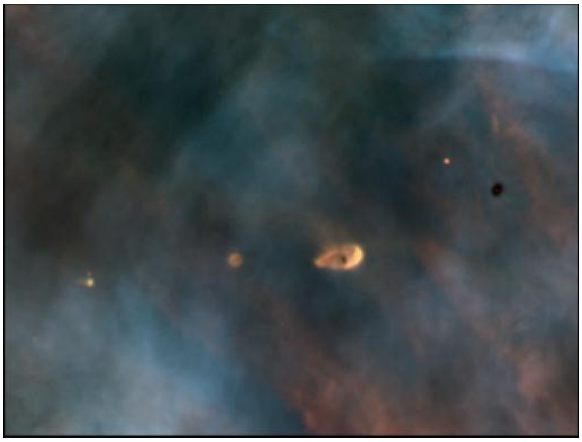

Figure 2.2 Proplyds imaged in the Orion Nebula by the *Hubble Space Telescope.*

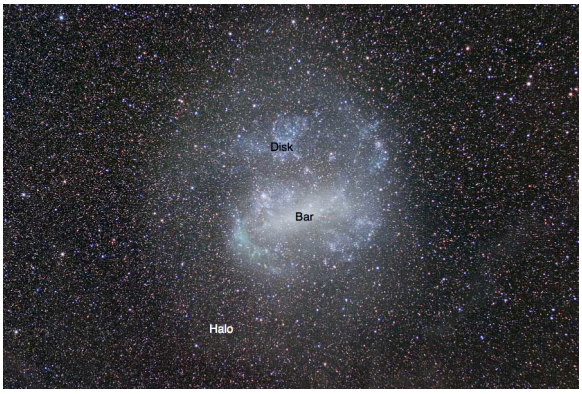

Figure 2.3 The Main Components of the Large Magellanic Cloud. Image credit and copyright Yuri Beletsky (ESO)

components, is elongated toward the center of the Milky Way galaxy, and is tilted 35 degrees to your line of sight. The gas component of the disk has several asymmetric features. The outer halo of the LMC contains mainly hot gas and older stars [15] [16].

The structure of the LMC may be due largely to tidal interactions with the Milky Way galaxy and the Small Magellanic Cloud (SMC), another nearby irregular galaxy. The Magellanic Clouds are inside the halo of the Milky Way, and the three may have been a "triple system" for at least 1 Gyr [15]. The Magellanic Clouds may be gravitationally bound to the Milky Way, or they may be making their first passage by our Galaxy [17]. Regardless, the

LMC is traveling through the halo of our Galaxy, with its eastern side leading. Numerical simulations of gravitational interactions among the Magellanic Clouds and the Milky Way are able to produce the LMC structure containing a bar, disk, and halo from an initial thin disk with no bar [15] [18]. There is an elongated region in the southern part of this leading side that is aligned along the border of the stellar disk and has a higher density than surrounding regions. Mastropietro et al. (2008) [16] suggest that the increased density along this leading edge is produced by a ram pressure that is being induced on the disk of the LMC as it travels through the hot gas in the halo of the Milky Way.

2.3.1 Star Formation Distribution and Triggers Across the LMC

Star formation regions seem to be distributed unevenly across most of the disk of the LMC. The highest concentration of star formation in the LMC is found at the southeastern edge of the disk, the edge that is leading the movement of the LMC through the Milky Way's halo. The largest single star-forming region, 30 Doradus (also known as NGC 2070) is located here. The highest concentration of young star clusters is found here, as reported by Glatt et al. (2010) [17]. Most of the other star-forming regions in the LMC are located near 30 Doradus. Some star-forming regions are found in the bar of the galaxy, and others are asymmetrically distributed throughout the disk, with no seemingly clear pattern [16].

Tidal interactions with the Milky Way and the SMC may be responsible for the current star-formation activity we observe in the LMC. Clusters of stars can be produced by strong shock compressions due to interactions among galaxies. The star-formation rate then decreases when the galaxies move apart. If galaxies repeatedly interact, this can cause observable episodes or epochs of star formation [17]. In the Magellanic Clouds, a correlation between star-formation epochs and encounters among the galaxies has been suggested by Girardi et al. (1995) [19], Pietrzynski & Udalski (2000) [20], and Chiosi et al. (2006) [21], among others.

Star formation may be triggered in the LMC by a bow shock that is compressing the leading edge of the LMC disk because of its movement through the hot gases in the halo of the Milky way. This has been suggested by deBoer (1998) [22]. Blondiau et al. (1997) [23] indeed find that the pressure on the southeastern edge of the disk of the LMC is ten times greater than the average pressure in other areas of the LMC. Additionally, Mastropietro et al. (2008) [16] use simulations to confirm that this pressure could produce the high amounts of star formation seen on this edge of the disk.

If this bow shock is a dominant mechanism for star-formation triggering, groups of stars should get older in the direction of the rotation of the LMC's disk. This is because the material compressed at the front should move to the side over time as the disk rotates, with the youngest stars at the leading edge on the southeast border of the disk. There is evidence for a progression in star formation along the disk in several objects along the outer eastern and northern edges of the LMC. These show a progression in age along the edge of the disk in a clockwise direction. Grebel & Brandner (1998) [24], who study the recent star-formation history of the LMC using supergiant stars, confirm that most of the recent star-formation (in the last 30 Myr) is concentrated on the eastern border of the disk, but they suggest that the bow shock theory cannot explain the inhomogeneous distribution of other star-formation regions across the disk.

One possible explanation for the other star-formation across the disk comes from Bekki & Chiba (2005) [15], who suggest a close interaction between the two Magellanic Clouds about 20 Myr ago.They say that this interaction would also have formed the bar in the LMC. Mastropietro et al. (2008) [16] point out, however, that perturbations in the old stellar disk should be visible due to this interaction, but that these are not observed. Through their simulations, Mastropietro et al. (2008) [16] find that compression perpendicular to the disk produces instabilities locally and clumpy structures with high-density star-forming regions. Because these structures would be inhomogeneously distributed, they could lead to

the uneven star formation seen across the LMC disk.

Another possible mechanism causing the uneven star formation across the LMC disk is called stochastic self-propagating star formation (SSPSF). This model was originally proposed by Mueller & Arnett (1976) [25]. In the SSPSF model, star formation is triggered in regions due to shock waves. These shock waves, as discussed in Section 2.1 can be produced by strong stellar winds and by supernovae. If SSPSF is the main mechanism for triggering star formation in the different regions of the LMC, we would see obvious gradients in the ages of stars in these regions, with younger stars on the edges of the regions and older stars in the centers. These small scale gradients have been reported in LMC star-forming regions by Chen et al. (2009) [2] and Romita et al. (2010) [26]. In 30 Doradus, the largest star-forming region in the LMC, many supergiant shells of H I gas have been found that are interlocked [27]. Smaller shells have formed along the rims of the supergiant shells, which is expected if the SSPSF model is dominating [28].

2.3.2 Star Formation History of the LMC

In the LMC, two main periods of star cluster formation have been observed: one that occurred more than 9 Gyr ago and one that occurred about 3-4 Gyr ago. It is thought that no star clusters formed in the time between the two main periods of star formation [29] [30] [31]. Star clusters have been continuing to form over the past 4 Gyr or so [17].

More recent periods of enhanced star cluster formation have been found in the LMC by different authors. Three such periods have been found at around 7 Myr, 125 Myr, and 800 Myr ago by Pietrzynski & Udalski (2000) [20] and Girardi et al. (1995) [19]. Two periods of enhanced star formation that occurred in both the LMC and the SMC at the same time, around 125 and 160 Myr ago, have been found by Glatt et al. (2010) [17]. Model calculations of the interactions between the LMC, SMC, and Milky Way show that the last close interaction between the LMC and SMC happened about 100-200 Myr ago [15]. Since

the star-formation rate in the LMC would increase when it closely encounters the SMC, the increase in star cluster formation found by Glatt et al. (2010) [17] around 100-200 Myr ago may have been triggered by a tidal interaction between the two galaxies [32] [15] [17]. The more recent peaks in star formation, however, may have another trigger. The current star-formation rate for the LMC is reported to be 0.19 solar masses per year by Whitney et al. (2008) [33] and 0.26 solar masses per year by Kennicutt et al. (1995) [34].

2.3.3 Searches for Young Stellar Objects in the Large Magellanic Cloud

Recent surveys have increased the number of probable YSOs in the LMC by a factor of more than 50. Recent star-formation surveys to identify YSOs in the LMC vary in their intensity and focus. The most prominent surveys have searched the entire LMC using a narrow range of parameters to identify only those objects with the highest probability of being YSOs. These large-scale surveys include one performed by Whitney et al. (2008) [33] that found 1197 probable YSOs as part of *Spitzer's* Surveying the Agents of a Galaxy's Evolution (SAGE) Legacy program [35]. Another survey performed by Gruendl & Chu (2009) [1] found 1172 YSO candidates across the LMC, many of which overlap with those found by the Legacy program. Previous to these two studies, fewer than 20 YSOs were known in the LMC.

These two large-scale surveys yield slightly different results. The contaminant elimination criteria used by Gruendl & Chu (2009) [1] reveal that 20-30% of the YSOs found by Whitney et al. (2008) [33] were probably background galaxies. Additionally, the analysis performed by Gruendl & Chu (2009) [1] allowed them to include sources that are not strictly point sources; in this way they find 850 YSO candidates that are not considered by Whitney et al. (2008) [33]. The findings of Whitney et al. (2008) [33] are biased toward intermediate-mass YSO candidates, while the findings of Gruendl & Chu (2009) [1] are biased toward

intermediate- and high-mass YSOs.

The main differences between these two large-scale surveys, as reported by Gruendl & Chu (2009) [1], are first, that Gruendl & Chu (2009) [1] include point sources that are in complex stellar environments, such as areas with multiple point sources. They also include sources in complex interstellar environments, such as sources that are superposed on diffuse dust emission. Finding these YSOs is attributed to using less-stringent criteria for identifying point sources. Secondly, Gruendl & Chu (2009) [1] determine with their criteria that 20-30% of the probable YSOs reported by Whitney et al. (2008) [33] were probably background galaxies. And, lastly, the survey done by Whitney et al. (2008) [33] probably includes more evolved and fainter YSOs than the Gruendl & Chu (2009) [1] survey. This is because of the different criteria used by each search to select initial YSO candidates.

A more detailed study to find YSO candidates within a smaller star-forming region was performed by Chen et al. (2009) [2]. They search for YSO candidates in N44, an H II region in the LMC. H II regions are regions of ionized hydrogen in the ISM that are associated with star formation. Ultraviolet light from recently-formed massive O and B stars ionizes the surrounding hydrogen gas. These are usually associated with the molecular clouds that the young O and B stars were formed from.

The same initial YSO candidate selection criteria are used by both Chen et al. (2009) [2] and Gruendl & Chu (2009) [1] but since they were looking at a much smaller region, Chen et al. (2009) [2] were able to go through the point sources more individually, making their search less automated. Doing so, they found 60 probable YSOs in N44, while Whitney et al. (2008) [33] found 19, and Gruendl & Chu (2009) [1] found 49. They used search criteria similar to that used by Gruendl & Chu (2009) [1], but in addition use photometry techniques that allow them to identify YSO candidates in crowded regions as well as those superposed on bright dust emission regions. They found about 10 more YSO candidates in the N44 region than are found by either Whitney et al. (2008) [33] or Gruendl & Chu (2009) [1],

including finding the ones identified by these large-scale surveys. Their findings are also biased toward intermediate- and high-mass YSOs.

More recently, Romita et al. (2010) [26] present a search for YSOs in N206, another H II region in the LMC (and the focus of the current YSO search). They use mid-and far-infrared *Spitzer* photometry from the SAGE project to identify YSOs, along with optical data from the Magellanic Clouds Photometric Survey (MCPS; [36]), near-infrared data from the 2-micron All-Sky Survey (2MASS; [37]), and data from the InfraRed Survey Facility (IRSF). They analyze the spectral energy distributions of point sources in the N206 region and identify 178 YSO candidates. This type of multi-wavelength search is time-consuming but is necessary to maximize the number of YSOs found in any given region.

2.4 H II Region N206

The H II region N206 was discovered by Karl Henize [38] in 1956 through a survey of H-alpha emission nebulae in the LMC. N206 shows signs of energetic star formation (Gorjian et al. 2004). N206 is about 210 pc x 210 pc, comparable to that of the Orion belt and sword, a region of star formation in our Galaxy where several YSOs have been found. N206 is far from the main bar of the LMC, where many star-forming regions are located. N206 is in the southern part of the LMC. N206 has four H-alpha knots associated with it and contains two OB associations. It has a supernova remnant on the eastern side and a superbubble, likely carved out by supernovae and massive stellar winds. Most of the Hα emission is coming from the eastern and southern sides of the bubble, where much of the star formation is predicted to occur.

N206 is located in an supergiant shell called LMC 9. LMC 9 (SGS 9) is a shell that is a collection of several giant Hα shells, but has no corresponding H I shell structure, which is why Book et al. (2008) [39] characterized the shell as false. This shell has almost never

shown cluster formation activity within the time period studied by Glatt et al. (2010) [17]. H I supershells are distributed from west to northwest along the periphery. The shell showing the most cluster formation activity is a region in the southeast, outside the boundary of the shell. In this region many clusters with ages between 50 and 250 Myr are found, which might be correlated with the expanding Hα and H I region. The few clusters younger than 50 Myr are located at the northeastern shell rim, which might be associated with H II regions. This shell is probably very old, because almost no young clusters are found in the shell, and barely any supergiants or Cepheids were found in the shell region because all the massive stars had already gone supernova, evolving on from the giant phases [24]. The star clusters from the sample of Glatt et al. (2010) [17] in this shell have ages between about 20 Myr to 1 Gyr, with a mean age of 170 Myr.

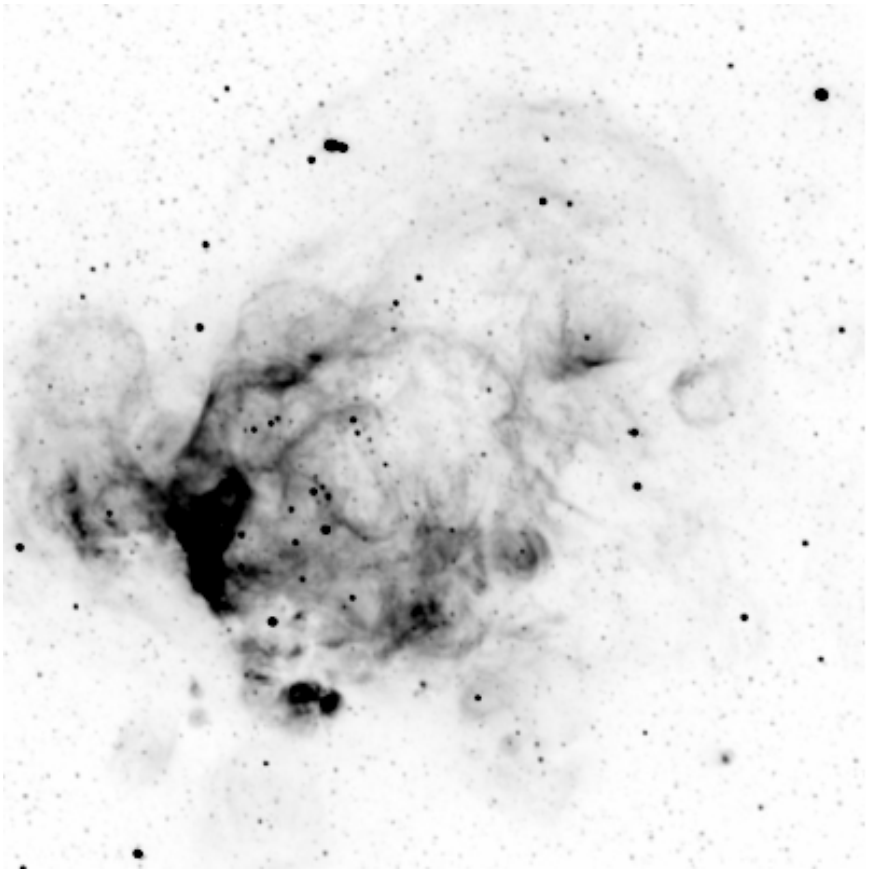

Figure 2.4 The H II region N206. Shown in Hα emission.

Chapter 3

Data: Observations and Photometry

To search for and characterize YSOs in N206, I used observations that span wavelengths from optical (0.367 μm) to radio (2.6 mm). My analysis is primarily based on mid- and far-infrared archival images of N206 that were acquired by the *Spitzer Space Telescope's* Surveying the Agents of a Galaxy's Evolution (SAGE; [35]) program. SAGE is *Spitzer* Legacy program that mapped the central 7°× 7° area of the LMC. I supplemented the *Spitzer* observations with near-infrared, optical, and radio observations from other programs. Table 3.1 gives a summary of the observations I used.

This chapter describes in detail the observations that I gathered and how I identified young stellar object candidates and measured fluxes in the observations. When I describe my use of the Image Reduction and Analysis Facility (IRAF), *routines* or *tasks* are in *italics*, PARAMETERS and PARAMETER SETS are given in ALL CAPITAL LETTERS, and **output values** in **bold type**.

Table 3.1. N206 Observation Summary

Filter Central Wavelength (μm)	Program	Principal Investigator	System	Used For
0.367 (U), 0.436 (B) 0.545 (V), 0.797 (I)	MCPS	Zaritsky	Swope/Great Circle	Photometry
0.656 (Hα)	MCELS	Smith	UM/CTIO Curtis Schmidt	Imaging
1.235 (J), 2.159 (Ks)	Illinois-TAC	Chu	CTIO Blanco/ISPI	Photometry/Imaging
3.6, 4.5, 5.8, 8.0	SAGE Legacy Program	Meixner	*Spitzer*/IRAC	Photometry/Imaging
24.0, 70.0	SAGE Legacy Program	Meixner	*Spitzer*/MIPS	Photometry/Imaging
2600 (CO)	NANTEN LMC	Fukui	NANTEN	Imaging

3.1 *Spitzer Space Telescope* Data

Until recently it was impossible to image and resolve YSOs in nearby galaxies because there is no ground-based telescope sensitive enough in the infrared to image and resolve such faint objects. Either the Earth's atmosphere blocks the needed infrared wavelength or the background noise is so high that an adequate signal-to-noise ratio is never achieved. This was overcome with the launch of the *Spitzer Space Telescope* in 2003.

The *Spitzer Space Telescope* is an Ritchey-Chrétien reflecting telescope with an 85-cm diameter primary mirror [40]. *Spitzer* is aboard a spacecraft in an Earth-trailing orbit. Out in space, the instruments on *Spitzer* are capable of imaging YSOs in neighboring galaxies over a wide range of infrared wavelengths, from 3-8 microns and at 24, 70, and 160 microns. This wavelength range gives *Spitzer* the capability of directly imaging YSOs in the near- and mid-infrared (∼1-10 microns), where the gas and dust that conceal these objects has the smallest impact on the transmitted light. *Spitzer* is also sensitive to the light emitted by the dust that still surrounds these YSOs. This dust scatters and absorbs much of the ultraviolet and visible light emitted by the YSOs and re-emits that light at longer wavelengths

(∼10-100 microns). With *Spitzer's* InfRared Array Camera (IRAC; [41]) and its Multiband Imaging Photometer (MIPS; [42]), we can, for the first time, image and resolve YSOs in the neighboring LMC at these wavelengths.

3.1.1 IRAC Observations

IRAC is a camera made up of four detector arrays; in essence it is four cameras. Each detector array is an impurity-band-conduction (IBC) infrared detector that obtains images in one channel, or wavelength. The four channels, at mid-infrared wavelengths of 3.6, 4.5, 5.8, and 8.0 μm, obtain images simultaneously. These four channels have central wavelengths of 3.56, 4.52, 5.73, and 7.91 μm, respectively, and bandwidths of 0.75, 1.01, 1.42, and 2.93 μm [41]. The channels are paired ([3.6 μm] with [5.8 μm] and [4.5 μm] with [8.0 μm]) to image two "nearly adjacent" fields that are 5.2 × 5.2 arcminutes in size. The two shorter wavelength channels use indium antimonide (InSb) detectors, while the longer wavelength channels use silicon arsenic (Si:As) detectors. Each of the four detectors has 256 × 256 pixels and a plate scale of 1.2 arcseconds per pixel [41]. The IRAC images have ∼2 arcsecond angular resolution.

The IRAC observations I used were in the *Spitzer* data archive provided by SAGE. Images were acquired in all four IRAC bands in the high dynamic range mode, which means that each observation consisted of two exposures, one long and one short. I found archival IRAC observations that imaged areas of N206 at six different times, with a short (0.4 seconds) and a long (10.4 seconds) exposure of the region each time. This gave me a total of 48 IRAC images (12 in each channel). The IRAC images were processed through the Spitzer Science Center (SSC) pipeline, and I used the post-Basic Calibrated Data (post-BCD) images in this study.

3.1.2 Locating Infrared Point Sources

The first step in my search for YSOs in N206 was to locate infrared point sources in the region. I required the YSO candidates to be sources with measurable flux values in the [4.5 μm] and [8.0 μm] bands, due to the color-magnitude selection criteria described in Section 4.1. I therefore first identified point sources in the 4.5 μm images using the IRAF routine *daofind*. *Daofind* is an automated routine that uses sets of user-specified parameters to detect objects in an image. The parameter sets that I used in *daofind* are called DATAPARS and FINDPARS. The DATAPARS parameters I set for use in locating point sources were FWHMPSF and SIGMA. The FINDPARS parameters that I set were THRESHOLD, SHARPLO, SHARPHI, ROUNDLO, and ROUNDHI.

DATAPARS are the data dependent parameters. FWHMPSF is the full-width at half-maximum (FWHM) of the point spread function of stars in an image. I used the IRAF task *imexamine* to measure the average FWHM of stars' radial profiles and to measure the standard deviation values for the background sky in the [4.5 μm] images. I used a FWHMPSF value of 3 pixels and a SIGMA value of 0.01 MJy/sr for finding point sources in all of the [4.5 μm] images.

FINDPARS are the object detection parameters. THRESHOLD is the minimum value (in multiples of SIGMA) from DATAPARS required for a detection to be considered a source. SHARPLO and SHARPHI are low and high limits for the image sharpness statistic which is used to avoid including counts that are due to bad pixels instead of real point sources. Similarly, ROUNDLO and ROUNDHI are low and high limits for the image roundness statistic which attempts to avoid including counts that are due to bad rows or columns instead of real point sources. To determine the FINDPARS parameters, I ran *daofind* on the [4.5] μm images with different sets of values for these parameters, adjusting the parameters to find the combination that would yield the largest number of reliable sources and the lowest

number of false detections. The most effective set of parameters was THRESHOLD = 10 SIGMA, SHARPLO = 0.5, SHARPHI = 1.4, ROUNDLO = -0.9, and ROUNDHI = 0.9.

Using these sets of parameters in *daofind*, I located point sources in all 12 of the [4.5 μm] images. To make the final list of [4.5 μm] point sources, I used a C program to combine each of the 12 lists into one list, with a criterion of coincidence of 2.4 arcseconds (2 pixels), so that two sources from two different lists would be counted as the same source if they were within 2.4 arcseconds of each other. The resulting [4.5 μm] list contained 14,609 point sources.

3.1.3 IRAC Photometry

I then measured the [4.5 μm] fluxes of the point sources in this master list using aperture photometry. I used the IRAF routine *phot* to perform the photometry. *Phot* takes user-specified parameters and outputs flux values for a set of user-selected sources in an image. Besides DATAPARS, I used two other parameter sets utilized by *phot*: PHOTPARS and FITSKYPARS. The PHOTPARS parameter I set is APERTURES. In FITSKYPARS, I set the parameters ANNULUS and DANNULUS.

PHOTPARS contains the photometry parameters. APERTURES is the radius in pixels of the aperture, or circle set around an object in an image, to measure its flux. When a detector is obtaining an observation, photons will hit the detector in different pixel locations. Each photon will be converted into one or more electrons that are counted and then converted digitally into "counts" that reflect the original photon incidence. The task *phot* adds up the "counts" that it detects within a specified aperture and reports it as **sum**. I set APERTURES to 3 pixels (3.6 arcseconds) for measuring 4.5 μm fluxes.

The set FITSKYPARS contains the sky fitting parameters. These are for measuring the background "count" values that are compared to the point source "count" values. ANNULUS gives the inner radius in pixels of an annulus that *phot* uses to measure this background

value, and DANNULUS gives the width of this annulus, in pixels. The ANNULUS and DANNULUS values were 3 and 4 pixels, respectively. These values are suggested by the IRAC Data Handbook for measuring the flux of a point source with a 3-pixel aperture. This means that the background measuring annulus went from 3 to 7 pixels (3.6 to 8.4 arcseconds) out from the central source being measured.

I used these parameters to run *phot* to measure the [4.5 μm] flux values of the 14,609 sources. The output values for each point source that were gathered from *phot* were **flux**, **area**, and **stdev**. *Phot* computes **flux** according to Equation 3.1, where **sum** is the total number of "counts" found in the specified aperture, **area** is the area of the aperture in square pixels, and **msky** is the background "count" value per pixel (found with the annulus). The output value **stdev** is the standard deviation of the sky value. From running *phot* on the 12 IRAC [4.5μm] images, I retrieved 12 sets of **flux**, **area**, and **stdev** values for the point sources.

$$\textbf{flux} = \textbf{sum - area} \times \textbf{msky} \tag{3.1}$$

Due to the way the IRAC images were calibrated, the output **flux** values from *phot* are given in units of MJy/sr, but I wanted them in Jy for my analysis. Table 5.1 in the IRAC Data Handbook provides the conversion factors FLUXCONV and CALFAC for each IRAC channel. FLUXCONV is used to convert between MJy/sr and DN/s, and CALFAC is used to convert between DN/s and μJy. DN/s are digital counts per second, the count units that IRAF usually uses. The FLUXCONV value given for the [4.5 μm] channel is 0.1388 (MJy/sr)/(DN/s), and the CALFAC value given is 0.207 (DN/s)/μJy. I used these values to convert the **flux** values from MJy/sr to μJy and then converted those to Jy. To further refine the flux values, I needed to apply aperture corrections. A given aperture will only take in a certain percentage of the flux of the point source. Table 5.7 of the IRAC Data Handbook provides aperture correction values for each channel for different aperture selections. The

aperture correction value (*apcorrect*) given for the [4.5 μm] measurements made with an aperture of 3 pixels and an annulus from 3 to 7 pixels is 1.127. This value is multiplied by the measured flux to estimate the total real flux. Using these conversions and corrections, I found a corrected flux value for each point source in each image using Equation 3.2.

$$correctedflux = apcorrect \times \frac{\mathbf{flux}}{FLUXCONV \times CALFAC \times 100000} \tag{3.2}$$

I then calculated an error value for each of the corrected flux values. The corrected flux error is the quadrature combination of the error in the flux measurement and the error in the background sky measurement. To calculate the error in the measured flux, I needed to take into account the fact that it is electrons that are actually being measured in a detector. The error in the measurement is the square root of the measurement, so if it is electrons that are being counted, the measurement error goes back to the measured electrons. To take this into account, I divided each output **flux** value by the GAIN value found in the headers of the images. The GAIN value gives the electrons per "count" value. The *phot* task assumed that the counts were in the IRAF default units of DN/s, so it referred to the image exposure time also. To account for this, I multiplied by the exposure time (EXPTIME) for each image, given in seconds. This gaves a calculated error on the measured counts.

For the error in the background sky measurement, I used the **stdev** and **area** output values, as well as using FLUXCONV and EXPTIME to convert to the same units as the flux measurement error. The calculation of the total error on the values measured by *phot* are given in Equation 3.3, where σ is the photometry error.

$$\sigma = \frac{([\mathbf{F} + \mathbf{area} \times \mathbf{S}]^{1/2} \times FLUXCONV)}{exptime} \tag{3.3}$$

,

where **F** is given by Equation 3.4, and **S** is given by Equation 3.5.

$$\mathbf{F} = \frac{(\mathbf{flux} \times exptime)}{(FLUXCONV \times GAIN)} \tag{3.4}$$

$$\mathbf{S} = \frac{(\mathbf{stdev}^2 \times exptime)}{FLUXCONV^2} \tag{3.5}$$

I then aperture-corrected these errors and converted them into the units I wanted to work with (Equation 3.6).

$$correctederror = apcorrect \times \frac{\sigma}{FLUXCONV \times CALFAC \times 100000} \tag{3.6}$$

I decided to retain a flux measurement only if it was at least 2 times its corresponding σ value, leaving 14,050 point sources. I used this list of 2σ sources to continue flux measurements in the other IRAC channels.

I next performed aperture photometry using *phot* on the [8.0 μm] IRAC images with the point sources that had 2σ detections at [4.5 μm]. I used the same flux aperture and background sky annulus that I had used in the [4.5 μm] photometry. I applied aperture corrections and flux conversions in the same way as with the [4.5 μm] measurements, using the appropriate values. All of the photometric parameters used are given in Table 3.2. I also calculated a σ value for each corrected flux value and retained only the sources that had 2σ detections in both [4.5 μm] and [8.0 μm] measurements. This brought the point source count down to 10,666.

We can compare how much light an object is emitting at different wavelengths by looking at its "color". The color of an objects in this sense is the difference in its magnitudes or a ratio of its fluxes at two different wavelengths. We often analyze the colors of objects in color-magnitude diagrams (CMDs), where a color (the difference between two magnitudes) is plotted against a magnitude at one wavelength. To select my initial YSO candidates, I used a CMD that incorporates two of the IRAC channels, at [4.5 μm] and [8.0 μm]. I describe

Table 3.2. Photometry Parameters

Filter (μm)	Aperture Radius ($''$)	Sky Annulus ($''$)	Aperture Correction	Zero Point (Jy)	Assumed Flux Calibration Error(%)
J	1.8	2.1-3.0	1.105	1594	5
Ks	1.8	2.1-3.0	1.106	666.8	5
[3.6 μm]	3.6	3.6-8.4	1.124	280.9	5
[4.5 μm]	3.6	3.6-8.4	1.127	179.7	5
[5.8 μm]	3.6	3.6-8.4	1.143	115.0	5
[8.0 μm]	3.6	3.6-8.4	1.234	64.1	5
[24.0 μm]	7.0	20.0-32.0	1.61	7.14	4
[70.0 μm]	16.0	18.0-39.0	2.07	0.775	10

this color-magnitude criteria further in Chapter 4. Doing this eliminated all but 112 point sources, which I considered my initial YSO candidates. I used aperture photometry next to measure the IRAC [3.6 μm] and [5.8 μm] fluxes of these candidate YSOs, applying the same corrections and error restrictions that I had for the previous values. For all the IRAC flux values, the aperture corrections range from 12.4% to 23.4%, according to channel.

After I had finished the IRAC photometry, I had measured IRAC point source flux values in a total of 48 images, 12 in each channel. I then calculated a weighted average flux value for each of the 112 YSO candidates in each IRAC wavelength. I weighted the average flux by the inverse-square of the measurement errors, as given by Equation 3.7. In Equation 3.7, $flux_i$ are the flux values for each source to be averaged, and $weight_i$ are the weights for each flux value. The weights are given by Equation 3.8, where σ_i is the error for each flux value.

$$\bar{flux} = \frac{\sum_{i=1}^{n} flux_i weight_i}{\sum_{i=1}^{n} weight_i} \tag{3.7}$$

$$weight_i = 1/\sigma^2 \tag{3.8}$$

Additionally, I combined the errors for the flux values that were averaged, which resulted in an error for the average flux for each candidate in each IRAC channel. The combined error was computed according to Equation 3.9, where $\sigma_{f\bar{l}ux}$ is the combined flux error, and $weight_i$ are the weights, according to Equation 3.8.

$$\sigma_{f\bar{l}ux} = (\frac{1}{\sum_{i=1}^{n} weight_i})^{1/2} \tag{3.9}$$

Lastly, I converted the average flux value for each YSO candidate in each IRAC channel into a magnitude value. I did this conversion using Equation 3.10, where mag is the calculated magnitude of the source, $flux_0$ is a zeropoint flux value in Jy, provided by Table 5.1 of the IRAC Data Handbook, and $f\bar{l}ux$ is the average flux calculated in Equation 3.7.

$$mag = -2.5 \times log_{10}(f\bar{l}ux/flux_0) \tag{3.10}$$

All but one of the 112 YSO candidates had a 2σ flux value in each of the four IRAC channels; the exception did not have a 2σ value in the [3.6 μm] channel.

3.1.4 MIPS Observations

The MIPS instrument has three imaging arrays, at far-infrared wavelengths of [24 μm], [70 μm], and [160 μm], and also obtains spectra between 52 and 100 μm. I used [24 μm] and [70 μm] images for my YSO search. These two channels have bandwidths of 5 and 19 μm, respectively [42]. The [24 μm] array has 128 $\times$ 128 pixels, and the [70 μm] array has 32 $\times$ 32 pixels. The field of view for both of these channels is 5 x 5 arcminutes, yielding a plate scale of 2.45 arcseconds per pixel for the [24 μm] channel and 4.0 arcseconds per pixel for

the [70 μm] channel. The [24 μm] array is an Si:As IBC detector, and the [70 μm] array is a germanium photoconductor [42].

I used MIPS observations of N206 at [24 μm] and [70 μm] from the *Spitzer* data archives that were acquired by the SAGE program. These observations were made using the scan mapping mode at four different times, for a total of 8 MIPS images, 4 at [24 μm] and 4 at [70 μm]. In the scan mapping mode, the telescope scans the sky at a constant rate while a scan mirror moves so as to freeze an image on each array for a specified exposure time. The three channels are exposed in turn as the telescope scans the sky, and a scan is executed ten times for each of the [24 μm] and [70 μm] channels [42]. The MIPS archival images were processed through the Spitzer Science Center (SSC) pipeline, and I used the post-BCD images.

3.1.5 MIPS Photometry

I used *phot* to measure the fluxes of the initial 112 YSO candidates in the MIPS [24 μm] and [70 μm] images. For the [24 μm] photometry, I used a source aperture with a radius of 7 arcseconds ($\sim$ 2.9 pixels) and a sky annulus from 20 to 32 arcseconds ($\sim$ 8.2 to 13.1 pixels). For the [70 μm] photometry, I used an aperture of 16 arcseconds (4 pixels) and an annulus from 18 to 39 arcseconds (4.5 to 9.75 pixels) (Table 3.2).

Just as with the IRAC flux values, *phot* output the MIPS flux values in MJy/sr, and I needed them in Jy for analysis. The flux values also needed to be aperture-corrected. The MIPS Data Handbook provided me with the needed conversions and corrections. To convert from MJy/sr to μJy/arcsecond^2, I multiplied the **flux** values from *phot* by 23.5045. I then multiplied by the aperture area in pixels to get the flux into μJy. (The aperture area for the 24 μm photometry was 6.0025 pixels, and the aperture for the 70 μm measurements was 16 pixels.) I multiplied each flux value by its aperture correction, 1.61 for the [24 μm] channel and 2.07 for [70 μm]. I therefore found a corrected flux value in Jy for each of the initial 112 YSO candidates in each MIPS image using Equation 3.11.

$$correctedflux = apcorrect * \frac{(\mathbf{flux} \times 23.5045 \times \mathbf{area})}{1000000} \tag{3.11}$$

I could then calculate a flux error just as was done with the IRAC fluxes, using Equation 3.3. I similarly corrected and converted these error values using Equation 3.6.

Using the measurements that were at least a 2σ detection, I found a weighted average flux value for each point source measured in each band, given again by Equations 3.7 and 3.8. I converted the average fluxes into magnitudes using Equation 3.10 and the flux zeropoints given in the MIPS Data Handbook. Two of the 112 YSO candidates did not have 2σ flux values in the MIPS [24 μm] channel, and 24 did not have flux values at [70 μm]. These 24 include one source that did not have a [24 μm] flux value.

3.2 Supplemental Data

To increase the wavelength range of my data set, I included near-IR and optical photometry. The near-IR observations came from my collaborators Dr. You-Hua Chu and Dr. Robert Gruendl at the University of Illinois at Urbana-Champaign (UIUC). They obtained telescope time at the Cerro Tololo Inter-American Observatory (CTIO) in February 2007 and acquired some near-IR images of the N206 region. The optical photometry I included came from the Magellanic Clouds Photometric Survey (MCPS; [36]). Additionally, I have included archival images from the Magellanic Clouds Emission Line Survey (MCELS; [43]) and radio contours from the NANTEN CO survey of the LMC [44].

3.2.1 Near-IR Observations & Photometry

My collaborators obtained near-IR images of N206 in the J and Ks bands at CTIO using the Victor Blanco 4-meter telescope with the Infrared Side-Port Imager (ISPI). The ISPI camera has a 10.25 $\times$ 10.25 arcminute field of view imaged with a 2048 $\times$ 2048 pixel mercury

cadmium telluride (HgCdTe) pixel array. The array has a plate scale of 0.3 arcseconds per pixel. They obtained 2 J- and 2 K_s-band images covering parts of N206.

I performed aperture photometry for the initial 112 YSO candidate sources in these two near-IR bands, obtaining **flux** values from *phot*. For the photometry, I used an aperture with a radius of 1.8 arcseconds (6 pixels) around each source and a sky annulus from 2.1 to 3 arcseconds (7 to 10 pixels). This time, the **flux** values were output in units of mJy. The conversion to Jy and aperture correction for these ISPI flux values is given in Equation 3.12.

$$correctedflux = (apcorrect * \mathbf{flux})/1000 \tag{3.12}$$

The error calculation was also similar to the *Spitzer* error calculations, but in this case the image calibration was done by Dr. Robert Gruendl at UIUC, and he provided me with a flux conversion value (*fluxconv*) that converts between mJy/pixel and "counts". This results in Equation 3.13 for calculating the ISPI flux errors, including aperture-correcting them and converting them into Jy.

$$error = \frac{(sqrt[\mathbf{G} + \mathbf{area} \times \mathbf{R}] \times fluxconv \times apcorrect)}{1000} \tag{3.13}$$

,

where **G** and **R** are given by Equations 3.14 and 3.15.

$$\mathbf{G} = \frac{(\mathbf{flux})}{(fluxconv \times GAIN)} \tag{3.14}$$

$$\mathbf{R} = \frac{\mathbf{stdev}^2}{fluxconv^2} \tag{3.15}$$

I then computed a weighted average flux, combined error, and magnitude value for each YSO candidate with at least a 2σ detection in each of the two MIPS channels in the same way that I did for the *Spitzer* flux values.

Of the 112 YSO candidates, 17 did not have an ISPI J-band flux, and 15 did not have Ks-band flux values. Twelve candidates are in common between these two lists, having neither a J- or Ks-band flux detection.

3.2.2 Optical Photometry

The optical photometry I included came from the MCPS photometric catalog of point sources in the Large Magellanic Cloud. The observations for this survey were obtained with the Las Campanas 1-meter Swope telescope in Chile, using the Great Circle Camera and a 2048 x 2048 CCD. The plate scale of the MCPS images is 0.7 arcseconds per pixel. Reductions and photometry from this survey were performed by Zaritsky et al. (2004) [36] to provide a photometric catalog of over 1 million sources from the central 8° by 8° region of the LMC. Observations and photometry from this survey were done in the Johnson UBV filters and the Gunn I filter. I obtained MCPS optical flux values for 74 of my 112 YSO candidates from the catalog. It is not surprising that all candidates weren't found if they are very young YSOs, still not emitting in the optical. All 74 candidates found had B, V, and I flux values, and 45 had U values. Again, it is not surprising that shorter wavelength detections might be missing for these objects.

3.2.3 Supplemental Images

In order to examine the physical environments surrounding my initial YSO candidates, I obtained archival optical images of N206 from MCELS and radio contours from the NANTEN CO survey of the LMC. MCELS is a survey done by CTIO and the University of Michigain (UM)using the UM/CTIO Curtis Schmidt Telescope and an STIS 2k CCD at CTIO. The field of view for the survey is 1.1° x 1.1° with a plate scale of 2.035 arcmin per pixel and a resolution of about 3 arcseconds. The survey used Hα (656.3 nm), [S II] (672.4 nm), and

[O III] (500.7 nm) filters to locate ionized gas in the LMC [43]. I used the Hα images from MCELS to see where the ionized hydrogen gas was in the regions surrounding my YSO candidates.

NANTEN is a 4-meter radio telescope at Las Campanas Observatory in Chile. The LMC CO survey took 32,800 observations of the central $6^\circ \times 6^\circ$ region of the LMC at the 2.6-mm wavelength emission of carbon monoxide at a resolution of about 40 parsecs. The survey is sensitive to finding giant molecular clouds (GMCs) as low as about (1-2) $\times$ 10^4 $M_\odot$. The survey found 107 GMCs in the LMC that range in mass from 6×10^4 to 2×10^6 $M_\odot$. These masses are similar to the masses of molecular clouds found in our Galaxy. The observations were reduced and radio contours were made by Fukui et al. (2001) [44], outlining giant molecular clouds. I used these contours to analyze the locations of my YSO candidates with respect to the giant molecular clouds found by this survey.

Chapter 4

Analysis

4.1 Selecting Initial YSO Candidates

YSOs exhibit an infrared excess, which means that they emit more infrared radiation than we would see from "normal stars", such as main sequence stars like our Sun. This infrared excess in YSOs is due to two things. First, YSOs are cooler than the stars they will become, and cooler objects radiate more of their light at longer wavelengths than hotter objects. Secondly, YSOs are still enshrouded in differing amounts of dust, depending on how evolved they are, and this dust absorbs radiation from the central object and re-emits its own light at infrared wavelengths. Since infrared excess is characteristic of YSOs, candidate YSOs can begin to be distinguished by how much of their light they radiate at different wavelengths, specifically infrared wavelengths.

To select my initial YSO candidates, I used a color-magnitude diagram that incorporates two of the IRAC channels, at [4.5 μm] and [8.0 μm]. This CMD, shown in Figure 4.1, plots the IRAC [4.5] - [8.0] color versus the IRAC [8.0 μm] magnitude. The [4.5] - [8.0] color is the difference between the measured magnitudes at [4.5 μm] and [8.0 μm], and the magnitude scale is backwards so that brighter [8.0 μm] objects are toward the top of the diagram,

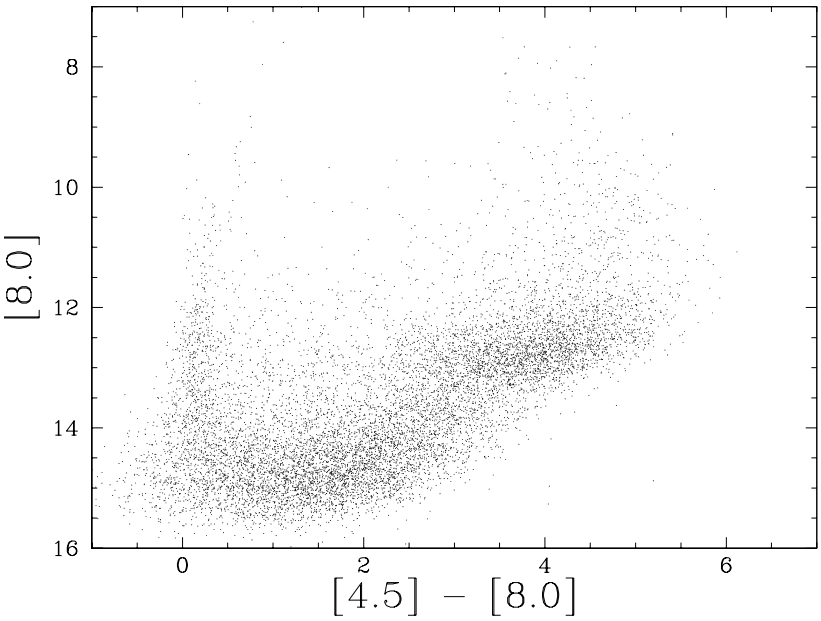

Figure 4.1 Color-magnitude diagram of IRAC [4.5 μm] & [8.0 μm] point sources. The [8.0 μm] magnitude is plotted on the ordinate, with brighter [8.0 μm] objects toward the top. Color (the difference between the [4.5 μm] and [8.0 μm] magnitudes) is plotted on the abscissa, with redder objects toward the right hand side. Units on both axes are in magnitudes.

and redder objects are toward the right hand side of the diagram. This CMD, using these wavelengths, was suggested specifically for distinguishing possible YSOs by Harvey et al. (2006) [45] and has been used by Chen et al. (2009) [2] and Gruendl & Chu (2009) [1] in their searches for YSOs in the LMC. This CMD is useful because in this color-magnitude space, different types of objects, such as normal stars, evolved stars, and background galaxies, are easily distinguishable, as described in the following sections. Plotted on the CMD in Figure 4.1 are the 10,666 IRAC [4.5 μm] and [8.0 μm] point sources I found and measured as described in Section 3.1.3.

4.1.1 Excluding Normal and Evolved Stars

So that I did not have to visually assess each of the 10,666 IRAC point sources individually, I used color-magnitude criteria to eliminate objects from this set that were likely to be other types of objects. The first objects I eliminated were normal and evolved stars. Normal stars (main-sequence, giant, and supergiant stars) do not exhibit IR excess and should not show much difference in their [4.5 μm] and [8.0 μm] magnitudes, giving colors of [4.5] - [8.0] $\approx$ 0 [45]. The main sequence stars found in my photometry are traced out by the vertical feature seen in Figure 4.1 that is located around [4.5] - [8.0] = 0 and goes from about [8.0] = 14 up to about [8.0] = 10. In this color-magnitude space, this main sequence feature is located at [4.5] - [8.0] $<$ 0.5, to the left of the blue dotted line in Figure 4.2, so I used this criterion to eliminate most probable normal stars from my list of sources.

More evolved red giant branch (RGB) and asymptotic giant branch (AGB) stars, however, will look redder than main sequence stars. RGB stars have fused their core hydrogen into helium and are fusing hydrogen in a shell outside of their non-fusing helium cores. AGB stars look similar to RGB stars externally, but they have a shell of helium fusing to carbon inside of their hydrogen fusing shell and a core of non-fusing carbon and oxygen. Both RGB and AGB stars can have powerful stellar winds. These stars can exhibit some mid-infrared excess due to infrared emission from dust in their stellar winds. Models of carbon- and oxygen-rich AGB stars in our Galaxy predict that most AGB stars will have a color of [4.5] - [8.0] $<$ 2 [46]. As mentioned in Chapter 2, the average metal (heavy element) content of the LMC is lower than that of our Galaxy, so that might lead to different predicted colors for AGB stars in the LMC. The Groenewegen (2006) [46] models, however, are based more on the abundances of carbon and oxygen that are produced by the stars than on the initial abundances that the stars were formed from.

Colors of AGB stars in the LMC still might be different than colors of AGB stars in the

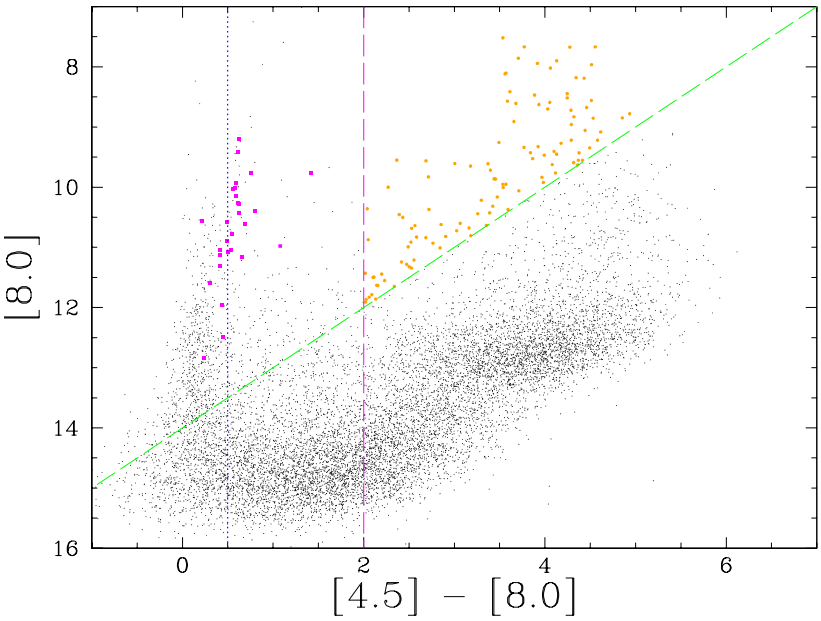

Figure 4.2 Color-magnitude diagram showing YSO candidate selection criteria. The black dots represent the IRAC [4.5 μm] and [8.0 μm] point sources found in N206. The [8.0 μm] magnitude is plotted on the ordinate, with brighter [8.0 μm] objects toward the top. Color (the difference between the [4.5 μm] and [8.0 μm] magnitudes) is plotted on the abscissa, with redder objects toward the right hand side. Units on both axes are in magnitudes. The vertical blue dotted line represents the criterion used to eliminate most "normal" stars from the sample; these stars are to the left of the dotted line. The vertical magenta dashed line represents the criterion used to eliminate both "normal" and evolved stars from the sample; these are to the left of the dashed line. The magenta squares represent the 28 known AGB stars located in the N206 region. The green dashed line represents the criterion used to eliminate most background galaxies from the sample; these are below the dashed line. The orange circles represent the initial 112 YSO candidates.

Milky Way. To check this color criterion so that I could exclude as many of these probable evolved stars as possible, I examined the CMD locations of known AGB stars in the N206 region. I found 28 known AGB stars in the field of N206 using the SIMBAD database. These stars are all carbon stars whose atmospheres contain substantial amounts of carbon. It is thought that this enriching of the atmospheres is due to carbon being pulled up from the interior through convection. I located these 28 AGB stars in the IRAC [4.5 μm] and [8.0

μm] images and measured their fluxes, applying the same corrections and conversions as in Section 3.1.3. These known AGB stars are marked as the magenta squares in the CMD in Figure 4.2, essentially tracing out the asymptotic giant branch in this diagram. These AGB stars have an [8.0 μm] magnitude range of 9.20 to 12.84 and a [4.5] - [8.0] color range of 0.21 to 1.42, which means that they do meet the Groenewegen (2006) [46] AGB color criterion of [4.5] - [8.0] < 2. I therefore adopted this criterion, shown as the magenta dashed line in Figure 4.2, to eliminate most evolved stars from my group of point sources. This criterion would also eliminate the normal stars discussed above. This criterion was also used by Whitney et al (2008) [33], Harvey et al. (2006) [45], Chen et al. (2009) [2], and Gruendl & Chu (2009) [1] to eliminate most normal and evolved stars from their samples of point sources. I do expect that I also eliminated some more evolved YSOs by using this criterion. These YSOs would be more exposed physically, surrounded by relatively little dust.

4.1.2 Excluding Background Galaxies

I also used a color-magnitude criterion to eliminate most background galaxies from my list of sources. Galaxies can show infrared excess due to their dust. My criterion for eliminating most background galaxies came from the *Spitzer* Wide-Area Extragalactic Survey (SWIRE; [47]). SWIRE was a survey that observed six fields in the sky all well out of the plane of our Galaxy, because it was designed to study the mid-infrared properties of extragalactic objects. Harvey et al. (2006) [45] and Gruendl & Chu (2009) [1] looked at the SWIRE Elais N1 data set [48] to examine the locations of the SWIRE sources in color-magnitude space. Figure 4.3 shows an IRAC ([4.5] - [8.0]) vs. [8.0] CMD, put together by Gruendl & Chu (2009) [1], of sources found by the SWIRE survey. Since the survey was done at high Galactic latitudes, the sources in this CMD are mostly foreground stars in our Galaxy and background galaxies. The main sequence stars can be seen in Figure 4.3 tracing out the vertical feature at ([4.5] - [8.0]) ≈ 0, just as in my CMD for the sources in N206. The main-

sequence feature curves toward the red at [8.0 μm] < 9 where the sources began to saturate due to the 30-second exposure time used by the SWIRE survey. The rest of the diagram is dominated by background galaxies. Harvey et al. (2006) [45] and Gruendl & Chu (2009) [1] determined that most background galaxies in this color-magnitude space can be eliminated by the color-magnitude criteria of (1) ([4.5] - [8.0]) < 0.5 and (2) [8.0] > 14 - ([4.5] - [8.0]). This is shown by the diagonal dashed line in Figure 4.3. I already excluded sources with ([4.5] - [8.0]) < 2, shown by the vertical dashed line in Figure 4.3, so I additionally adopted the latter criterion, [8.0] < 14 - ([4.5] - [8.0]) (shown as the green dashed line in Figure 4.2), as an initial attempt to exclude background galaxies from my list of YSO candidates. I expect that, using this criterion, I am also excluding low-mass YSOs from my candidates. My search is, therefore, biased toward intermediate- and high-mass YSOs.

4.1.3 Initial YSO Candidates

My final color-magnitude criteria for selecting the initial set of YSO candidates are:

(1) ([4.5] - [8.0]) > 2 and (2) [8.0] > 14 - ([4.5] - [8.0]).

These criteria are represented by the magenta and green dashed lines on the CMD in Figure 4.2. These criteria left 112 sources in this wedge of space, shown by the orange circles in the figure. Upon inspecting images of these sources, two were found to be nonreal. Images for these two "sources" are shown at [3.6 μm] in Figure 4.4. These nonreal "sources" are artifacts due to saturation of a bright source, so they were rejected and not included in the list of initial YSO candidates. The 110 remaining sources make up my initial list of YSO candidates. The measured magnitudes for these initial candidates are given in Table 4.1.3.

Table 4.1. Multiwavelength Photometry of Initial YSO Candidates

Name	Rank	U	B	V	I	J	K	Class.
(1)	(2)	(3)	(4)	(5)	(6)	(7)	(8)	(15)
		[3.6]	[4.5]	[5.8]	[8.0]	[24]	[70]	
		(9)	(10)	(11)	(12)	(13)	(14)	
052918.10-710126.76	97	— —	20.39 (0.09)	18.88 (0.06)	16.98 (0.03)	15.35 (0.03)	14.11 (0.02)	SD
		13.66 (0.03)	13.76 (0.02)	12.89 (0.12)	11.28 (0.12)	7.20 (0.05)	0.03 (0.68)	
052919.30-710134.68	96	— —	— —	— —	— —	19.51 (0.33)	17.83 (0.18)	D
		14.46 (0.34)	13.66 (0.25)	13.13 (0.13)	11.24 (0.11)	7.11(0.05)	-0.11 (0.62)	
052923.76-710214.64	91	— —	21.17 (0.11)	19.23 (0.04)	17.23 (0.03)	15.62 (0.03)	14.47 (0.03)	G
		13.34 (0.01)	13.43 (0.01)	12.41 (0.05)	10.91 (0.04)	7.50 (0.05)	— —	
052934.30-710905.40	41	— —	21.08 (0.11)	20.10 (0.05)	19.02 (0.07)	— —	— —	C II/III
		13.76 (0.01)	13.51 (0.01)	11.12 (0.01)	9.41 (0.01)	6.39 (0.02)	— —	
052934.49-710427.48	112	20.26 (0.17)	18.88 (0.04)	17.35 (0.03)	15.90 (0.03)	— —	— —	SD
		13.75 (0.01)	13.93 (0.02)	13.24 (0.09)	11.91 (0.10)	7.19 (0.05)	— —	
052935.23-710856.76	48	19.29 (0.09)	19.35 (0.10)	18.88 (0.04)	18.34 (0.04)	— —	— —	C II/III
		14.05 (0.02)	13.97 (0.02)	11.24 (0.02)	9.55 (0.02)	6.20 (0.01)	— —	
052938.38-710042.12	103	— —	— —	— —	— —	17.32 (0.07)	15.29 (0.04)	GC I/II
		14.01 (0.02)	13.60 (0.02)	12.63 (0.05)	11.50 (0.06)	6.31 (0.02)	— —	
052938.47-705520.64	34	18.43 (0.08)	19.24 (0.05)	18.38 (0.06)	18.06 (0.05)	17.16 (0.07)	16.10 (0.06)	G
		13.49 (0.01)	13.51 (0.01)	10.92 (0.01)	9.22 (0.01)	6.03 (0.01)	— —	
052938.90-705523.52	65	— —	19.21 (0.10)	17.53 (0.04)	16.11 (0.05)	15.11 (0.02)	14.14 (0.03)	SG
		13.45 (0.01)	13.49 (0.01)	11.65 (0.02)	9.95 (0.01)	6.18 (0.01)	— —	
052939.19-710439.00	102	19.44 (0.13)	18.27 (0.04)	16.91 (0.06)	15.59 (0.04)	14.46 (0.02)	13.63 (0.02)	SD
		13.41 (0.01)	13.61 (0.02)	12.58 (0.05)	11.49 (0.05)	7.30 (0.05)	— —	
052945.38-710501.68	111	— —	18.71 (0.08)	17.26 (0.04)	15.84 (0.10)	14.71 (0.02)	13.73 (0.02)	GC III
		13.75 (0.02)	13.89 (0.02)	13.65 (0.17)	11.87 (0.30)	7.14 (0.09)	— —	
052954.38-710506.36	58	19.08 (0.11)	19.97 (0.05)	19.59 (0.08)	18.72 (0.05)	17.79 (0.10)	16.59 (0.09)	C II
		14.00 (0.04)	13.88 (0.03)	11.35 (0.04)	9.76 (0.04)	5.47 (0.02)	-0.13 (0.32)	
052955.82-710503.84	56	20.12 (0.22)	18.72 (0.03)	17.08 (0.07)	15.40 (0.04)	14.17 (0.02)	13.12 (0.02)	SD
		12.65 (0.01)	12.83 (0.01)	11.28 (0.03)	9.65 (0.03)	4.33 (0.01)	-0.32 (0.28)	
052956.54-710440.08	77	18.87 (0.11)	19.22 (0.08)	19.02 (0.05)	18.07 (0.10)	16.72 (0.05)	15.05 (0.04)	CSD mult.
		13.38 (0.02)	12.85 (0.01)	11.89 (0.04)	10.45 (0.04)	5.96 (0.02)	-0.29 (0.25)	
052958.56-710844.88	62	19.67 (0.12)	19.57 (0.05)	19.16 (0.05)	19.02 (0.11)	17.48 (0.08)	15.63 (0.05)	C II

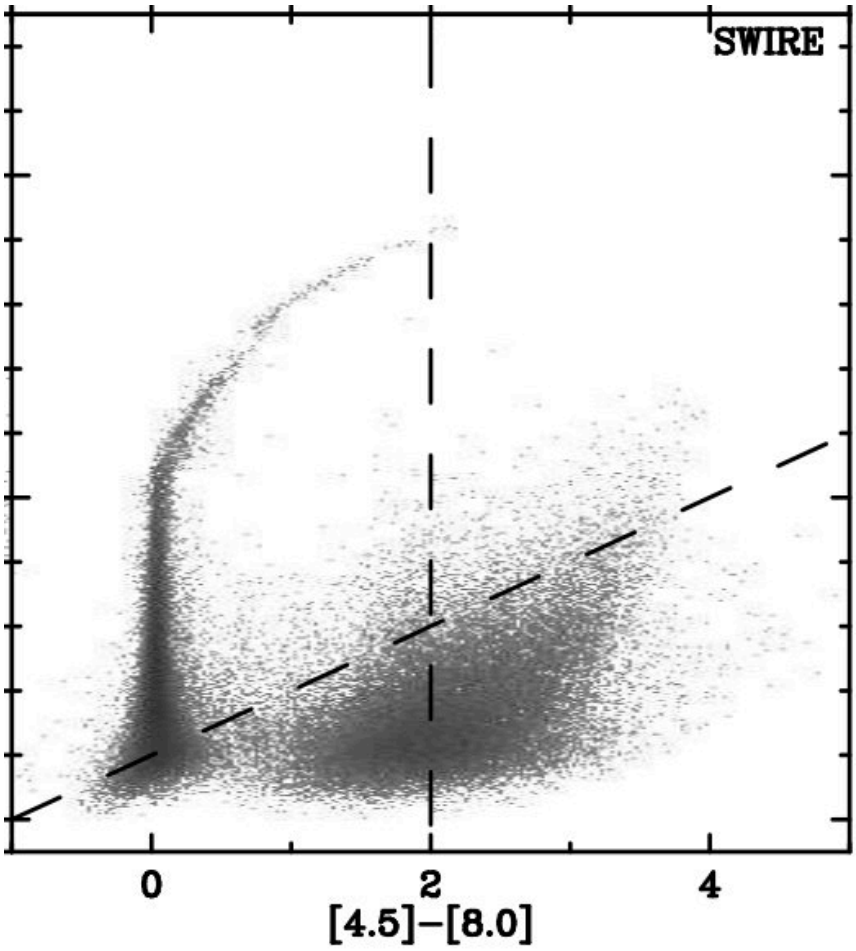

Figure 4.3 Color-magnitude diagram of IRAC [4.5 μm] & [8.0 μm] point sources from the SWIRE survey. The ordinate plots the [8.0 μm] magnitude. Most normal and evolved stars lie to the left of the vertical dashed line. Most of the objects below the diagonal dashed line are background galaxies. Figure from Gruendl & Chu (2009) [1]

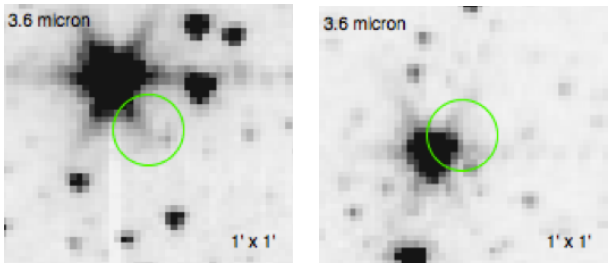

Figure 4.4 [3.6 μm] images of sources identified as nonreal. These are artifacts due to saturation of a bright source.

Table 4.1 (continued)

Name	Rank	U	B	V	I	J	K	Class.
(1)	(2)	(3)	(4)	(5)	(6)	(7)	(8)	(15)
		[3.6]	[4.5]	[5.8]	[8.0]	[24]	[70]	
		(9)	(10)	(11)	(12)	(13)	(14)	
		13.72 (0.01)	13.32 (0.01)	11.52 (0.02)	9.86 (0.02)	6.27 (0.02)	— —	
053003.96-710512.84	63	15.37 (0.06)	16.43 (0.03)	15.83 (0.13)	16.66 (0.17)	15.88 (0.04)	15.41 (0.05)	SDC II
		13.85 (0.04)	13.90 (0.04)	11.73 (0.05)	9.92 (0.04)	5.40 (0.01)	-0.48 (0.33)	
053003.98-710531.56	108	19.66 (0.16)	18.63 (0.05)	17.27 (0.03)	15.96 (0.04)	14.89 (0.02)	13.99 (0.02)	SD
		13.68 (0.01)	13.87 (0.02)	13.25 (0.06)	11.78 (0.05)	7.27 (0.09)	0.04 (0.71)	
053015.84-710758.80	84	— —	20.47 (0.09)	19.39 (0.05)	18.55 (0.06)	15.43 (0.03)	13.74 (0.02)	GC III
		13.12 (0.01)	13.21 (0.02)	12.12 (0.05)	10.68 (0.05)	6.35 (0.03)	-1.43 (0.20)	
053017.71-710742.60	74	17.29 (0.04)	17.79 (0.03)	17.40 (0.04)	16.76 (0.09)	16.23 (0.04)	15.70 (0.05)	SD
		14.38 (0.13)	13.96 (0.07)	12.00 (0.17)	10.37 (0.19)	4.21 (0.01)	-2.41 (0.12)	
053017.98-710737.92	51	18.83 (0.07)	19.21 (0.04)	18.65 (0.06)	17.70 (0.03)	16.92 (0.06)	16.36 (0.07)	SD
		13.96 (0.06)	13.91 (0.06)	11.30 (0.05)	9.59 (0.06)	4.11 (0.01)	-2.36 (0.13)	
053018.60-710800.60	72	— —	— —	— —	— —	14.40 (0.02)	12.86 (0.01)	CG I/II
		12.34 (0.01)	12.40 (0.01)	11.68 (0.03)	10.36 (0.03)	5.46 (0.01)	-2.06 (0.15)	
053019.27-710750.88	18	— —	— —	— —	— —	18.60 (0.16)	17.79 (0.16)	D
		13.39 (0.04)	13.07 (0.04)	10.36 (0.04)	8.56 (0.03)	3.23 (0.01)	-2.58 (0.11)	
053019.49-710739.72	46	— —	— —	— —	— —	— —	— —	D
		14.06 (0.08)	13.39 (0.05)	11.50 (0.09)	9.53 (0.06)	2.72 (0.01)	-2.64 (0.11)	
053019.68-710750.16	9	— —	— —	— —	— —	— —	— —	DC I
		12.51 (0.02)	12.08 (0.02)	9.79 (0.03)	8.02 (0.02)	3.00 (0.01)	-2.64 (0.11)	
053020.26-710748.00	5	— —	19.46 (0.04)	17.95 (0.08)	16.45 (0.03)	15.24 (0.03)	14.08 (0.02)	CD II/III
		12.08 (0.02)	11.56 (0.01)	9.57 (0.02)	7.86 (0.02)	2.69 (0.01)	-2.70 (0.11)	
053020.40-705430.24	59	— —	— —	— —	— —	18.39 (0.13)	16.21 (0.07)	C I/II
		13.83 (0.01)	12.54 (0.01)	11.25 (0.01)	9.83 (0.01)	4.33 (0.01)	— —	
053020.66-710738.64	7	— —	— —	— —	— —	17.18 (0.08)	15.74 (0.06)	C I/II
		12.44 (0.02)	11.86 (0.02)	9.74 (0.02)	7.94 (0.02)	2.44 (0.01)	-2.65 (0.11)	
053020.88-705408.28	83	19.52 (0.08)	17.91 (0.10)	17.17 (0.03)	15.92 (0.03)	15.00 (0.02)	14.28 (0.03)	G
		13.83 (0.01)	13.84 (0.02)	12.42 (0.04)	10.68 (0.03)	6.88 (0.03)	— —	
053021.07-710559.28	109	— —	— —	— —	— —	15.28 (0.03)	14.44 (0.03)	SD
		13.93 (0.03)	13.89 (0.03)	13.35 (0.18)	11.83 (0.25)	5.14 (0.02)	-1.34 (0.17)	

Table 4.1 (continued)

Name	Rank	U	B	V	I	J	K	Class.
(1)	(2)	(3)	(4)	(5)	(6)	(7)	(8)	(15)
		[3.6]	[4.5]	[5.8]	[8.0]	[24]	[70]	
		(9)	(10)	(11)	(12)	(13)	(14)	
053021.29-705437.44	36	— —	21.49 (0.15)	20.11 (0.15)	19.23 (0.14)	17.30 (0.08)	15.66 (0.05)	C II
		13.35 (0.01)	12.75 (0.01)	10.86 (0.01)	9.26 (0.01)	4.81 (0.01)	— —	
053021.55-705409.00	60	— —	20.44 (0.09)	20.05 (0.09)	19.37 (0.14)	18.22 (0.14)	16.66 (0.10)	C II
		13.86 (0.01)	13.80 (0.02)	11.58 (0.02)	9.84 (0.01)	6.75 (0.03)	— —	
053022.06-710751.60	70	16.81 (0.04)	17.44 (0.03)	17.25 (0.03)	16.92 (0.03)	16.80 (0.06)	16.58 (0.08)	SD
		14.23 (0.13)	13.52 (0.08)	11.89 (0.18)	10.22 (0.16)	3.06 (0.01)	-2.48 (0.12)	
053022.46-710742.96	22	— —	— —	— —	— —	18.07 (0.11)	15.80 (0.05)	C I
		13.14 (0.04)	12.56 (0.04)	10.28 (0.03)	8.63 (0.03)	2.69 (0.01)	-2.52 (0.12)	
053023.11-710556.40	3	17.63 (0.09)	18.44 (0.05)	17.86 (0.11)	17.71 (0.07)	16.49 (0.05)	15.44 (0.05)	C mult.
		12.21 (0.01)	12.22 (0.01)	9.42 (0.01)	7.67 (0.01)	3.74 (0.01)	-1.24 (0.18)	
053024.89-710823.64	86	20.21 (0.18)	18.81 (0.04)	17.48 (0.03)	16.13 (0.03)	15.16 (0.03)	14.36 (0.03)	SD
		13.82 (0.02)	13.99 (0.02)	12.44 (0.04)	10.81 (0.04)	7.03 (0.07)	-0.31 (0.56)	
053025.58-710533.36	76	20.28 (0.25)	18.65 (0.04)	17.26 (0.03)	15.87 (0.03)	14.85 (0.02)	14.00 (0.02)	SD
		13.58 (0.02)	13.70 (0.03)	12.00 (0.06)	10.44 (0.06)	6.30 (0.01)	-0.07 (0.32)	
053027.41-705421.96	81	19.20 (0.09)	19.26 (0.07)	18.96 (0.10)	18.44 (0.08)	18.17 (0.17)	17.34 (0.16)	GC II
		13.87 (0.02)	13.99 (0.02)	12.17 (0.02)	10.64 (0.02)	7.42 (0.02)	— —	
053034.37-711120.04	110	— —	18.84 (0.04)	17.38 (0.03)	16.02 (0.03)	14.84 (0.02)	14.03 (0.02)	SD
		13.82 (0.01)	13.99 (0.02)	13.09 (0.05)	11.86 (0.08)	8.52 (0.08)	— —	
053035.69-710137.20	19	17.71 (0.06)	17.99 (0.05)	17.69 (0.06)	17.20 (0.07)	16.50 (0.03)	14.93 (0.03)	C II
		12.59 (0.01)	12.16 (0.01)	10.25 (0.01)	8.57 (0.01)	5.85 (0.01)	— —	
053036.22-710646.08	85	— —	21.43 (0.20)	19.13 (0.10)	17.13 (0.03)	15.47 (0.03)	14.18 (0.02)	SDC III
		13.65 (0.02)	13.75 (0.02)	12.19 (0.05)	10.72 (0.06)	— —	— —	
053038.47-710711.64	107	20.23 (0.36)	18.76 (0.11)	17.44 (0.04)	16.11 (0.03)	15.09 (0.02)	14.29 (0.03)	SD
		13.95 (0.03)	13.99 (0.03)	12.98 (0.17)	11.65 (0.24)	6.64 (0.08)	-0.42 (0.27)	
053038.57-710934.56	106	19.05 (0.08)	18.72 (0.03)	17.84 (0.03)	17.02 (0.05)	16.46 (0.05)	16.10 (0.07)	SD
		16.00 (0.03)	13.79 (0.02)	13.22 (0.09)	11.63 (0.07)	7.38 (0.04)	— —	
053045.24-710803.84	67	— —	18.07 (0.05)	16.87 (0.05)	15.69 (0.03)	14.83 (0.02)	14.03 (0.02)	SD
		13.40 (0.03)	13.54 (0.05)	11.52 (0.05)	10.01 (0.05)	4.39 (0.02)	-2.07 (0.15)	
053045.77-710737.56	53	19.54 (0.13)	18.41 (0.03)	16.88 (0.03)	15.36 (0.03)	14.23 (0.02)	13.35 (0.02)	SD

Table 4.1 (continued)

Name	Rank	U	B	V	I	J	K	Class.
(1)	(2)	(3)	(4)	(5)	(6)	(7)	(8)	(15)
		[3.6]	[4.5]	[5.8]	[8.0]	[24]	[70]	
		(9)	(10)	(11)	(12)	(13)	(14)	
		12.81 (0.01)	12.98 (0.02)	11.30 (0.03)	9.61 (0.03)	4.72 (0.03)	-1.82 (0.14)	
053046.61-710751.60	40	— —	— —	— —	— —	18.47 (0.14)	16.89 (0.10)	CD I
		14.01 (0.09)	13.84 (0.06)	11.10 (0.07)	9.35 (0.06)	3.69 (0.02)	-1.35 (0.17)	
053046.75-710844.88	57	— —	— —	— —	— —	15.91 (0.04)	15.04 (0.04)	C mult.
		13.43 (0.02)	13.12 (0.02)	11.43 (0.03)	9.72 (0.02)	4.81 (0.01)	-0.91 (0.27)	
053047.06-710855.68	94	— —	— —	— —	— —	19.43 (0.30)	— —	D
		15.62 (0.14)	13.85 (0.03)	12.83 (0.09)	11.01 (0.06)	6.39 (0.07)	-0.79 (0.48)	
053047.16-710742.96	27	— —	— —	— —	— —	— —	— —	C I
		13.88 (0.05)	13.15 (0.03)	10.62 (0.03)	8.83 (0.03)	3.84 (0.03)	-1.98 (0.13)	
053047.71-710802.04	78	14.19 (0.04)	14.99 (0.03)	14.86 (0.04)	14.83 (0.04)	14.87 (0.02)	14.56 (0.03)	SD
		13.25 (0.04)	12.93 (0.04)	12.21 (0.14)	10.50 (0.13)	3.41 (0.01)	-2.15 (0.14)	
053047.88-710755.20	20	18.54 (0.13)	18.40 (0.07)	17.38 (0.08)	16.37 (0.04)	15.61 (0.03)	14.83 (0.03)	CD mult.
		12.88 (0.02)	12.64 (0.02)	10.25 (0.02)	8.59 (0.02)	3.58 (0.02)	-1.57 (0.15)	
053048.17-710811.76	49	— —	— —	— —	— —	— —	— —	DC I
		13.87 (0.06)	13.92 (0.08)	11.35 (0.05)	9.55 (0.04)	3.93 (0.01)	-2.08 (0.15)	
053048.79-710735.04	38	— —	— —	— —	— —	20.07 (0.38)	16.82 (0.09)	C I
		13.71 (0.05)	13.25 (0.03)	10.89 (0.05)	9.33 (0.05)	4.42 (0.04)	-1.29 (0.19)	
053049.51-710804.92	54	— —	— —	— —	— —	18.33 (0.14)	15.96 (0.06)	CD I
		13.70 (0.05)	13.70 (0.07)	11.26 (0.06)	9.62 (0.05)	3.73 (0.02)	-0.83 (0.22)	
053049.97-710722.44	69	— —	20.36 (0.16)	20.27 (0.10)	20.29 (0.23)	17.65 (0.09)	17.25 (0.12)	SD
		15.00 (0.15)	13.64 (0.24)	12.01 (0.09)	10.16 (0.07)	5.38 (0.10)	-1.20 (0.25)	
053050.23-710813.56	64	— —	— —	— —	— —	— —	17.77 (0.17)	CD I
		14.04 (0.08)	13.52 (0.05)	11.56 (0.08)	9.95 (0.08)	4.36 (0.02)	-1.96 (0.16)	
053054.02-710606.12	82	— —	18.62 (0.17)	16.16 (0.06)	15.42 (0.04)	14.24 (0.02)	13.36 (0.02)	SD
		13.08 (0.01)	13.20 (0.02)	12.09 (0.04)	10.64 (0.04)	4.92 (0.02)	-1.11 (0.19)	
053055.32-710605.04	25	— —	— —	— —	— —	18.44 (0.17)	17.14 (0.13)	D
		13.28 (0.04)	13.01 (0.03)	10.63 (0.04)	8.72 (0.03)	3.47 (0.01)	-1.03 (0.20)	
053056.23-710602.52	6	— —	— —	— —	— —	15.95 (0.04)	14.97 (0.04)	C I/II
		12.30 (0.02)	12.03 (0.02)	9.77 (0.02)	7.90 (0.02)	3.79 (0.01)	-1.33 (0.21)	

Table 4.1 (continued)

Name	Rank	U	B	V	I	J	K	Class.
(1)	(2)	(3)	(4)	(5)	(6)	(7)	(8)	(15)
		[3.6]	[4.5]	[5.8]	[8.0]	[24]	[70]	
		(9)	(10)	(11)	(12)	(13)	(14)	
053056.33-710731.08	100	— —	— —	— —	— —	— —	— —	D
		— —	13.45 (0.33)	12.38 (0.19)	11.43 (0.63)	— —	-0.22 (0.73)	
053056.59-710754.48	105	— —	— —	— —	— —	0.07 (0.42)	18.57 (0.26)	D
		16.32 (0.28)	13.77 (0.46)	13.45 (0.16)	11.63 (0.14)	5.17 (0.08)	-1.89 (0.28)	
053056.69-710603.60	4	— —	— —	— —	— —	15.42 (0.03)	15.33 (0.05)	CG I/II
		12.12 (0.02)	11.95 (0.02)	9.49 (0.02)	7.67 (0.02)	3.90 (0.01)	-1.29 (0.22)	
053056.71-710557.84	24	— —	22.01 (0.49)	20.96 (0.16)	19.72 (0.12)	18.03 (0.11)	15.08 (0.04)	C I/II
		12.93 (0.01)	12.73 (0.02)	10.54 (0.02)	8.70 (0.01)	6.39 (0.01)	-1.24 (0.22)	
053057.12-710605.04	8	15.40 (0.03)	15.29 (0.03)	15.27 (0.02)	15.13 (0.03)	15.23 (0.03)	15.05 (0.04)	CG III
		12.54 (0.01)	12.48 (0.01)	9.76 (0.01)	7.96 (0.01)	4.08 (0.01)	-1.22 (0.22)	
053104.20-710735.76	95	— —	— —	— —	— —	18.12 (0.11)	16.07 (0.06)	CSD I/II
		14.32 (0.02)	13.77 (0.02)	12.63 (0.05)	11.21 (0.06)	6.32 (0.12)	-1.08 (0.25)	
053105.11-710756.28	35	— —	— —	— —	— —	19.24 (0.24)	17.67 (0.18)	CD I/II
		13.73 (0.03)	13.80 (0.02)	10.93 (0.02)	9.22 (0.02)	5.98 (0.05)	-0.37 (0.35)	
053105.23-710709.84	98	17.66 (0.05)	17.86 (0.04)	17.34 (0.04)	16.16 (0.03)	15.08 (0.02)	14.39 (0.03)	C III
		14.04 (0.03)	13.82 (0.03)	11.56 (0.21)	11.32 (0.34)	3.81 (0.01)	-1.53 (0.16)	
053105.62-710700.48	73	— —	19.71 (0.06)	19.04 (0.05)	18.18 (0.04)	6.72 (0.05)	14.95 (0.04)	C I/II
		13.47 (0.02)	13.09 (0.01)	11.84 (0.05)	10.37 (0.04)	4.47 (0.01)	-1.47 (0.17)	
053110.18-710506.36	99	— —	19.81 (0.09)	18.28 (0.03)	16.61 (0.04)	15.20 (0.03)	14.08 (0.02)	SD
		13.76 (0.02)	13.87 (0.03)	12.88 (0.09)	11.34 (0.08)	6.32 (0.09)	-0.14 (0.68)	
053115.84-710508.16	50	17.95 (0.08)	18.57 (0.04)	18.56 (0.04)	18.40 (0.06)	17.51 (0.08)	15.45 (0.05)	GC II
		13.07 (0.01)	12.25 (0.01)	10.96 (0.01)	9.56 (0.01)	5.43 (0.10)	— —	
053117.45-710533.72	33	— —	— —	— —	— —	18.66 (0.18)	17.10 (0.12)	CD mult.
		13.56 (0.02)	13.70 (0.03)	10.88 (0.02)	9.08 (0.01)	6.21 (0.23)	-1.05 (0.39)	
053117.50-710354.72	14	— —	— —	— —	— —	18.70 (0.16)	15.69 (0.05)	C I
		12.82 (0.03)	12.03 (0.01)	9.99 (0.02)	8.41 (0.02)	3.20 (0.02)	-2.43 (0.12)	
053117.62-710536.24	28	— —	20.33 (0.11)	20.14 (0.11)	19.42 (0.11)	19.47 (0.28)	18.05 (0.21)	CD II
		13.38 (0.02)	13.70 (0.04)	10.64 (0.02)	8.85 (0.01)	6.17 (0.22)	-1.17 (0.36)	
053119.58-710420.28	71	— —	18.56 (0.07)	17.42 (0.08)	16.51 (0.04)	15.80 (0.03)	14.93 (0.04)	SD

Table 4.1 (continued)

Name (1)	Rank (2)	U (3) [3.6] (9)	B (4) [4.5] (10)	V (5) [5.8] (11)	I (6) [8.0] (12)	J (7) [24] (13)	K (8) [70] (14)	Class. (15)
		13.94 (0.04)	13.74 (0.06)	12.24 (0.07)	10.32 (0.05)	3.03 (0.05)	-2.49 (0.13)	
053120.02-710413.80	29	— —	18.644 (0.11)	17.61 (0.17)	17.59 (0.12)	18.38 (0.14)	17.65 (0.20)	DS
		13.54 (0.09)	13.39 (0.10)	10.77 (0.07)	8.85 (0.05)	2.50 (0.03)	-2.76 (0.11)	
053120.06-710400.84	89	15.70 (0.07)	16.61 (0.03)	16.24 (0.04)	15.61 (0.04)	15.23 (0.03)	14.52 (0.03)	SD
		14.00 (0.09)	13.52 (0.05)	12.78 (0.55)	10.84 (0.28)	2.52 (0.02)	-2.93 (0.10)	
053120.95-710409.12	12	— —	— —	— —	— —	— —	— —	DC I
		12.58 (0.05)	12.52 (0.05)	10.01 (0.05)	8.18 (0.05)	2.00 (0.01)	-2.95 (0.10)	
053121.22-710542.36	52	18.58 (0.12)	18.81 (0.06)	19.23 (0.07)	19.37 (0.13)	17.50 (0.09)	16.25 (0.07)	DS
		12.43 (0.01)	12.61 (0.01)	11.14 (0.07)	9.61 (0.07)	4.72 (0.05)	-1.42 (0.21)	
053121.36-710411.64	17	16.40 (0.15)	17.14 (0.05)	16.70 (0.11)	16.49 (0.11)	17.39 (0.08)	16.50 (0.09)	SD
		13.09 (0.10)	12.76 (0.08)	10.36 (0.08)	8.52 (0.07)	1.87 (0.01)	-2.99 (0.10)	
053121.46-710407.32	13	13.89 (0.04)	14.66 (0.03)	14.70 (0.02)	14.44 (0.05)	14.72 (0.02)	14.53 (0.03)	DSC III
		12.72 (0.06)	12.62 (0.07)	10.02 (0.05)	8.19 (0.04)	1.84 (0.01)	-3.03 (0.09)	
053121.48-710359.04	32	— —	— —	— —	— —	19.09 (0.26)	16.69 (0.09)	DC I
		13.45 (0.07)	13.50 (0.08)	10.77 (0.06)	9.06 (0.06)	2.48 (0.01)	-3.01 (0.09)	
053121.84-710540.20	47	— —	18.05 (0.04)	16.29 (0.02)	14.42 (0.03)	13.13 (0.01)	12.02 (0.01)	SD
		11.79 (0.01)	11.92 (0.01)	10.92 (0.06)	9.55 (0.07)	4.54 (0.04)	-1.51 (0.20)	
053121.96-710424.96	26	— —	— —	— —	— —	— —	17.95 (0.20)	D
		13.70 (0.14)	13.71 (0.14)	10.58 (0.03)	8.78 (0.03)	2.86 (0.02)	-2.61 (0.12)	
053122.54-710535.52	55	— —	— —	— —	— —	— —	— —	DC I
		13.82 (0.10)	13.99 (0.09)	11.47 (0.13)	9.63 (0.10)	4.29 (0.03)	-1.61 (0.19)	
053122.78-710409.84	1	15.65 (0.12)	16.60 (0.06)	16.18 (0.12)	15.30 (0.14)	14.78 (0.02)	13.28 (0.02)	GC II
		11.41 (0.02)	11.05 (0.02)	9.26 (0.03)	7.52 (0.03)	1.55 (0.01)	-3.10 (0.09)	
053122.80-710414.88	21	14.43 (0.07)	15.46 (0.04)	15.20 (0.11)	15.04 (0.10)	14.60 (0.02)	13.29 (0.02)	DSC mult.
		12.36 (0.05)	12.29 (0.05)	10.61 (0.11)	8.61 (0.07)	1.68 (0.01)	-3.03 (0.09)	
053123.23-710425.32	37	— —	— —	— —	— —	— —	18.30 (0.34)	D
		13.58 (0.13)	13.45 (0.09)	11.08 (0.15)	9.27 (0.11)	2.84 (0.01)	-2.68 (0.11)	
053123.38-710416.32	16	— —	— —	— —	— —	— —	16.98 (0.17)	D
		12.52 (0.04)	12.35 (0.03)	10.30 (0.06)	8.47 (0.05)	1.85 (0.01)	-2.98 (0.09)	

Table 4.1 (continued)

Name (1)	Rank (2)	U (3)	B (4)	V (5)	I (6)	J (7)	K (8)	Class. (15)
		[3.6] (9)	[4.5] (10)	[5.8] (11)	[8.0] (12)	[24] (13)	[70] (14)	
053123.42-710412.36	2	16.28 (0.12)	17.34 (0.07)	16.96 (0.15)	— —	14.86 (0.02)	14.56 (0.04)	G
		11.72 (0.03)	11.44 (0.03)	9.42 (0.04)	7.67 (0.04)	1.64 (0.01)	-3.05 (0.09)	
053123.42-710511.76	88	19.53 (0.15)	18.21 (0.04)	16.82 (0.04)	15.51 (0.03)	14.34 (0.02)	13.38 (0.02)	SD
		13.22 (0.02)	13.41 (0.02)	12.25 (0.06)	10.83 (0.06)	5.29 (0.10)	-0.84 (0.30)	
053123.50-710419.20	23	15.84 (0.15)	16.82 (0.07)	16.59 (0.14)	16.58 (0.17)	16.88 (0.07)	16.52 (0.10)	SD
		13.19 (0.06)	13.14 (0.06)	10.54 (0.05)	8.68 (0.03)	2.17 (0.01)	-2.90 (0.10)	
053123.57-710735.40	10	— —	— —	— —	— —	18.36 (0.16)	15.35 (0.05)	C mult.
		12.34 (0.01)	11.67 (0.01)	9.81 (0.02)	8.10 (0.01)	5.21 (0.01)	-1.38 (0.20)	
053123.78-710423.52	31	— —	18.58 (0.15)	18.11 (0.23)	18.11 (0.19)	17.70 (0.09)	16.21 (0.07)	DG
		13.48 (0.09)	13.25 (0.09)	10.77 (0.08)	8.96 (0.07)	2.70 (0.01)	-2.76 (0.11)	
053124.05-710524.72	44	17.83 (0.13)	18.49 (0.04)	17.55 (0.04)	16.42 (0.04)	15.78 (0.03)	14.98 (0.04)	SD
		13.69 (0.08)	13.58 (0.05)	11.17 (0.07)	9.45 (0.07)	4.48 (0.05)	-1.52 (0.20)	
053124.22-710408.76	15	— —	— —	— —	— —	18.17 (0.14)	17.39 (0.16)	DS
		12.93 (0.04)	12.69 (0.05)	10.35 (0.04)	8.45 (0.03)	1.96 (0.01)	-2.93 (0.10)	
053124.31-710735.76	11	— —	20.27 (0.07)	19.97 (0.08)	19.60 (0.15)	18.97 (0.23)	16.35 (0.08)	C mult.
		12.42 (0.02)	11.68 (0.01)	9.85 (0.02)	8.12 (0.02)	7.50 (0.01)	-1.37 (0.21)	
053124.84-710406.24	45	— —	— —	— —	— —	18.92 (0.26)	— —	D
		13.72 (0.05)	13.46 (0.05)	11.31 (0.05)	9.47 (0.04)	2.55 (0.02)	-2.76 (0.11)	
053124.94-710738.28	39	16.10 (0.05)	16.80 (0.03)	16.71 (0.03)	16.51 (0.03)	16.39 (0.05)	16.37 (0.08)	SD
		13.73 (0.05)	13.11 (0.03)	11.16 (0.06)	9.34 (0.04)	7.18 (0.01)	-1.29 (0.21)	
053124.96-710525.44	61	17.78 (0.10)	17.57 (0.03)	16.48 (0.02)	15.45 (0.03)	14.54 (0.02)	13.85 (0.02)	SD
		13.25 (0.04)	13.30 (0.03)	11.63 (0.12)	9.86 (0.10)	4.63 (0.07)	-1.46 (0.20)	
053125.44-710417.76	66	— —	17.92 (0.07)	16.60 (0.08)	14.83 (0.04)	13.58 (0.01)	12.48 (0.01)	SD
		12.27 (0.03)	12.27 (0.03)	11.32 (0.17)	10.00 (0.22)	2.91 (0.02)	-2.66 (0.11)	
053125.54-710421.36	30	— —	— —	— —	— —	17.83 (0.11)	16.46 (0.09)	D
		12.57 (0.02)	12.57 (0.02)	10.55 (0.05)	8.91 (0.04)	3.16 (0.02)	-2.58 (0.12)	
053126.06-710727.48	87	19.97 (0.16)	18.66 (0.03)	17.38 (0.02)	16.03 (0.05)	15.00 (0.02)	14.12 (0.02)	SD
		13.59 (0.03)	13.72 (0.03)	12.38 (0.09)	10.82 (0.10)	4.88 (0.01)	-0.99 (0.25)	
053126.16-710514.64	80	17.35 (0.10)	17.36 (0.03)	16.15 (0.03)	15.13 (0.03)	14.25 (0.02)	13.57 (0.02)	SD

Table 4.1 (continued)

Name	Rank	U	B	V	I	J	K	Class.
(1)	(2)	(3)	(4)	(5)	(6)	(7)	(8)	(15)
		[3.6]	[4.5]	[5.8]	[8.0]	[24]	[70]	
		(9)	(10)	(11)	(12)	(13)	(14)	
		13.29 (0.01)	13.47 (0.03)	12.09 (0.05)	10.62 (0.06)	5.81 (0.26)	-0.62 (0.35)	
053126.52-710421.00	43	— —	18.49 (0.15)	18.90 (0.24)	19.01 (0.20)	— —	— —	DS
		13.85 (0.06)	13.82 (0.06)	11.18 (0.06)	9.43 (0.04)	3.61 (0.03)	-2.42 (0.13)	
053126.52-710726.04	79	20.37 (0.21)	19.35 (0.05)	18.21 (0.03)	16.96 (0.03)	16.63 (0.05)	15.88 (0.06)	SD
		13.49 (0.02)	13.66 (0.03)	12.17 (0.07)	10.60 (0.07)	5.35 (0.01)	-0.84 (0.27)	
053126.69-710327.36	92	18.79 (0.16)	18.56 (0.04)	17.27 (0.09)	15.92 (0.03)	14.80 (0.02)	13.86 (0.02)	SD
		13.60 (0.02)	13.69 (0.03)	12.48 (0.07)	10.93 (0.07)	5.42 (0.04)	-1.15 (0.23)	
053127.53-710739.00	68	— —	— —	— —	— —	16.96 (0.06)	15.89 (0.06)	CD I/II
		14.12 (0.03)	13.77 (0.03)	11.69 (0.04)	10.06 (0.03)	5.57 (0.02)	-0.72 (0.29)	
053130.36-710404.80	42	17.19 (0.16)	18.86 (0.08)	18.29 (0.15)	18.27 (0.08)	17.94 (0.10)	16.09 (0.06)	GC II
		13.56 (0.02)	13.27 (0.02)	11.07 (0.02)	9.43 (0.02)	5.03 (0.05)	-1.70 (0.18)	
053130.62-705749.32	93	— —	21.06 (0.13)	20.11 (0.08)	18.43 (0.08)	— —	— —	G
		13.95 (0.01)	13.48 (0.01)	12.99 (0.02)	10.99 (0.01)	7.56 (0.01)	— —	
053134.13-710540.92	101	— —	21.33 (0.17)	20.62 (0.16)	19.66 (0.10)	18.78 (0.16)	17.24 (0.12)	SD
		16.43 (0.19)	13.64 (0.28)	13.29 (0.12)	11.44 (0.09)	6.57 (0.05)	-0.38 (0.35)	
053157.65-710049.68	75	18.74 (0.23)	19.81 (0.13)	18.86 (0.12)	17.68 (0.11)	— —	— —	G
		13.86 (0.01)	13.82 (0.02)	12.99 (0.03)	10.43 (0.01)	7.92 (0.06)	— —	

Note. — Column (1): candidate name, Column (2): ranking of the brightness at 8 μm (from high to low), Columns (3)-(14): photometric magnitudes (and errors) of 12 wavelengths from U to 70 μm, Column (15): classification & remarks.

4.2 Determining Final YSO Candidates

After using color-magnitude criteria to quickly eliminate most probable non-YSOs from my list of candidates, I still had some "contaminants" among my remaining list. With only 112 sources left, I examined each candidate individually to further determine its nature. I assessed each initial YSO candidate based on its spectral energy distribution (SED), location in color-magnitude space, brightness, and morphology. During this assessment, I was able to identify several non-YSOs, including background galaxies, dust clumps, and stars.

An SED is a plot of the fluxes of an object at different wavelengths. I constructed SEDs for all of the initial YSO candidates from the fluxes that I measured in the different available optical and infrared wavelengths. Figure 4.5 is an example of an SED for one of my candidate YSOs that had a flux at each of the 12 measured wavelengths. All of the initial YSO candidate SEDs are given in Appendix A. The SEDs are plotted in log space with the flux values given in Janskys (10^{-26} W m^{-2} Hz). I examined the shapes of these SEDs as part of my assessment of the initial YSO candidates.

To look at each candidate's source brightness and morphology, I prepared and examined images for each candidate in the following wavelengths: Hα, J, Ks, [3.6 μm], [4.5 μm], [5.8 μm], [8.0 μm], [24 μm], and [70 μm]. I displayed all of these images for each candidate using SAOImage DS9 [49]. A screenshot showing an example of the graphical interface for one candidate is given in Figure 4.6. Typically, I looked at a $1'$ x $1'$ region surrounding each source. An occasional exception was with the ISPI J and K_s images. These have higher resolution and make it easier to discern the morphologies of some sources; I therefore would sometimes display a smaller field of view ($10''$ x $10''$, $15''$ x $15''$ or $30''$ x $30''$) for these images. Additionally, while I did not assess the nature of a source based on its surrounding interstellar environment, I prepared a $20'$ x $20'$ field of view image of N206 in Hα with CO giant molecular cloud (GMC) contours superposed on it so that I could note each source's

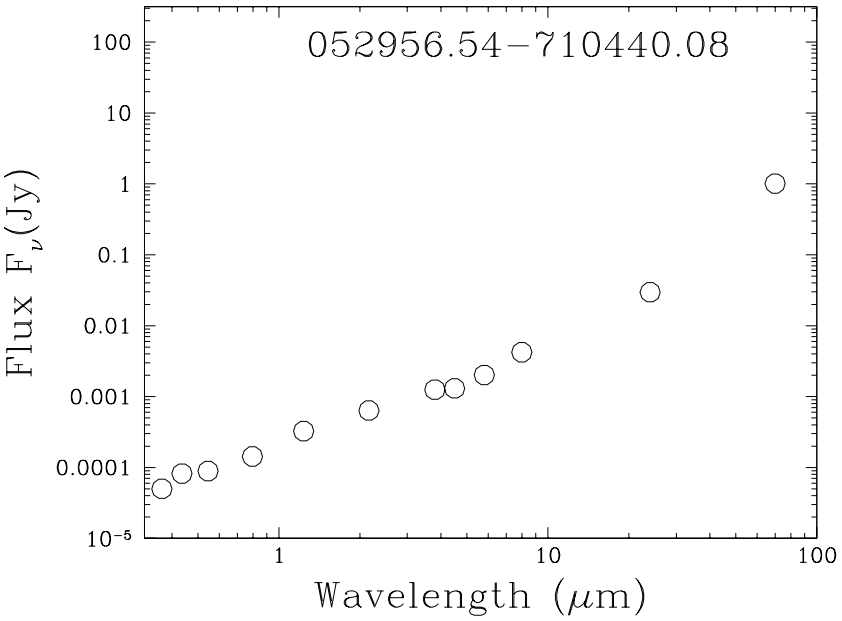

Figure 4.5 Spectral energy distribution (SED) for YSO candidate 052956.54-710440.08, given in log space.

location with respect to Hα filaments, dark clouds, or GMCs. In the following sections I describe how I used the photometry and images of my initial candidates to identify non-YSOs that were still among them.

4.2.1 Identifying Additional AGB Stars

There were likely to still be some AGB stars in my initial YSO candidate list that were surrounded by large amounts of dust. To begin to search for possible AGB stars remaining, I performed photometry in the available wavelength images for the 28 known AGB stars in N206. I give this photometry in Table B in Appendix B. I constructed SEDs for these AGB stars to examine their shapes. The 28 SEDs are given in Figures 4.7 and 4.8. All of these SEDs have a peak between 1 and 4 μm. These AGB stars would be similar to AGB stars in our Galaxy, with dust temperatures between about 400 and 1000 K [50]. The AGB stars mixed in with the initial YSO candidates would be more obscured by dust and would have

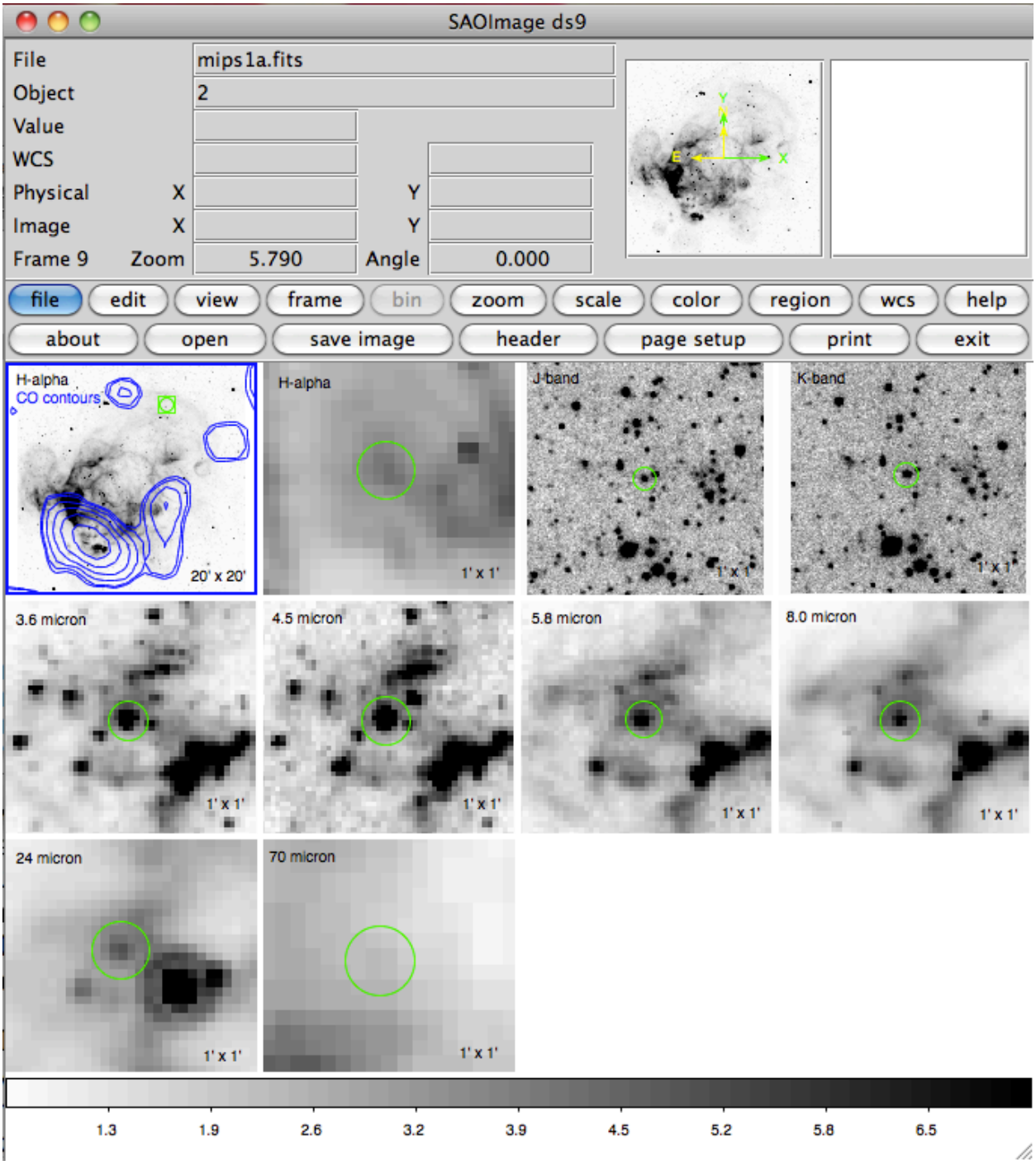

Figure 4.6 An example of the multiwavelength images viewed for each candidate during its assessment. The wavelength being displayed is at the upper left of each box, and the field of view is at the lower right. The green circles show the source being examined and are not indicative of the flux aperture used in photometry.

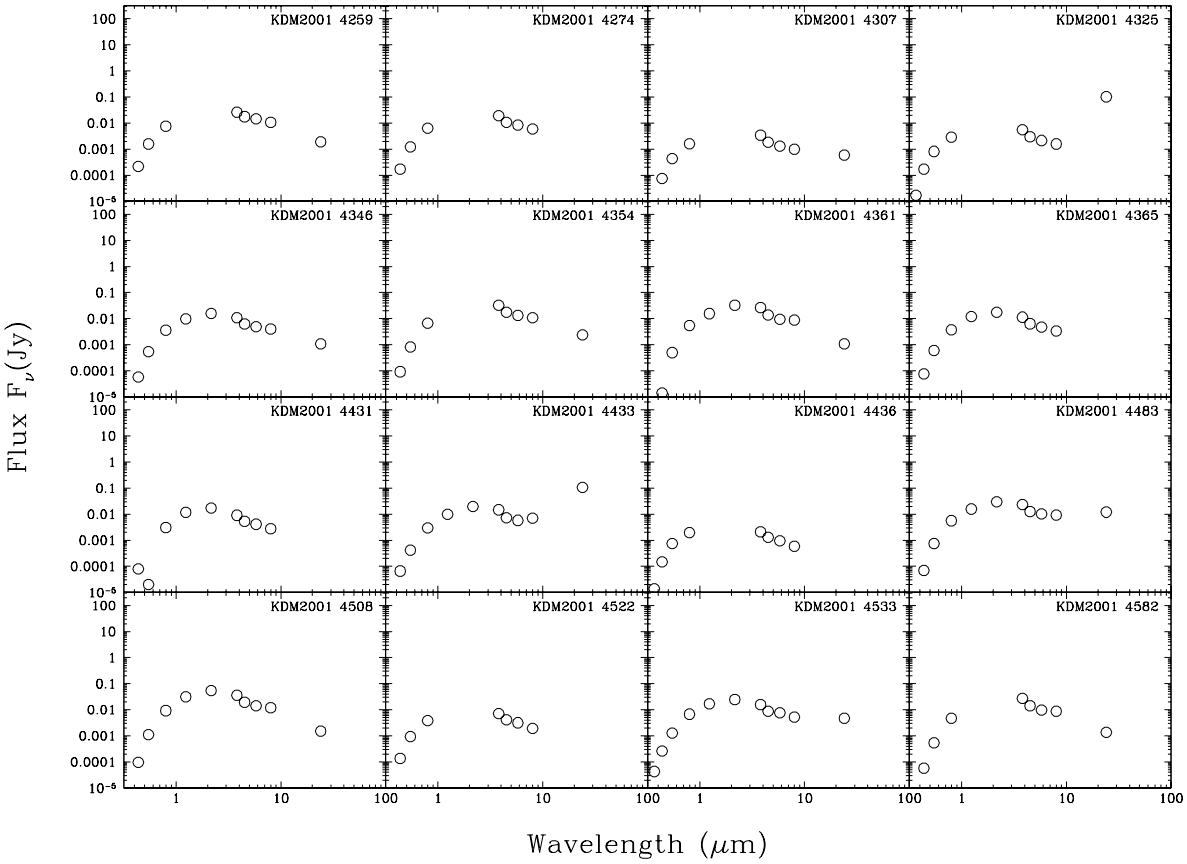

Figure 4.7 Spectral energy distributions (SEDs) for known AGB stars in N206, plotted in log space.

lower dust temperatures and redder colors. Their SEDs would look similar in shape to the SEDs of the known AGB stars, but they would peak at longer wavelengths.

None of the the 112 YSO candidate SEDs looked similar in shape to those of the known AGB stars. I could not therefore confidently determine any of the candidates to be AGB stars. This is not surprising, since, through a similar assessment, Chen et al. (2009) [2] found only two AGB stars in their initial YSO candidate list of 99. Their YSO search was in a region of similar size to N206.

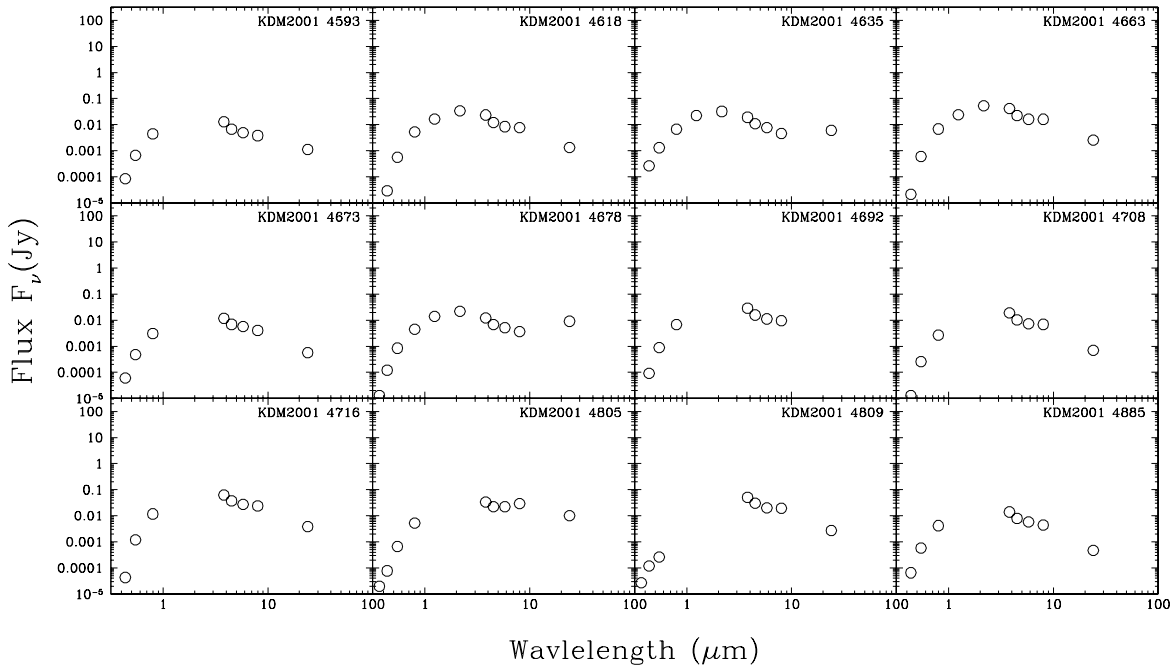

Figure 4.8 A continuation of the previous figure. SEDs for known AGB stars in N206, plotted in log space.

4.2.2 Identifying Additional Background Galaxies

A type of contaminant that I did find among my YSO candidates was background galaxies. Again, I first looked at the SEDs to try to determine which candidates might be galaxies. Galaxies mixed in with the YSO candidates in that color-magnitude space would be galaxies that are abundant in gas and dust, such as late-type galaxies or AGN. The SEDs of late-type galaxies have two broad humps, one due to stellar emission over optical and near-infrared, and the other from dust emission over mid- and far-infrared. The SED of an AGN depends on the viewing angle. It can be flat from optical to far-infrared, or obscured in optical,

showing only mid- and far-infrared. In this case, it could be either falling or rising at 24 μm [2].

I used SIMBAD to search for known galaxies in the N206 field of view, so that I could perform photometry on them and construct SEDs for comparison with my YSO candidates. I found four galaxies in the region. In order to have a larger sample to compare against, I extended the search to a radius of 28″ and found an additional twelve galaxies. I performed photometry on these in the available wavelength images and constructed their SEDs. The photometry for these sixteen known galaxies is given in Table B.2 in Appendix B, and their SEDs are given in Figure 4.9. Unfortunately, most of these galaxies were outside of the *J*- and *Ks*-band images in my dataset, so those points are missing from the SEDS. The result is that the shape of two broad humps can only be seen clearly in the SED of galaxy 2MASSI J0530201-710748. The SED of another galaxy, 2MASSI J0531228-710413, looks almost flat from optical through near-infrared, then begins to rise in a dust hump in the mid-infrared.

I determined six of my YSO candidates (052923.76-710214.64, 052938.47-705520.64, 053020.88-705408.28, 053123.42-710412.36, 053130.62-705749.32, and 053157.65-710049.68) to have SEDs that resembled those of galaxies, showing two broad humps due to stellar and dust emission. If they can be resolved in images, background galaxies can also be distinguished through their morphologies. I used the higher-resolution *J*- and *Ks*-band images to look at the morphologies of four of these six galaxy candidates (the other two candidates were not in the *J*- and *Ks*-band images). These four galaxy candidates looked extended in the near-infrared images, and the other two looked extended at the shorter-wavelength IRAC bands. Additionally, the latter three of these galaxy candidates corresponded with three of the known galaxies in the N206 field of view (053123.42-710412.36 with 2MASSI J0531228-710413, 053130.62-705749.32 with 2MASS J05315772-7100494, and 053157.65-710049.68 with 2MASS J05313060-7057491). I therefore classified these six YSO candidates as galaxies, giving them the classification "G" in Table 4.1.3, based on the shapes of their SEDs, their

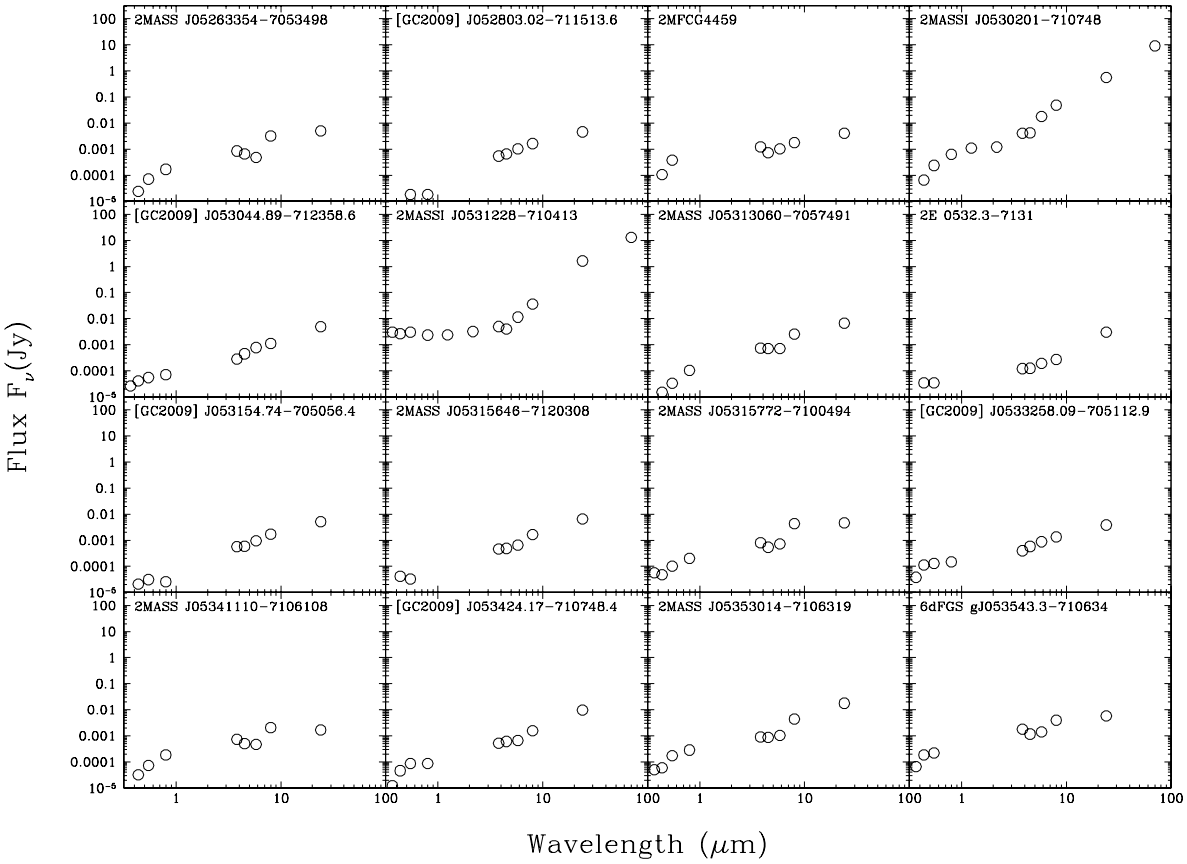

Figure 4.9 Spectral energy distributions for known galaxies within a 28″ radius of N206, plotted in log space.

morphologies in the near- and mid-infrared bands, and their correspondence to previously known galaxies. The SEDs for these galaxies, along with images of them that I examined, are in Figures 4.10 and 4.11. In this figure, a near- or mid-infrared image for each galaxy is shown, exemplifying its extended morphology. Also, a [24 μm] image is given for each galaxy, showing its relative brightness at this wavelength.

4.2.3 Identifying Dust Clumps

Some warm dust clumps that showed peaks of emission were included by my selection criteria in N206. I found that these were usually at the bend of a dust filament. The SEDS of emission from areas of diffuse dust can look similar to SEDs of circumstellar dust disks around YSOs. I therefore had to rely mostly on the images of the candidates to identify dust clumps. If a source looked diffuse across different wavelengths, I determined that it was not a YSO, a star, or a galaxy. The near-infrared images were particularly useful for this. In the *Ks* images, YSOs or stars would appear unresolved, while dust clumps may appear as extended emission. In this manner, I classified 12 of my YSO candidates (052919.30-710134.68, 053019.27-710750.88, 053019.49-710739.72, 053047.06-710855.68, 053055.32-710605.04, 053056.33-710731.08, 053056.59-710754.48, 053121.96-710424.96, 053123.23-710425.32, 053123.38-710416.32, 053124.84-710406.24, and 053125.54-710421.36) to be dust clumps, giving them a designation of "D". SEDs and images for these dust clumps are given in Figures 4.12 through 4.14. For these figures, images at [4.5 μm] and [5.8 μm] are given, showing the diffuse nature of the source.

I determined one YSO candidate, 053123.78-710423.52, to be a combination of a dust clump and a background galaxy. I designated this source as "DG" to emphasize that its SED was mostly due to dust, but that the optical and near-infrared flux values in the SED were likely from a nearby galaxy. This galaxy is visible in the *Ks*-band image in Figure 4.15, to the upper-right of the central source. The flux aperture used in the photometry would have easily picked up emission from this nearby galaxy. Also in Figure 4.15 are the SED for this source and a [5.8 μm] image, showing the diffuse nature of the source.

Similarly, four YSO candidates (053120.02-710413.80, 053121.22-710542.36, 053124.22-710408.76, and 053126.52-710421.00) were classified as "DS", meaning that its SED is mostly due to dust, but that there is some contribution from a stellar source as well. These SEDs and images are given in Figure 4.16. The middle image for each candidate was selected to

show the stellar source in question, and the longer wavelength image to the right was selected to show the diffuse dust emission.

4.2.4 Identifying Stellar Sources

Stars near dust clumps that were among my candidates would have SEDs that are largely due to stellar emission, but the infrared excess would come from the nearby emitting dust. I found 34 of these among my list, and designated them as "SD". This designation is different from "DS" in that the shape of the SED is mostly due to the stellar source. For all of these objects, a stellar source was seen in shorter wavelengths, was seen to fade toward longer wavelengths, and then just dust would be seen at the longest wavelengths. The *J*- and *Ks*-band fluxes were also used to classify these; stars are brighter at *J*, while YSOs are brighter at *Ks*. SEDs and images for these 29 objects are given in Figures 4.17- 4.23. The images for these objects were selected to show a stellar source at shorter wavelengths and to show the source fading and the dust dominating at longer wavelengths.

The last "contaminant" among the list of YSO candidates was classified as "SG", because it appeared to be a star projected next to a galaxy. The star was visible in the images through [5.8 μm], but then the nearby galaxy seemed to mostly dominate the SED after that point. The nearby galaxy is candidate 052938.47-705520.64, previously reclassified as a galaxy. The SED and images for this source, 052938.90-705523.52, is given in Figure 4.24.

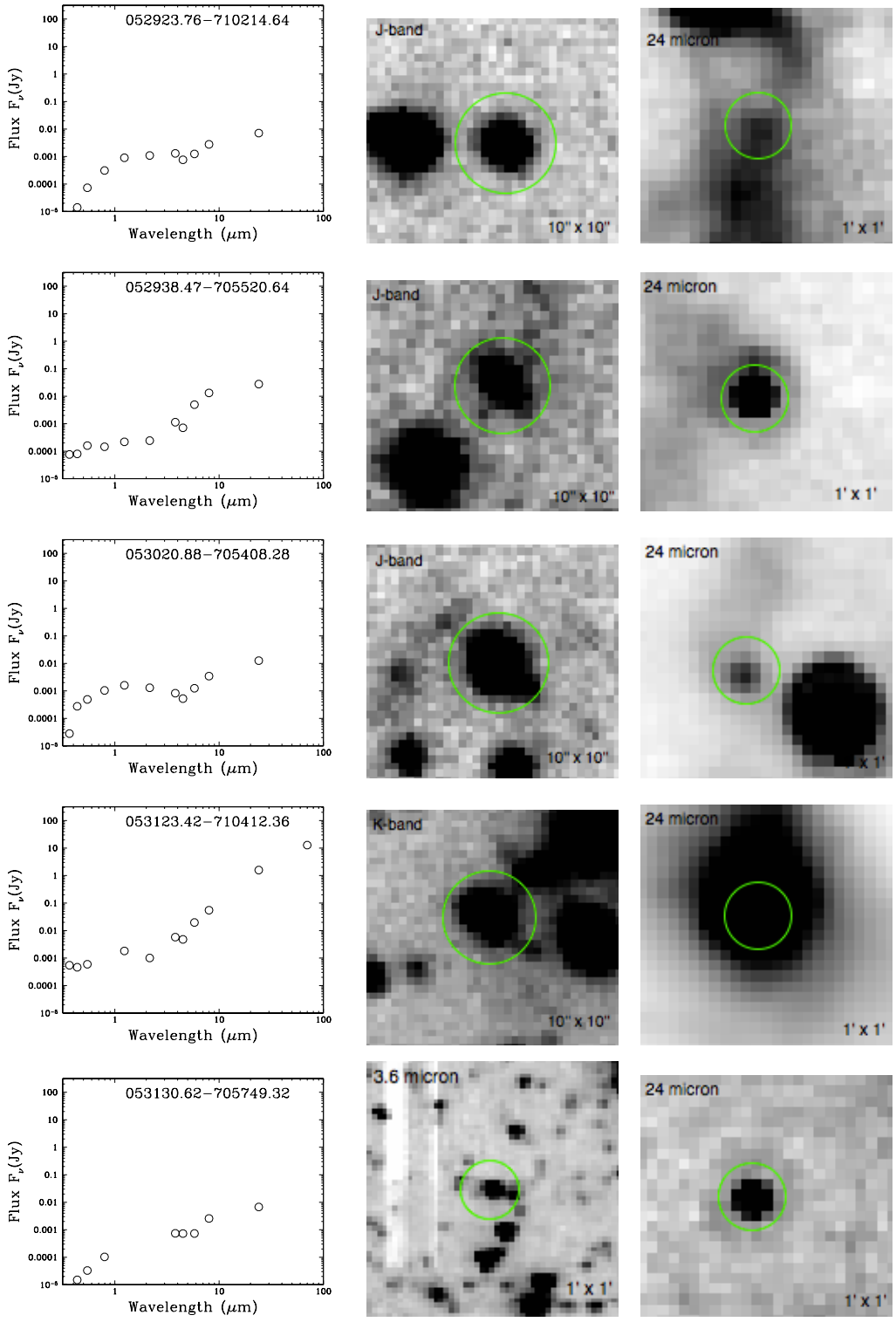

Figure 4.10 SEDS and sample multiwavelength images for each YSO candidate classified as a galaxy. The wavelength being displayed is at the upper left of each box, and the field of view is at the lower right. The green circles show the source being examined and are not indicative of the flux aperture used in photometry.

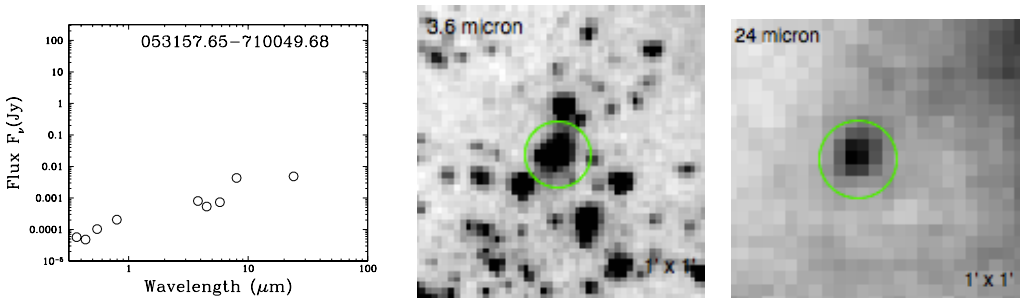

Figure 4.11 A continuation of the previous figure. SEDs and sample multiwavelength images for each YSO candidate classified as a galaxy. The wavelength being displayed is at the upper left of each box, and the field of view is at the lower right. The green circles show the source being examined and are not indicative of the flux aperture used in photometry.

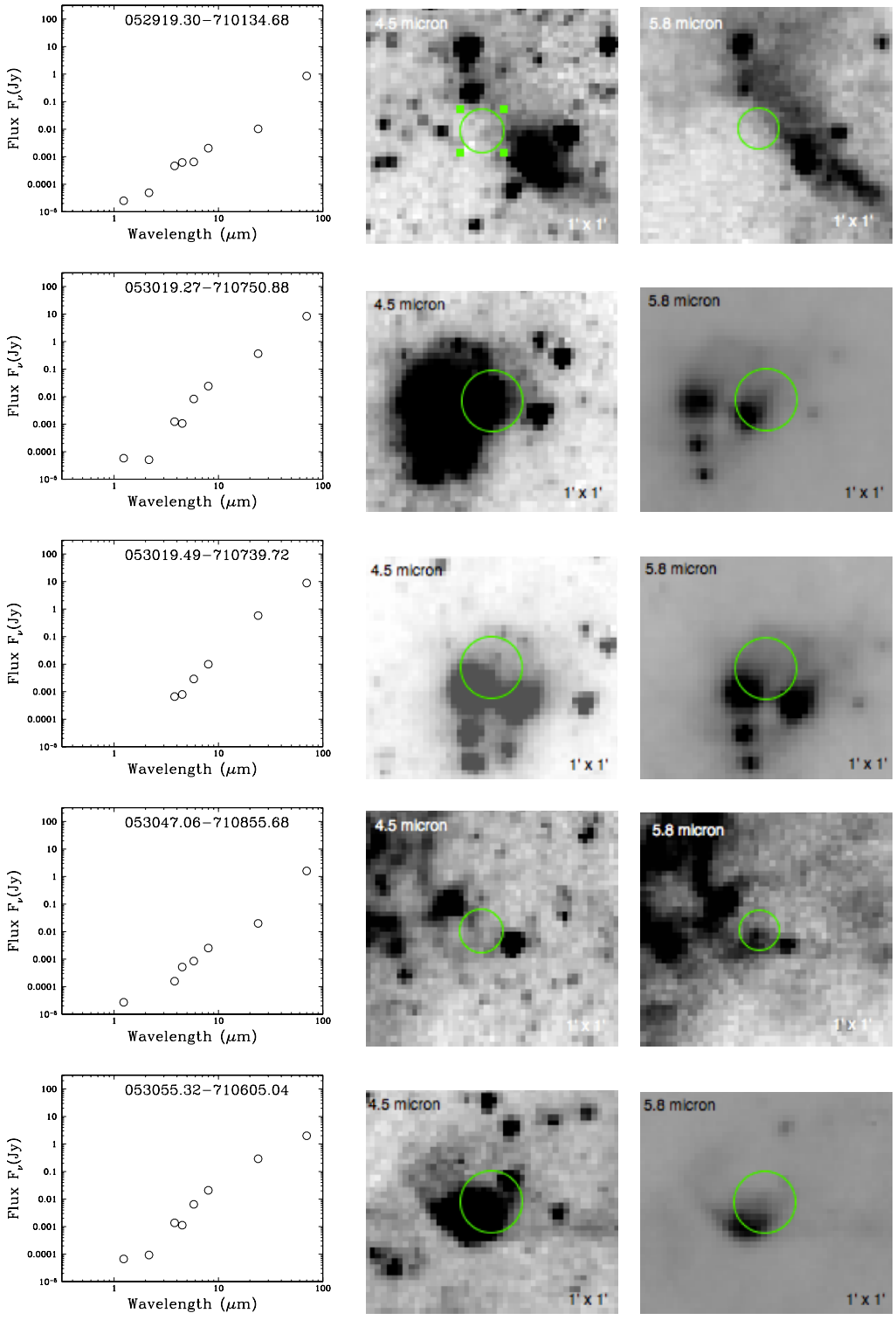

Figure 4.12 SEDS and sample multiwavelength images for each YSO candidate classified as a dust clump. The wavelength being displayed is at the upper left of each box, and the field of view is at the lower right. The green circles show the source being examined and are not indicative of the flux aperture used in photometry.

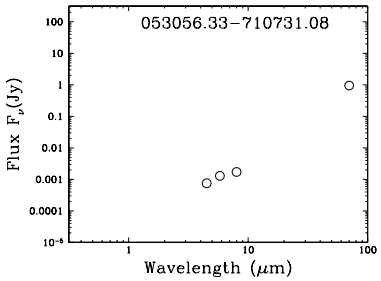
053056.33−710731.08
Flux F_ν(Jy)
Wavelength (μm)

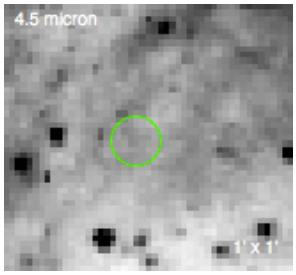
4.5 micron
1' x 1'

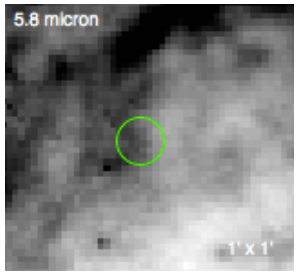
5.8 micron
1' x 1'

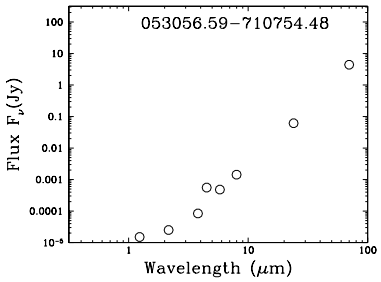
053056.59−710754.48
Flux F_ν(Jy)
Wavelength (μm)

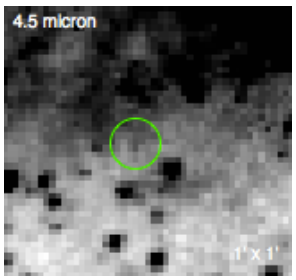
4.5 micron
1' x 1'

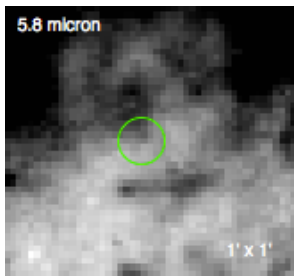
5.8 micron
1' x 1'

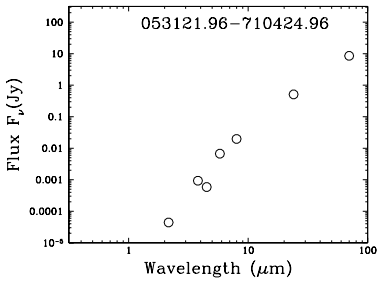
053121.96−710424.96
Flux F_ν(Jy)
Wavelength (μm)

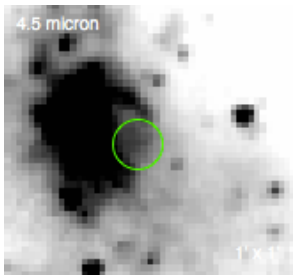
4.5 micron
1' x 1'

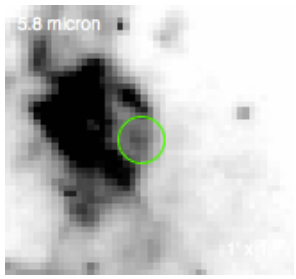
5.8 micron
1' x 1'

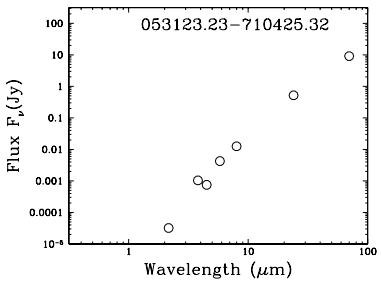
053123.23−710425.32
Flux F_ν(Jy)
Wavelength (μm)

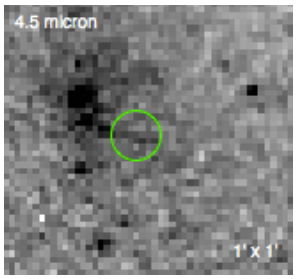
4.5 micron
1' x 1'

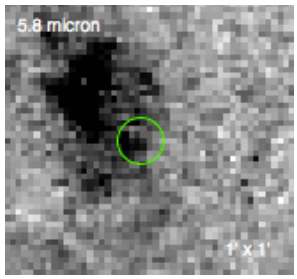
5.8 micron
1' x 1'

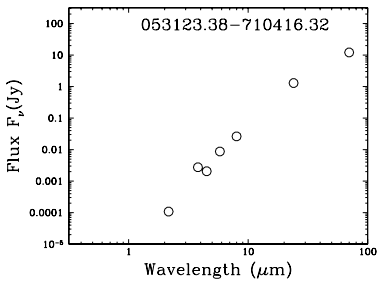
053123.38−710416.32
Flux F_ν(Jy)
Wavelength (μm)

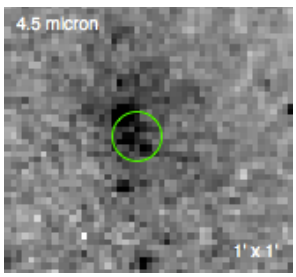
4.5 micron
1' x 1'

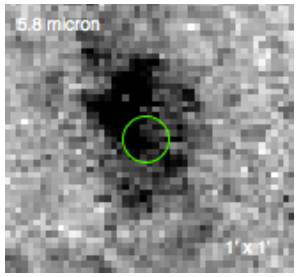
5.8 micron
1' x 1'

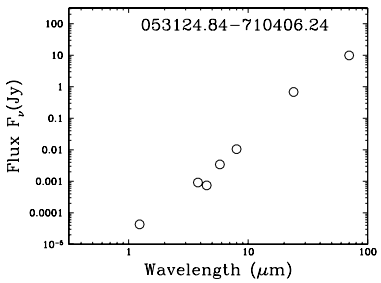
053124.84−710406.24
Flux F_ν(Jy)
Wavelength (μm)

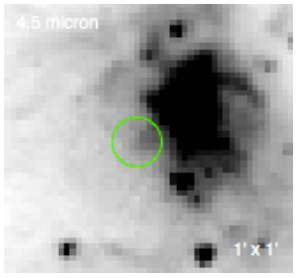
4.5 micron
1' x 1'

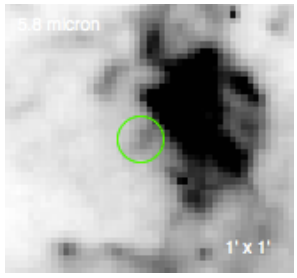
5.8 micron
1' x 1'

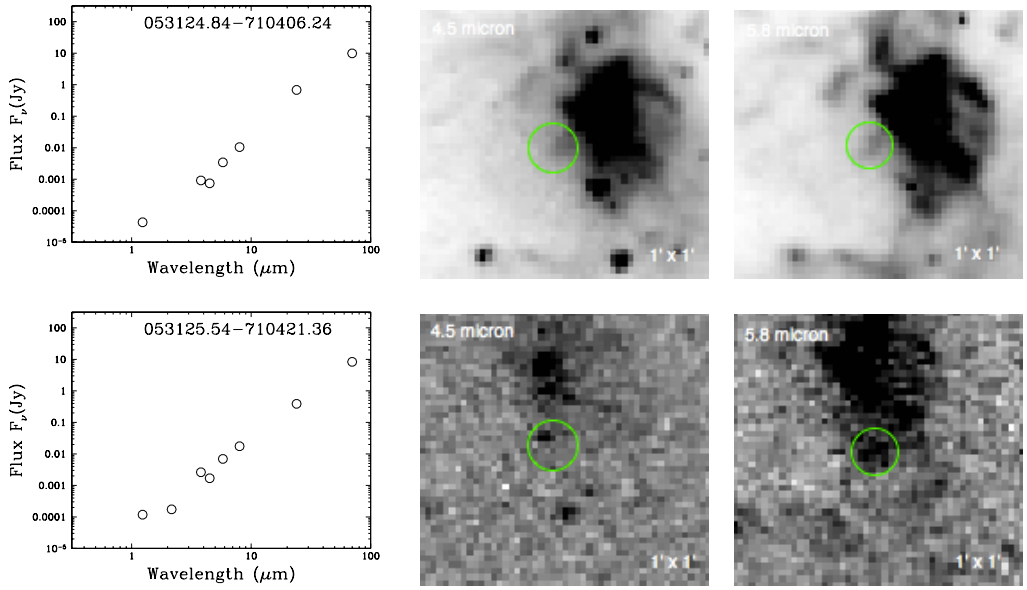

Figure 4.14 A continuation of the previous figure. SEDS and sample multiwavelength images for each YSO candidate classified as a dust clump. The wavelength being displayed is at the upper left of each box, and the field of view is at the lower right. The green circles show the source being examined and are not indicative of the flux aperture used in photometry.

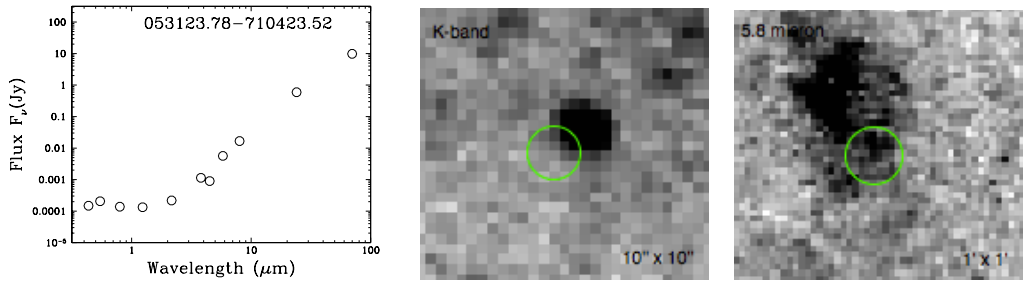

Figure 4.15 SED and sample multiwavelength images for the YSO candidate classified as "DG", due to a combination of dust emission and emission from a nearby background galaxy. The wavelength being displayed is at the upper left of each box, and the field of view is at the lower right. The green circles show the source being examined and are not indicative of the flux aperture used in photometry.

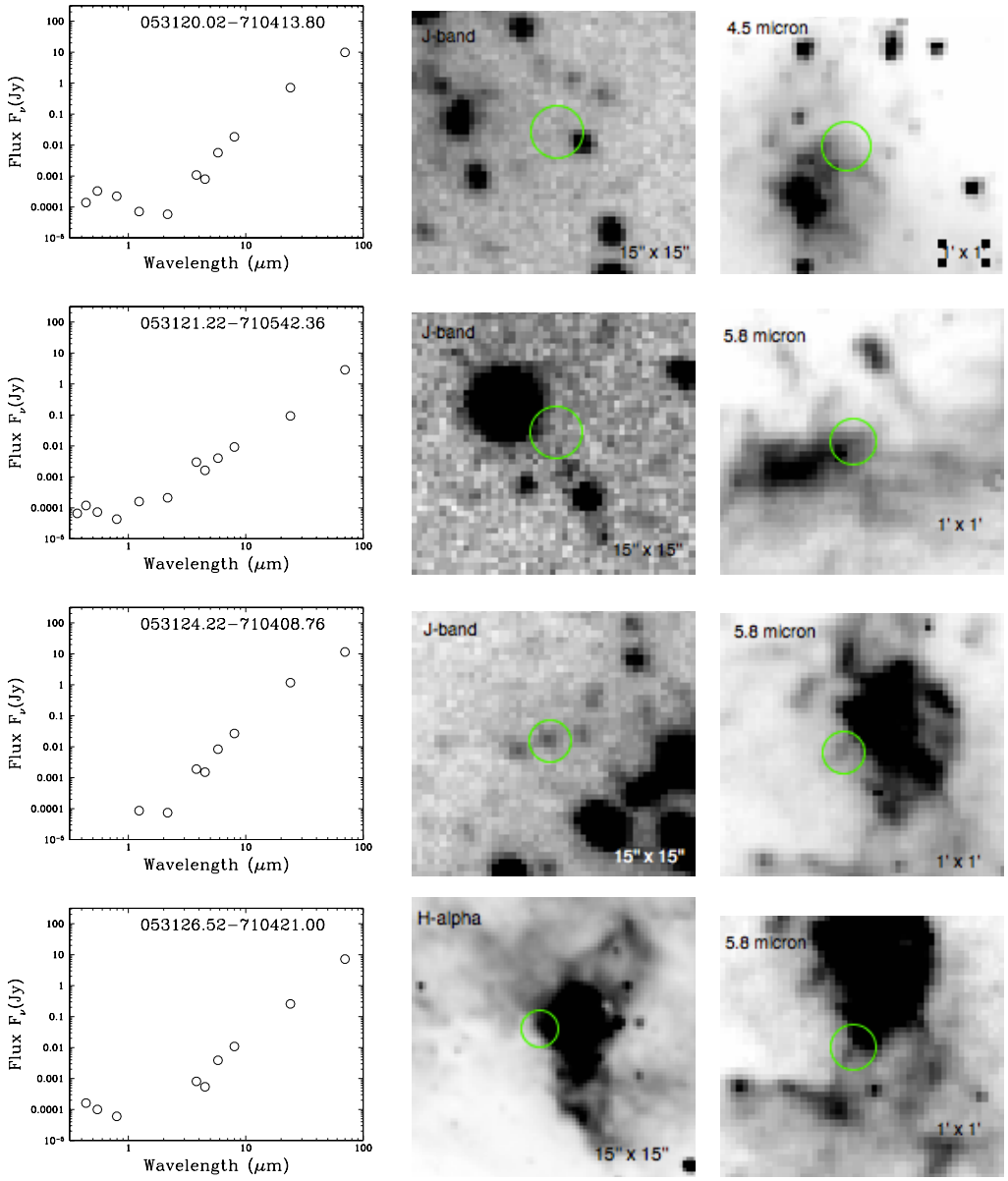

Figure 4.16 SEDs and sample multiwavelength images for the YSO candidates classified as "DS", due to a combination of dust emission and emission from a stellar source. The wavelength being displayed is at the upper left of each box, and the field of view is at the lower right. The green circles show the source being examined and are not indicative of the flux aperture used in photometry.

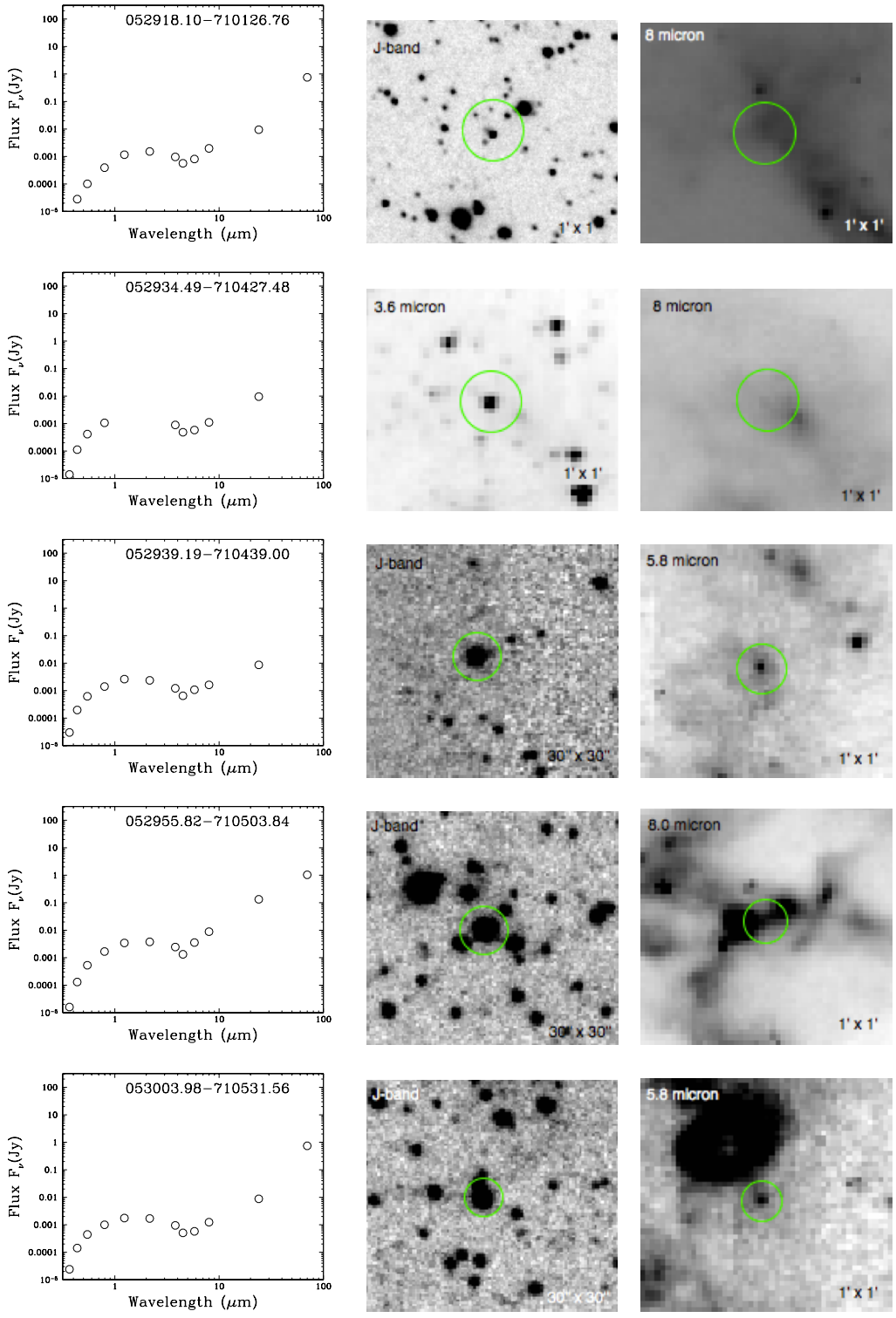

Figure 4.17 SEDs and sample multiwavelength images for the YSO candidates classified as "SD", due to a combination of emission from a stellar source and dust emission, with stellar emission dominating. The wavelength being displayed is at the upper left of each box, and the field of view is at the lower right. The green circles show the source being examined and are not indicative of the flux aperture used in photometry.

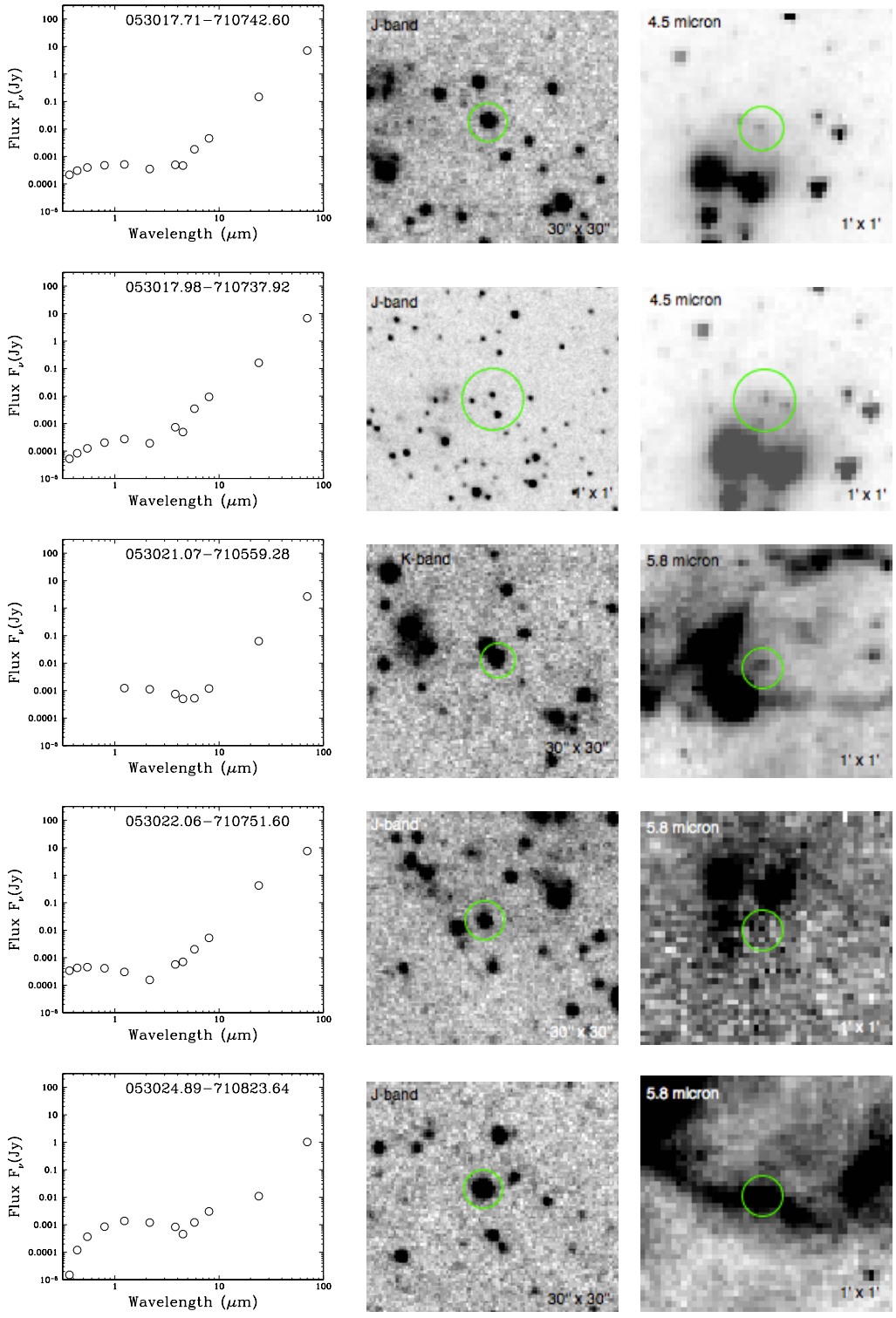

Figure 4.18 A continuation of the previous figure. SEDs and sample multiwavelength images for the YSO candidates classified as "SD", due to a combination of emission from a stellar source and dust emission, with stellar emission dominating. The wavelength being displayed is at the upper left of each box, and the field of view is at the lower right. The green circles show the source being examined and are not indicative of the flux aperture used in photometry.

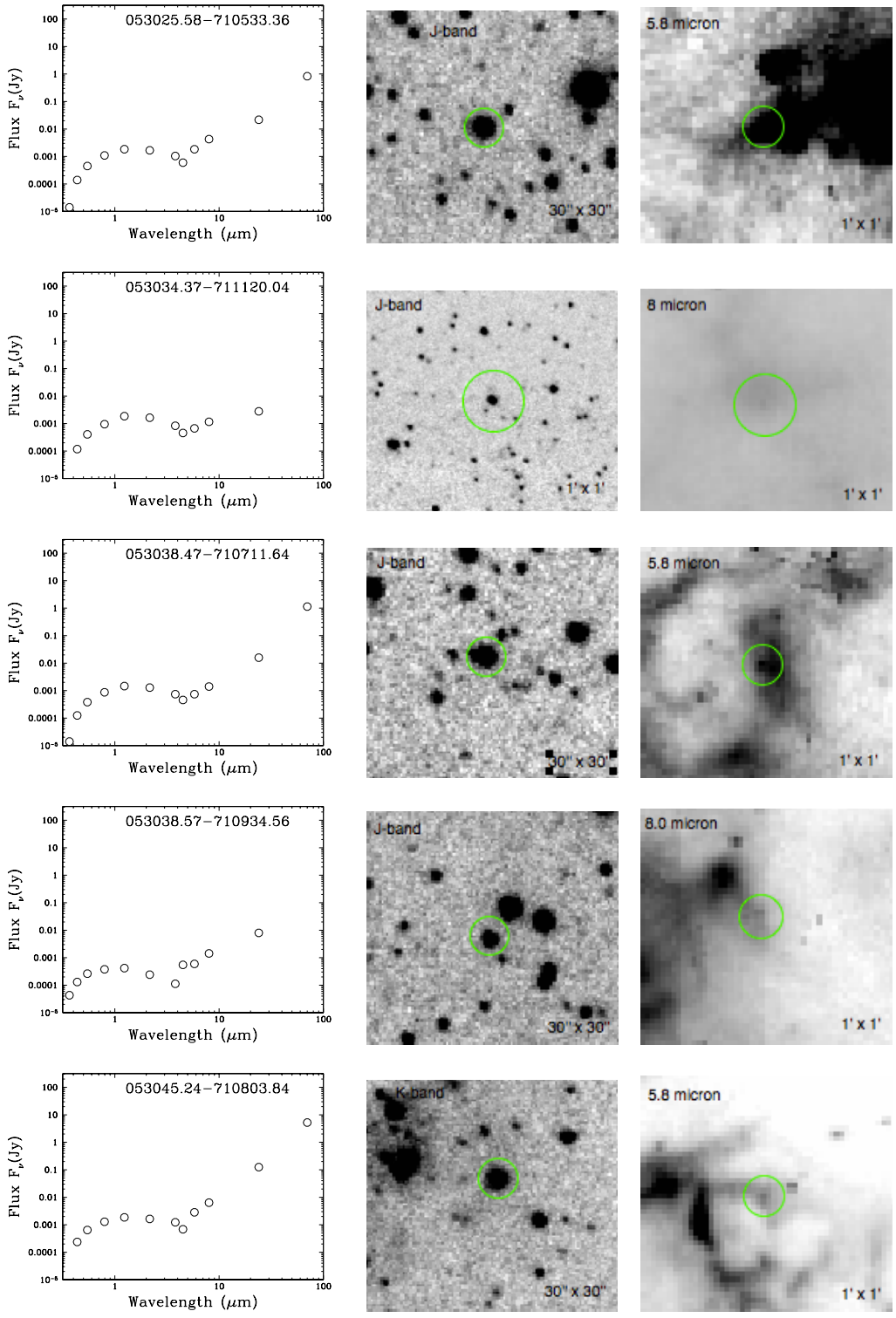

Figure 4.19 A continuation of the previous figure. SEDs and sample multiwavelength images for the YSO candidates classified as "SD", due to a combination of emission from a stellar source and dust emission, with stellar emission dominating. The wavelength being displayed is at the upper left of each box, and the field of view is at the lower right. The green circles show the source being examined and are not indicative of the flux aperture used in photometry.

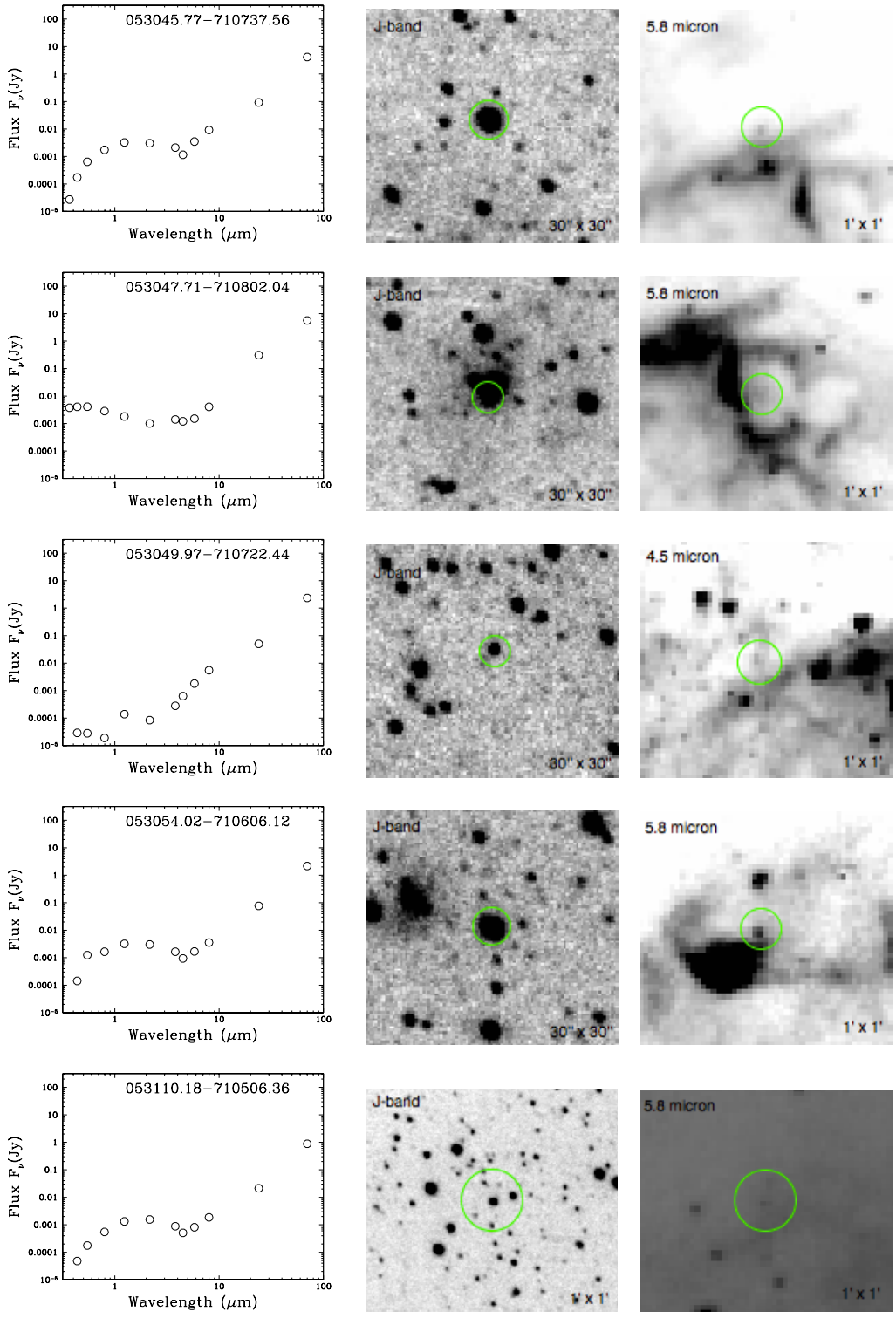

Figure 4.20 A continuation of the previous figure. SEDs and sample multiwavelength images for the YSO candidates classified as "SD", due to a combination of emission from a stellar source and dust emission, with stellar emission dominating. The wavelength being displayed is at the upper left of each box, and the field of view is at the lower right. The green circles show the source being examined and are not indicative of the flux aperture used in photometry.

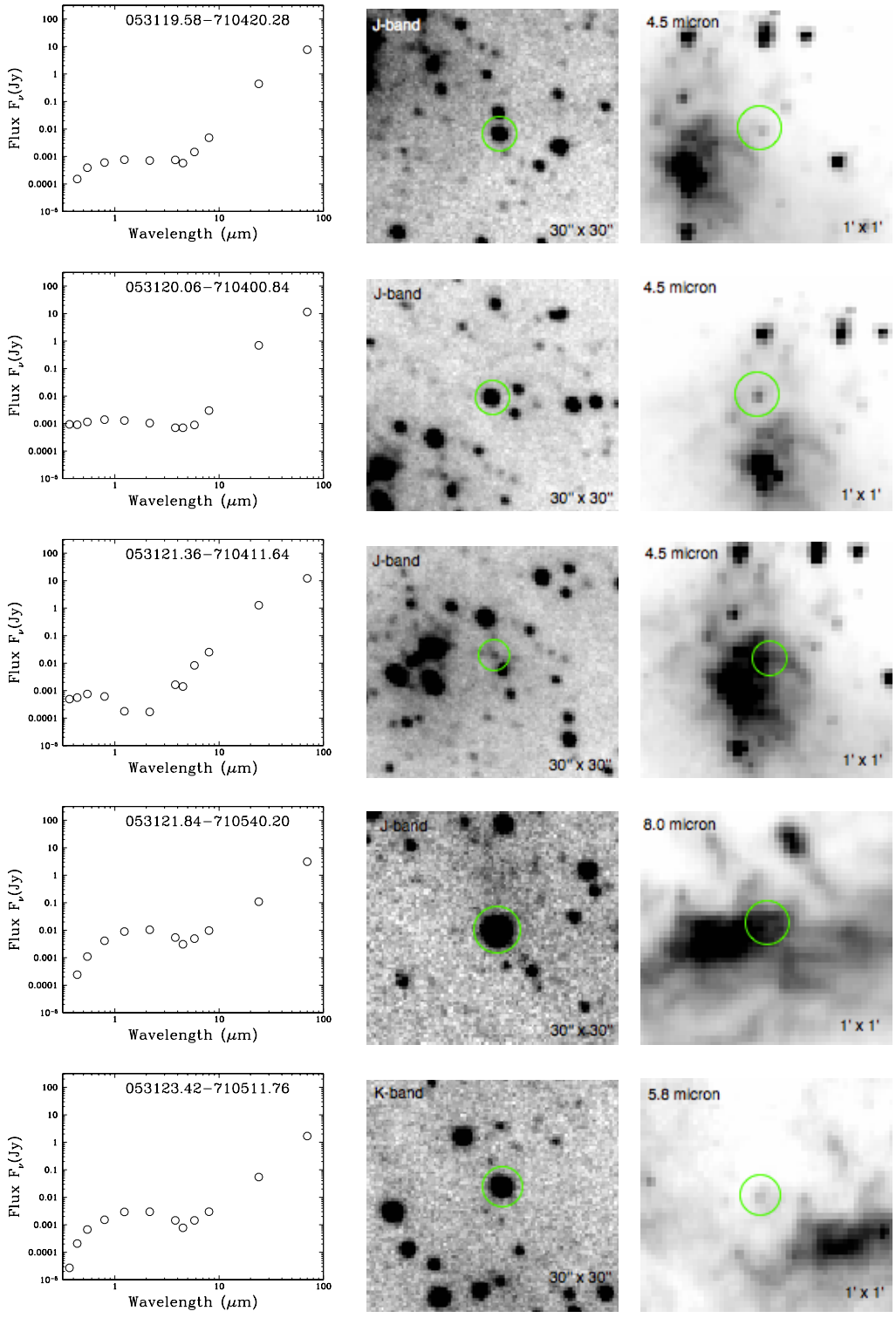

Figure 4.21 A continuation of the previous figure. SEDs and sample multiwavelength images for the YSO candidates classified as "SD", due to a combination of emission from a stellar source and dust emission, with stellar emission dominating. The wavelength being displayed is at the upper left of each box, and the field of view is at the lower right. The green circles show the source being examined and are not indicative of the flux aperture used in photometry.

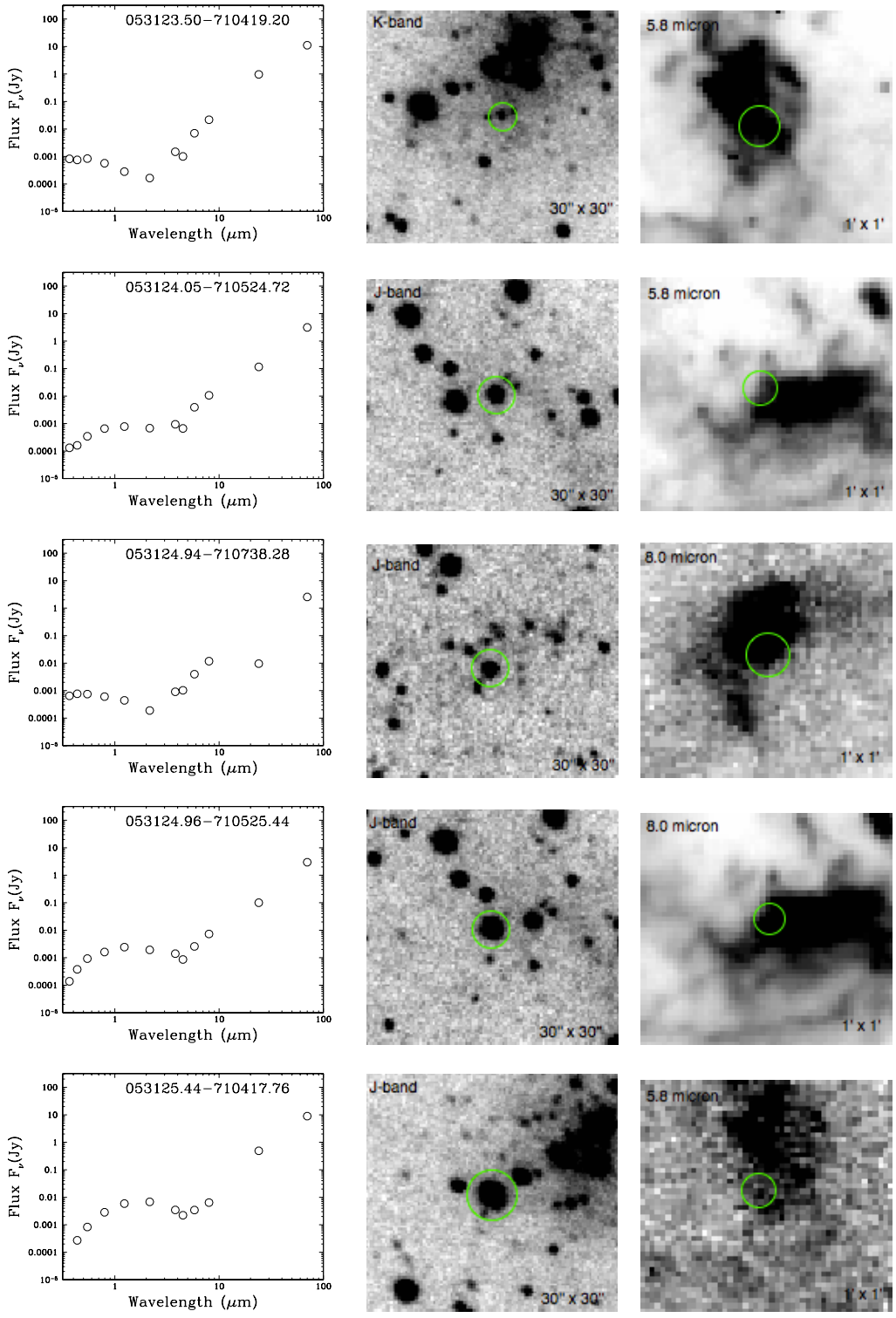

Figure 4.22 A continuation of the previous figure. SEDs and sample multiwavelength images for the YSO candidates classified as "SD", due to a combination of emission from a stellar source and dust emission, with stellar emission dominating. The wavelength being displayed is at the upper left of each box, and the field of view is at the lower right. The green circles show the source being examined and are not indicative of the flux aperture used in photometry.

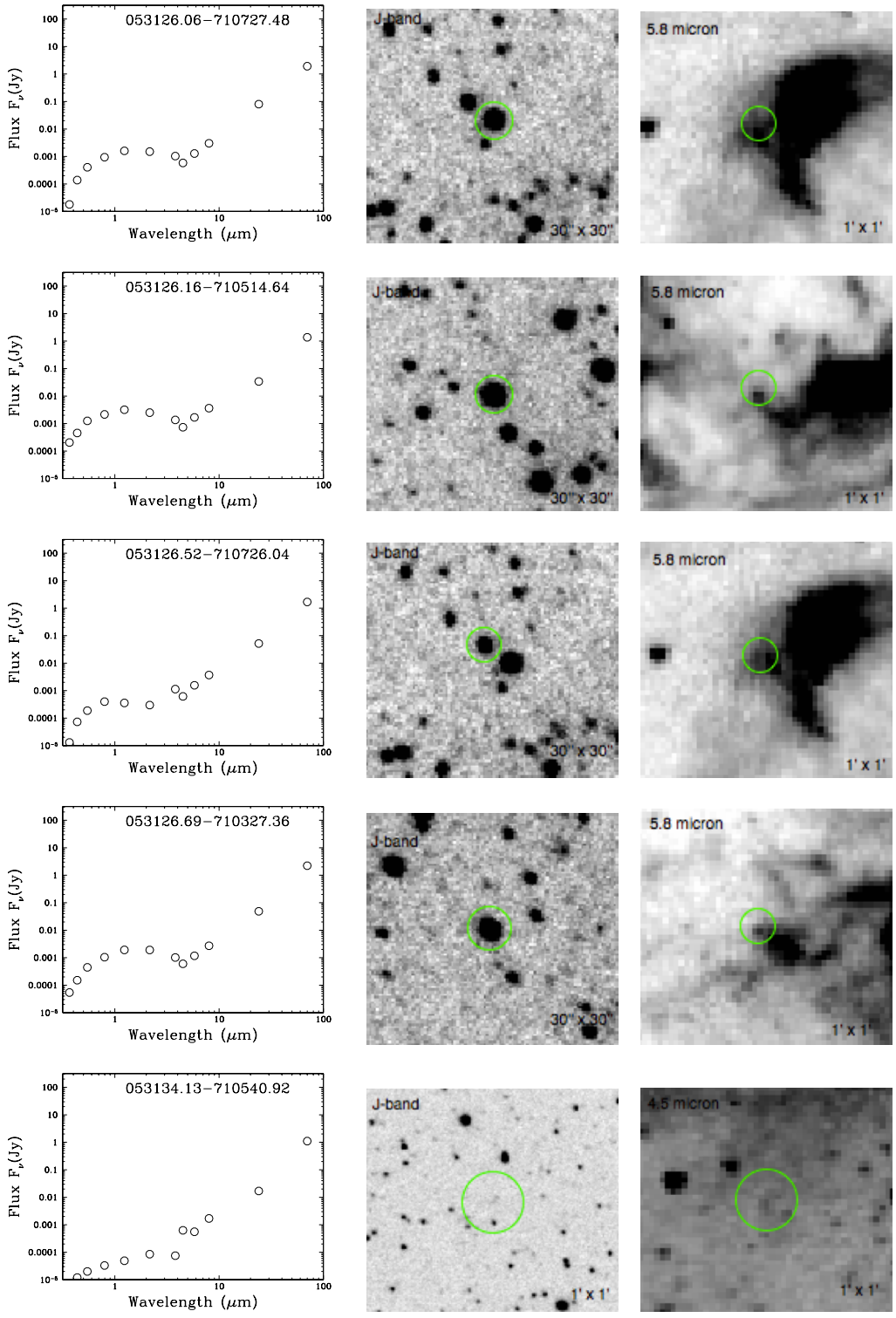

Figure 4.23 A continuation of the previous figure. SEDs and sample multiwavelength images for the YSO candidates classified as "SD", due to a combination of emission from a stellar source and dust emission, with stellar emission dominating. The wavelength being displayed is at the upper left of each box, and the field of view is at the lower right. The green circles show the source being examined and are not indicative of the flux aperture used in photometry.

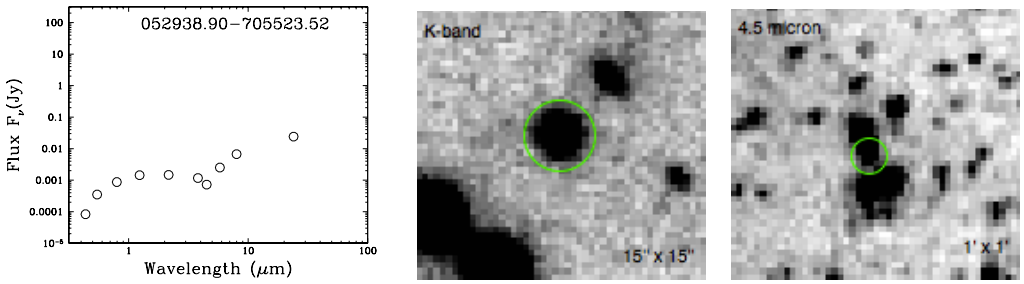

Figure 4.24 SED and sample multiwavelength images for the YSO candidate classified as "SG", due to a combination of emission from a stellar source and a nearby galaxy, with stellar emission dominating. The wavelength being displayed is at the upper left of each box, and the field of view is at the lower right. The green circles show the source being examined and are not indicative of the flux aperture used in photometry.

4.2.5 Final YSO Candidates

After identifying and removing galaxies, dust clumps, stellar sources, and objects that were a combination of these from my list of YSO candidates, I was left with 51 candidates to consider. In the next section I describe how I classified these remaining sources, hereafter called YSOs, as "Definite" YSOs, "Probable" YSOs, and "Possible" YSOs. I also explain how I gave each of them a preliminary evolutionary classification.

4.3 Classifying Young Stellar Objects

After eliminating probable non-YSOs from the list of candidates, I assigned each YSO a two-fold classification. This classification of each source is based on: (1) how confident I am that the source is a YSO and (2) how evolved the YSO appears to be.

In the first part of the classification, each YSO was given a "definite", "probable" or "possible" designation. I examined each source to determine if I could convincingly rule out that it was anything but a YSO. A source that is called a "definite" YSO, therefore, is one that I am convinced is not any other type of object. These receive a classification of "C", for "Candidate". A "probable" YSO is one that appears to be a YSO but I cannot rule out that it could be another type of object. So, for example, a source with a "CG" designation is one that I deem to most likely be a YSO, but I cannot rule out that it might be a galaxy. Similarly, a "possible" YSO is a source that looks to most likely be a non-YSO, but I cannot rule out the possibility of it being a YSO. A "possible" YSO designation example would therefore be "GC". Below I describe in detail the process of giving each YSO one of these designations.

In the second part of the classification, I roughly classified each YSO according to how evolved it seemed to be. Lada (1987) [4] proposed a system of morphological classification for low-mass YSOs that resembles an evolutionary sequence. In this system, low-mass YSOs

are classified according to features of their SEDs. Chen et al. (2009) [2] suggests a similar system for classifying massive YSOs, using types instead of classes. In this system, a Type I SED would rise steeply from near-infrared to 24-micron and beyond, suggesting dominant emission from a circumstellar envelope. A Type I YSO would not be visible in optical or in J-band images. A Type II YSO SED would show a low peak at optical wavelengths and a high peak between 8 and 24 μm. The low optical peak represents emission from the inner source and the high infrared peak represents emission from the circumstellar disk. For a Type II YSO, the envelope is mostly dissipated. A Type III YSO SED would show bright optical emission and some dust emission, showing that the young star is largely exposed but still surrounded by some circumstellar material. A number of sources might also resemble two different types, and could be classified as Type I/II, for example. Examples of SEDs for these main evolutionary types are given in Figure 4.25. Since my search for YSOs in N206 is biased toward intermediate- and high-mass YSOs, I followed this typing system. Below I describe the process of assigning these types to each of the remaining YSO candidates.

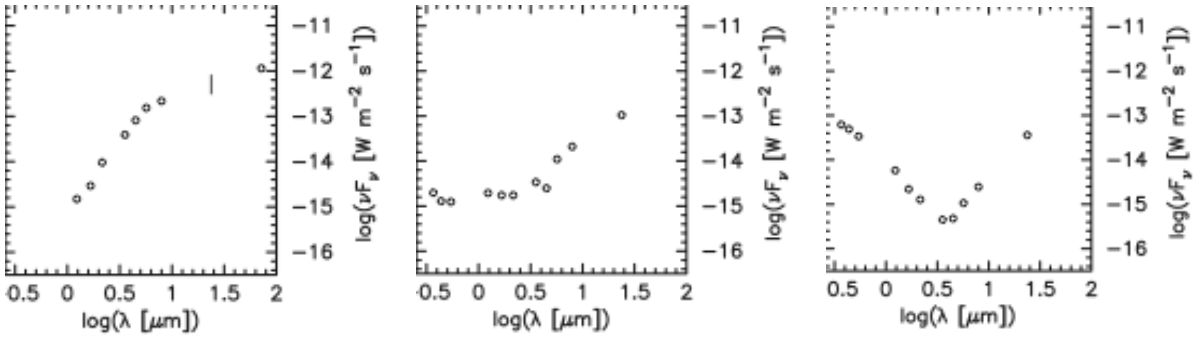

Figure 4.25 Example SEDs of evolutionary YSO types from Chen et al. (2009) [2]. From left to right: Type I YSO, Type II YSO, Type III YSO.

4.3.1 "Definite" Young Stellar Objects

I found 21 of the YSO candidates to be "definite" YSOs, for which I could convincingly rule out each source being either a background galaxy, a star, or a dust clump. With the exception of the Type III "definite" YSO and the Type II/III "definite" YSOs (discussed below), the SEDs of these YSOs are rising, and there is no clear shape that would suggest a stellar photosphere; I have therefore ruled out that these sources are stars or galaxies. Additionally, for each of the "definite" YSOs, a clear source is seen, making it easy to rule out that any of these sources are diffuse dust clumps.

Four of these "definite" YSOs (053022.46-710742.96, 053047.16-710742.96, 053048.79-710735.04, and 053117.50-710354.72) I further classified as being Type I, or early-type YSOs, based primarily on the shapes of their SEDs. The emission from these is thought to mostly come from an envelope of gas and dust surrounding the star. All four of the source SEDs (seen in Figure 4.26) are steeply rising from near-infrared through 70 μm. There were no flux values found in the optical for these sources. For the second of these YSOs, 053047.16-710742.96, no J- or Ks-band flux values were detected either. The Hα images in Figure 4.26 show that the first three sources appear to be in or behind dark clouds, and the fourth source is in a bright Hα region. In the J-band images for these four YSOs, a source is either not detectable or barely detectable. A clear source is seen for these four YSOs at both [4.5 μm] and [8.0 μm]. The first and fourth of these sources look to be among other sources or dust at [24 μm], but the second and third sources have clear [24 μm] counterparts, as seen in the figure.

I found that five of the "definite" YSOs (052954.38-710506.36, 052958.56-710844.88, 053021.29-705437.44, 053021.55-705409.00, and 053035.69-710137.20) fit the description of a Type II YSO, which is more evolved than a Type I. The emission from this YSO type is coming from a central source and a circumstellar disk, as the dust envelope has dissipated. I

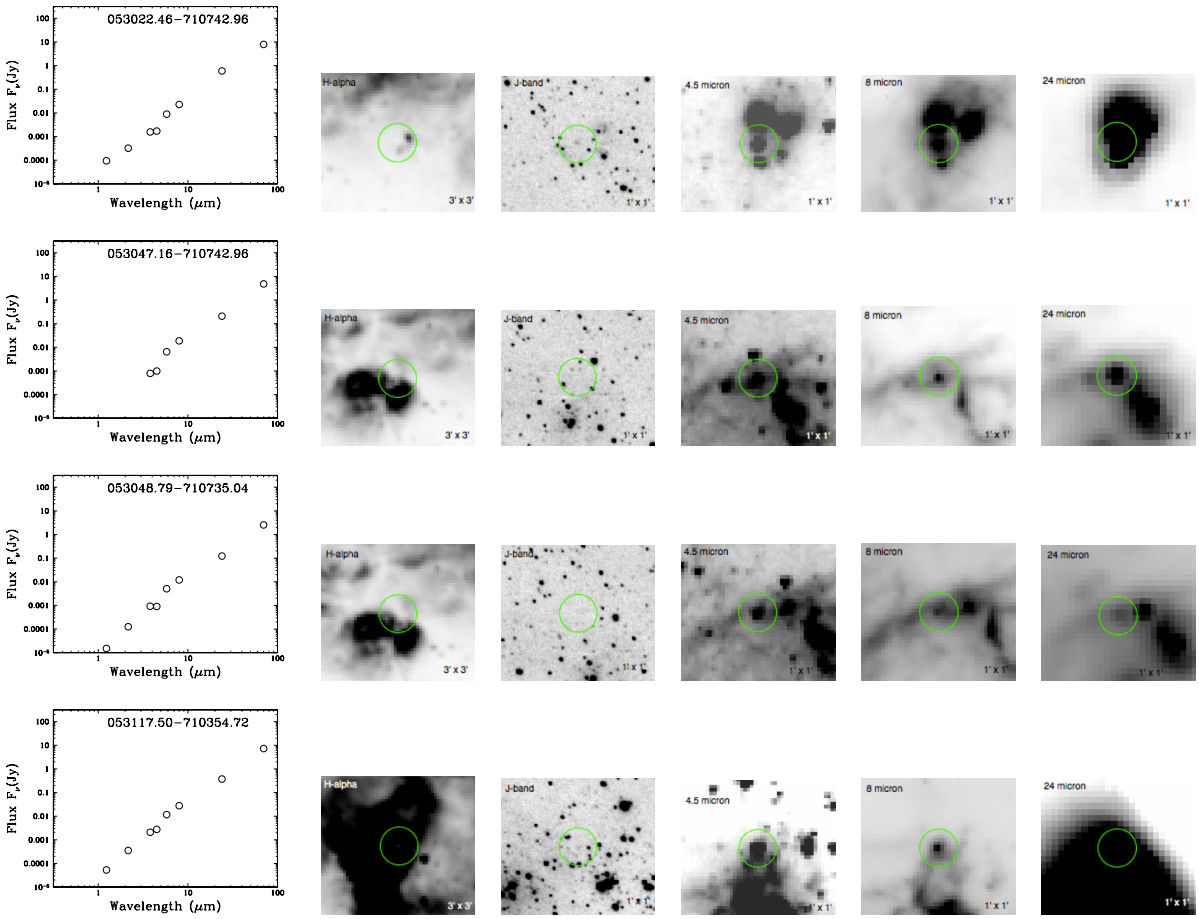

Figure 4.26 SEDs and sample multiwavelength images for the YSO candidates classified as "definite" Type I YSOs. The wavelength being displayed is at the upper left of each box, and the field of view is at the lower right. The green circles are centered on the source being examined and are not indicative of the flux aperture used in photometry.

again chose this classification based primarily on the SEDs. These 5 SEDs show a low peak in the optical and near-infrared wavelengths, and a high peak in the mid- to far-infrared wavelengths. The SEDs and selected images for these sources are given in Figure 4.27. The images selected show a brightening up of each source from the near-infrared J band through [8 μm]. The first and the fourth of these show noticeable dimming of the sources at [24 μm] in the images given.

Another 5 of the "definite" YSOs (053020.40-705430.24, 053020.66-710738.64, 053056.23-710602.52, 053056.71-710557.84, and 053105.62-710700.48) were classified as Type I/II, between the two types. This was largely because they had optical points in their SEDs, but their SEDs were steeply rising. They therefore show signs of being in between the two types and are shown in Figure 4.28.

One of these "definite" YSOs (053105.23-710709.84) was classified as a more evolved Type III YSO, where there is clear stellar emission from the central source, but the source is still surrounded by appreciable amounts of circumstellar material. As shown in Figure 4.29, this YSO has a strong stellar component to its SED, the hump that peaks at near-infrared wavelengths. There is also a good contribution from dust at the longer wavelengths. The images show the source as being bright in the J band, then getting dimmer through the mid-infrared. The [24 μm] image looks a little brighter due to the contributing dust at that wavelength.

Two "definite" YSOs (052934.30-710905.40 and 052935.23-710856.76)appeared to be between Types II and III, classified as Type II/III. Unfortunately, these sources were not in the ISPI J- and Ks-band images, so no near-infrared images are available for them. SEDs and selected images for these are given in Figure 4.30.

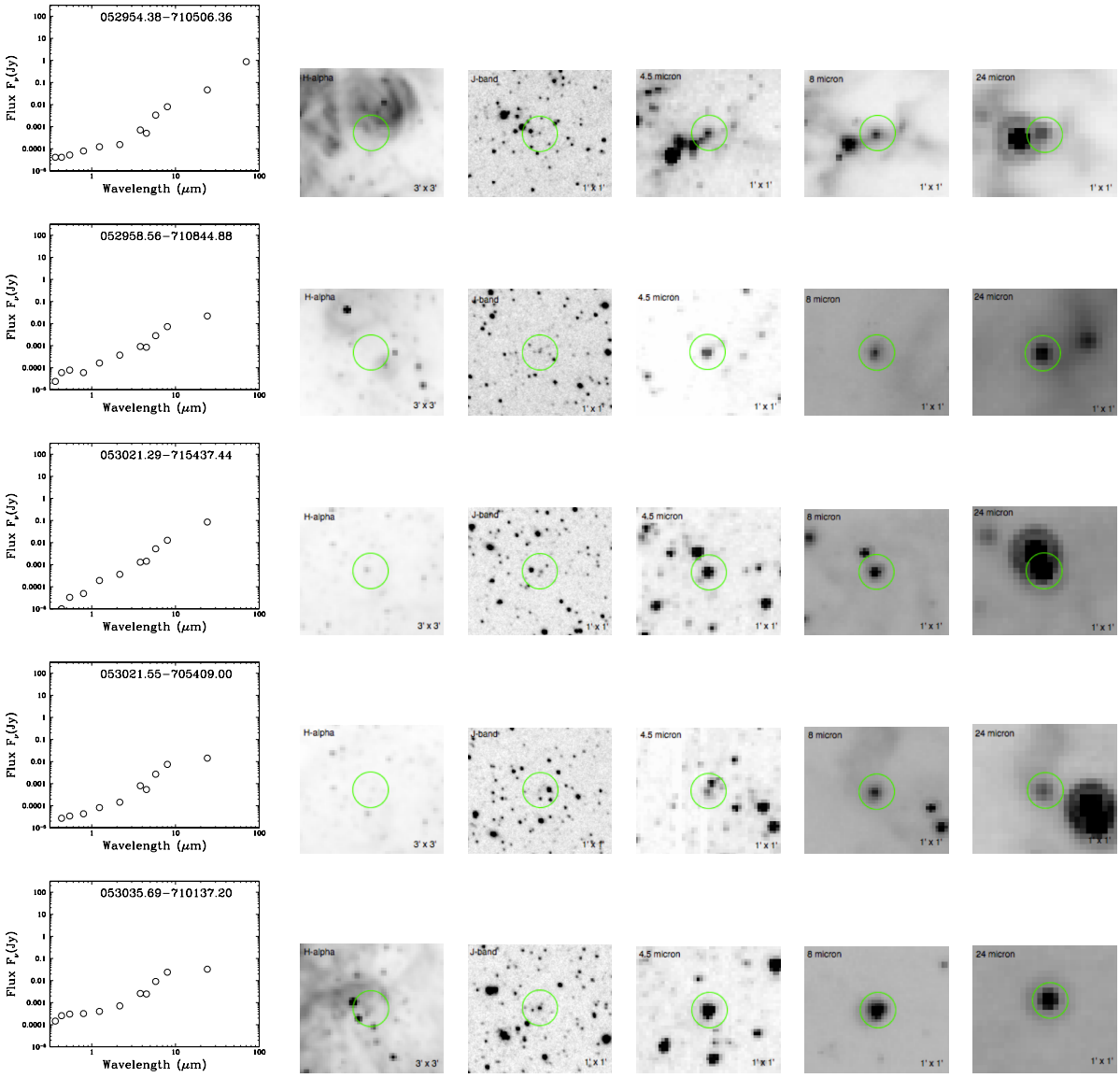

Figure 4.27 SEDs and sample multiwavelength images for the YSO candidates classified as "definite" Type II YSOs. The wavelength being displayed is at the upper left of each box, and the field of view is at the lower right. The green circles are centered on the source being examined and are not indicative of the flux aperture used in photometry.

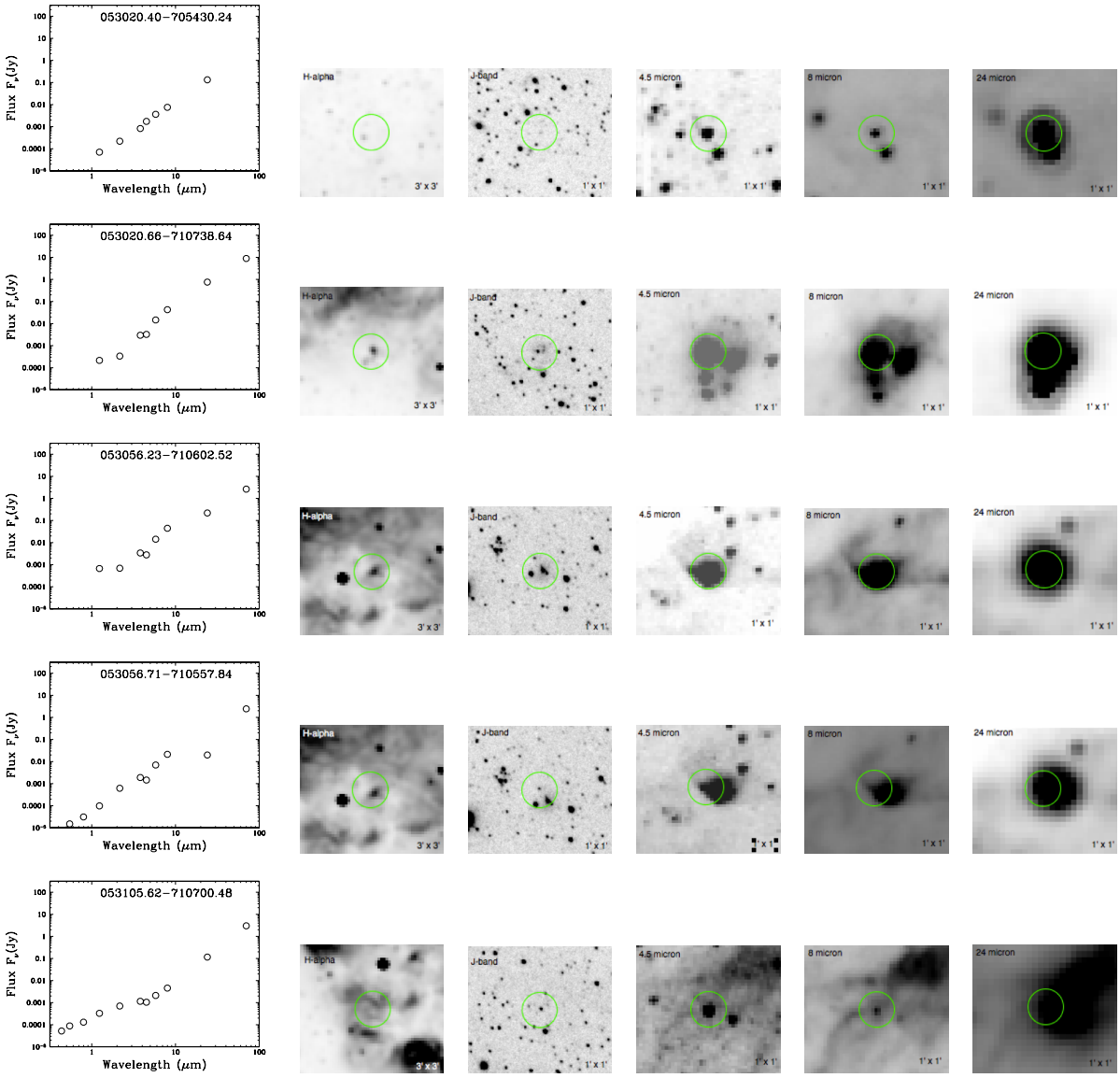

Figure 4.28 SEDs and sample multiwavelength images for the YSO candidates classified as "definite" Type I/II YSOs. The wavelength being displayed is at the upper left of each box, and the field of view is at the lower right. The green circles are centered on the source being examined and are not indicative of the flux aperture used in photometry.

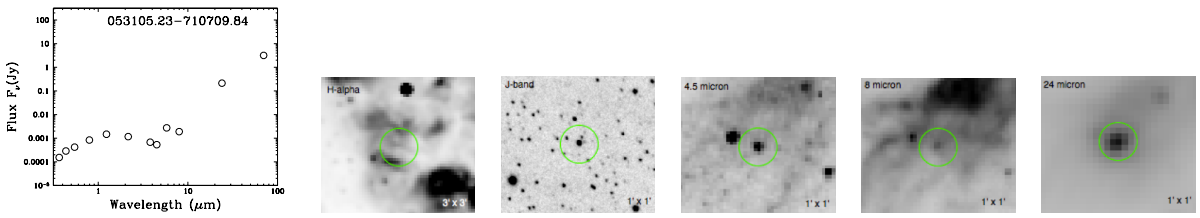

Figure 4.29 SEDs and sample multiwavelength images for the YSO candidate classified as a "definite" Type III YSO. The wavelength being displayed is at the upper left of each box, and the field of view is at the lower right. The green circles are centered on the source being examined and are not indicative of the flux aperture used in photometry.

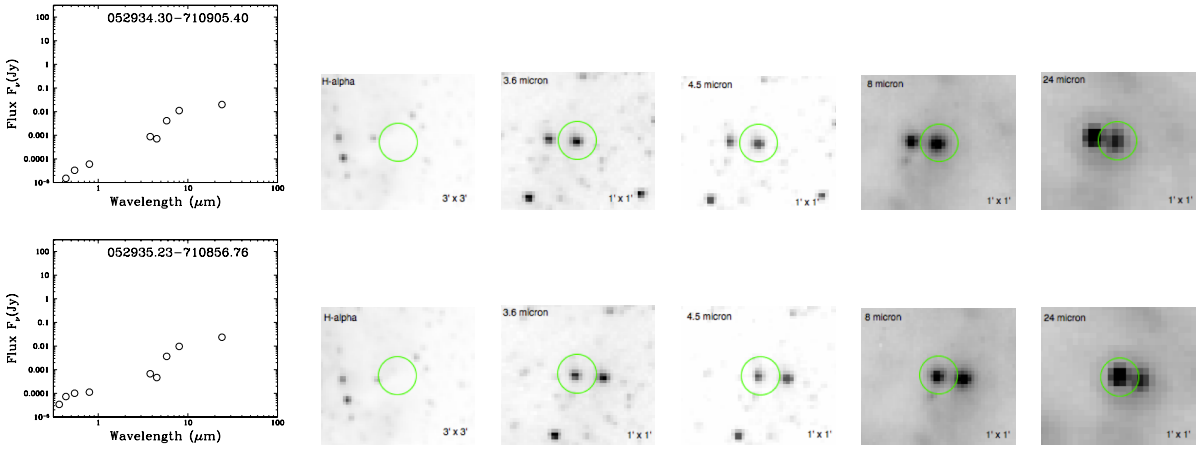

Figure 4.30 SEDs and sample multiwavelength images for the YSO candidates classified as a "definite" Type II/III YSOs. The wavelength being displayed is at the upper left of each box, and the field of view is at the lower right. The green circles are centered on the source being examined and are not indicative of the flux aperture used in photometry.

I found that four of the "definite" YSOs (053023.11-710556.40, 053046.75-710844.88, 053123.57-710735.40, and 053124.31-710735.76) looked like a single source in the longer wavelength images, but in the higher resolution *J*- and *Ks*-band images, they were resolved into multiple sources. I call these multiple YSOs, and their SEDs and selected images are in Figure 4.31. In this figure, both a *J*- and a *Ks*-band image is given for each source to illustrate the multiplicity of the source. Source 053023.11-710556.40 is in a dense Hα region, and was classified as a Type II YSO due to the shape of its SED. For source 053046.75-710844.88, the near- and mid-infrared images show two sources instead of one. I classified this source as a Type I/II YSO, because its SED has a Type II shape, but there are no optical flux points. The near-infrared images of source 053123.57-710735.40 show at least three sources; it looks like a small cluster of YSOs. This source was classified as Type I due to the brightnesses in the images and the shape of the SEDs. Lastly, source 053124.31-710735.76 is in a dark cloud, as shown in the Hα images. In the near-infrared images it looks like four sources instead of one, and it has a Type II SED.

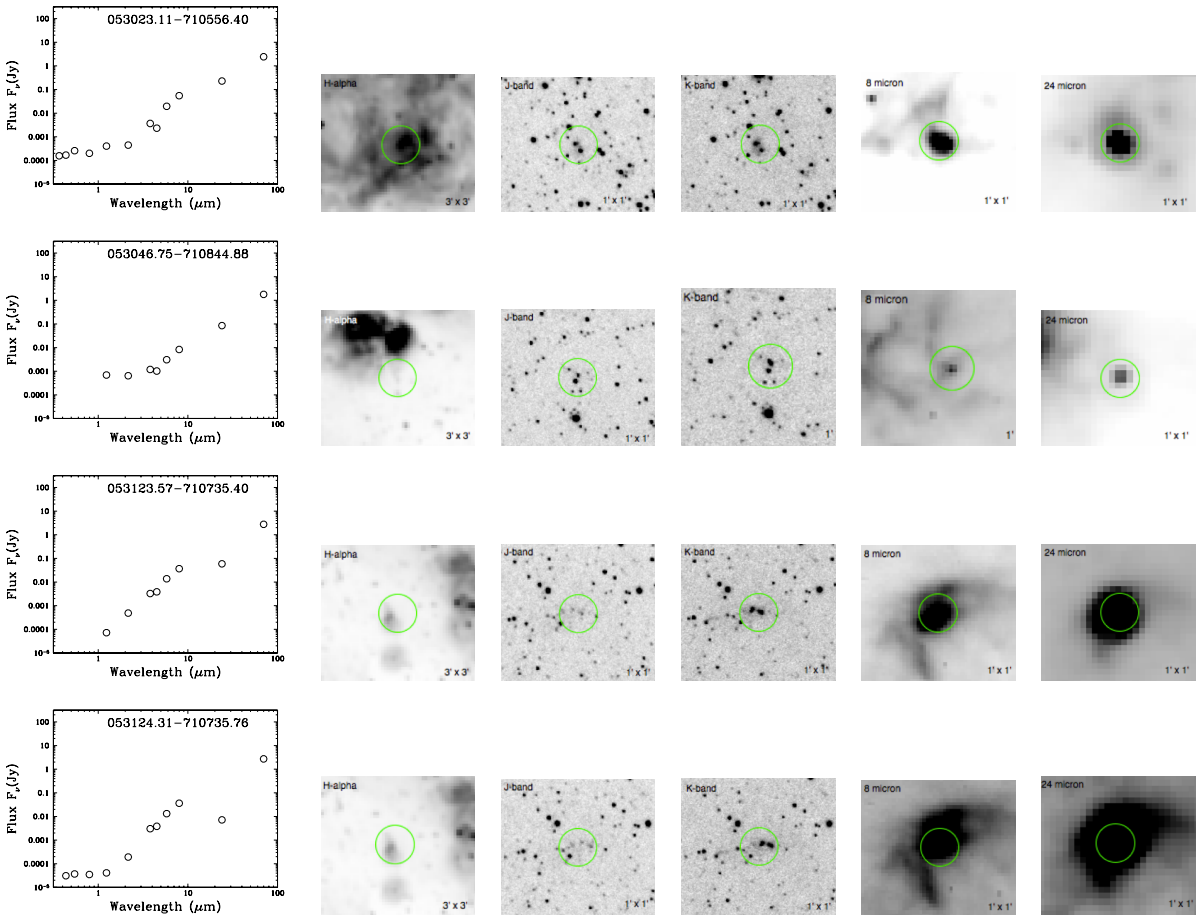

Figure 4.31 SEDs and sample multiwavelength images for the YSO candidates classified as a "definite" multiple YSOs. The wavelength being displayed is at the upper left of each box, and the field of view is at the lower right. The green circles are centered on the source being examined and are not indicative of the flux aperture used in photometry.

4.3.2 "Probable" Young Stellar Objects

I found 14 "probable" YSOs, which means that they seemed most likely to be YSOs, but I could not rule out that they could be another type of object as well. I determined three of these "probable" YSOs (053046.61-710751.60, 053049.51-710804.92, and 053050.23-710813.56) to be Type I YSOs. Their SEDs are rising steeply, and they do not have any optical flux points. All three of these "probable" Type I YSOs were given the classification "CD", meaning that I could not rule out the possibility that they were dust clumps. Each looks like a clear source at shorter wavelengths, as seen in the [4.5 μm] images in Figure 4.32, but in the longer wavelengths, they look like they are either in very dusty regions or like they might be clumps of dust themselves. Seeing a clear point source at shorter wavelengths is what distinguished these YSOs as being "probable" instead of "possible".

One "probable" YSO (053117.62-710536.24) was classified as a Type II YSO. This is because its SED seems to have a low peak at optical wavelengths and a high peak and far-infrared wavelengths, as show in Figure 4.33. Just like the Type I "probable" YSOs, this YSO is classified as a "CD". This YSO still looks like a clear source at longer wavelengths, but it looks like the surrounding dust is contributing significantly to the fluxes at these wavelengths.

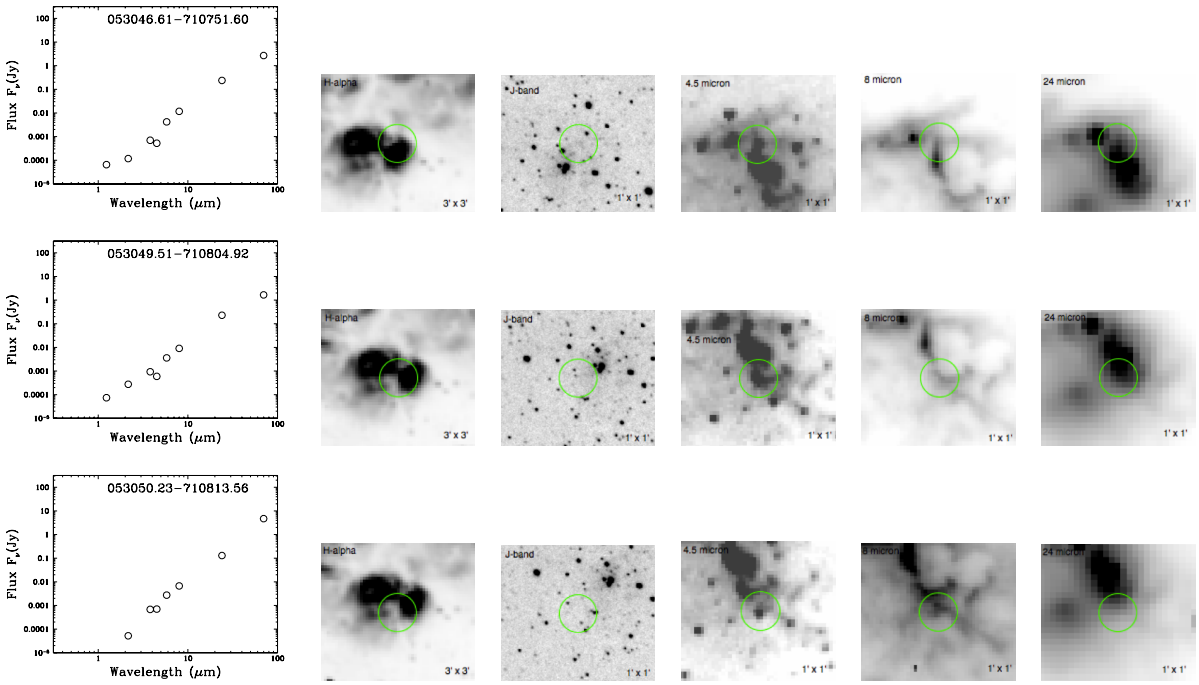

Figure 4.32 SEDs and sample multiwavelength images for the YSO candidates classified as a "probable" Type I YSOs. The wavelength being displayed is at the upper left of each box, and the field of view is at the lower right. The green circles are centered on the source being examined and are not indicative of the flux aperture used in photometry.

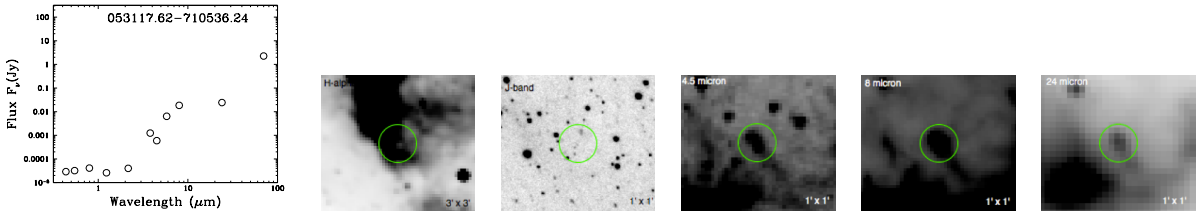

Figure 4.33 SEDs and sample multiwavelength images for the YSO candidate classified as a "probable" Type II YSO. The wavelength being displayed is at the upper left of each box, and the field of view is at the lower right. The green circles are centered on the source being examined and are not indicative of the flux aperture used in photometry.

I determined five of the "probable" YSOs (053018.60-710800.60, 053056.69-710603.60, 053104.20-710735.76, 053105.11-710756.28, and 053127.53-710739.00) to be of Type I/II. The first of these, as seen in Figure 4.34, has optical flux points in its SED, but the SED is rising steeply and does not show any peaks. The other six do not have optical flux values, but the shapes of their SEDs do suggest a low peak at shorter wavelengths and a high peak at longer wavelengths.

The first source in Figure 4.34, 053018.60-710800.60, I classified as a "CG", because I could not rule out the possibility of it being a galaxy. It does not have any optical flux values, but there is a clear near- and mid-infrared source in its images; this compelled me to classify it as a "probable" YSO. However, it looks possibly extended in the higher resolution *J*- and *Ks*-band images, which means it could be a galaxy. Additionally, the shape of its SED could resemble that of a Type I/II YSO or that of a galaxy with no optical flux values.

Source 053056.69-710603.60 in Figure 4.34 is very likely a YSO with a nearby galaxy contributing to its SED. This nearby galaxy can be seen in the *J*-band image in the figure, to the right of the central source. This source is therefore also given a classification of "CG".

The next source, 053104.20-710735.76, has no optical flux points in its SED, and is brighter in the *Ks* band than in the *J* band, which leads me to the "probable" YSO classification. However, there is not a clear distinct source in the images after 8 μm, so I cannot rule out that it could be a heavily obscured star in the dust. I therefore give this source a classification of "CSD".

Source 053105.11-710756.28 in Figure 4.34 brightens up toward longer wavelengths like a YSO, but in the mid-infrared images it looks possibly diffuse. This source is therefore classified as a "CD", since there is a possibility of it being a dust clump.

The last source in the figure, 053127.53-710739.00, has a steeply rising SED like a YSO, but at longer wavelengths (as seen in the [8.0 μm] and [24 μm] images in Figure 4.34), the source is confused with the dust pillar that it appears to be in and this dust pillar is probably

contributing greatly to the flux values in the SED. This source is therefore classified as a "CD".

One source (053057.12-710605.04) is classified as a Type III "probable" YSO, because its SED shows a strong stellar component, as seen in Figure 4.35. This suggests that the central YSO is emerging from its surrounding material, but the longer wavelength increases in the SEDs suggest that there is still a good deal of dust in the region. However, this SED shape also resembles that of a galaxy, and while the central source does not look particularly extended in the near-infrared images, there is a nearby galaxy visible in those images that could be contributing to the SED. This source is therefore classified as a "CG".

Source 053020.26-710748.00, shown in Figure 4.36, is classified as a Type II/III "probable" YSO because its SED has characteristics of both a Type II and a Type III YSO SED. Additionally, this source is classified as a "CD", because in the longer wavelengths images, it looks like dust makes a significant contribution to the flux values in the SED.

Three "probable" YSOs (052956.54-710440.08, 053047.88-710755.20, and 053117.45-710533.72) look in the higher resolution near-infrared images to be possible multiples (as seen in the J-band images in Figure 4.37). The first of these, 052956.54-710440.08, is classified as a "CSD" of Type II. The other two sources are both classified as "CD", because it looks like dust is greatly contributing to their SEDs. The second source, 053047.88-710755.20, is given a Type III designation, and the last source, 053117.45-710533.72, is a Type I/II.

4.3.3 "Possible" Young Stellar Objects

I found 16 of the YSO candidates to be "possible" YSOs, meaning that they looked likely to be another type of object, but I could not rule out that they could be YSOs. Five of these are Type I "possible" YSOs; their SEDs do not have any optical points, and they are steeply rising (as seen in Figure 4.38). These are also all given the classification "DC", because they

cannot be easily distinguished as a distinct source instead of a diffuse dust area.

Five of the "possible" YSOs (053003.96-710512.84, 053027.41-705421.96, 053115.84-710508.16, 053122.78-710409.84, and 053130.36-710404.80) are classified as Type II, according to their SEDS (as seen in Figure 4.39). All five SEDs exhibit a low peak at optical wavelengths and a high peak at longer wavelengths.

The first source in this group, 053003.96-710512.84, has an Hα counterpart in the images, as well as optical flux points. It looks to be fading into dust toward longer mid-infrared wavelengths in the images, which leads to a classification of a star in dust. However, there does seem to be a clear counterpart at 24 μm, so I cannot rule out that it could be a YSO. This source is therefore classified as "SDC".

The other four sources have a slight galaxy shape to their SEDs, and they look like they could be extended in the near-infrared images. The sources do appear to brighten through the mid-infrared images, though, and so I cannot rule out a YSO classification. These sources are classified "GC".

One "possible" YSO's SED seemed to fit the Type I/II SED shape. This source, 052938.38-710042.12 (Figure 4.40, was classified as a "GC", because it looks extended in the near-infrared images. It does not, however, have any optical flux values in its SED, so I cannot rule out that it could be a YSO.

Four "possible" YSOs (052945.38-710501.68, 053015.84-710758.80, 053036.22-710646.08, and 053121.46-710407.32) were classified as Type III YSOs. The first two of these, as seen in Figure 4.41, were classified as "GC", because they look possibly extended in the near-infrared images. Their SEDs could also be shaped like those of galaxies. Also, there does not appear to be a distinct source in the far-infrared. The third source, 053036.22-710646.08, was classified as an "SDC", because it has an Hα counterpart, and it appears to possibly be fading in the images toward longer wavelengths. The last of these sources is classified as a "DSC", because it looks like mostly contribution by dust with a stellar component. It also

has a clear source at 24μm, however, which leads me to not rule out a YSO.

One "possible" YSO, shown in Figure 4.42, looked like it could be multiple sources. The J-band image in the figure shows possibly two sources in the center. It is classified as a Type II, due to the shape of its SED. Additionally, it is classified as a "DSC", because it looks from the images as if most of the SED is due to dust emission, with an embedded star. I cannot, however, rule out it being a YSO.

4.4 Characterizing YSOs Through Model Fitting

In addition to assigning classifications to the YSOs, I fit their SEDs to SEDs for model YSOs. I performed the fitting using the Online SED Model Fitter provided by Robitaille et al. (2006) [51]. This online model fitter includes SEDs for 20,000 different model YSOs, each from 10 different inclination angles. Each model assumes a stellar core, a flared accretion disk, and a gravitationally flattening infalling envelope. The fitting tool fits 14 different parameters. The stellar parameters include the star's mass, radius, temperature, and age. The disk parameters are the disk accretion rate, its mass, inner radius, outer radius, scale height factor, and flaring angle. The infalling envelope parameters include the envelope accretion rate, outer radius, cavity density, cavity opening angle, and ambient density. The input parameters required by the model fitter are the fluxes for the YSOs at the available wavelengths, along with their uncertainties. The uncertainty for each flux value is the quadratic sum of the measurement error and the calibration error. I input the flux and uncertainty values in units of mJys, converted from the magnitudes given in Table 4.1.3. This table also gives the measurement error for each flux value, and the calibration errors are given as percentages of the fluxes in Table 3.2.

A word of caution should be given here concerning using physical parameter values output by the fitting. This is because 14 parameters were being fit by, at most, 12 data points. I

performed the fits because I wanted to compare against these models and begin to constrain the physical parameters of the YSOs. For the most part, my evolutionary classifications matched well with those of the models, but the results of the fits should not be heavily relied upon.

There are 43 YSOs in my sample that appear to be single sources, so I fit the SEDs of these YSOs to the model YSO SEDs to analyze them. The SED flux values that I input for each YSO were compared against the YSO models in the fitter. The best-fit models are selected using chi-squared statistics, with the best-fit model being that with the lowest chi-squared value. The probable ranges for the physical parameters of each YSO that I fit was found using the ten best-fit models for the YSO. Table 4.2 gives inferred parameters for each of the 43 YSOs that I fit.

In Table 4.2, YSO Name is the name I assigned for the YSO, Type is the evolutionary type I assigned each YSO, and $M_\star$ Range gives the range of central source masses for the ten models that were the best fit to the YSO. Stage Range gives a range of evolutionary stages defined by Robitaille et al. (2006) [51] for the ten YSO models that were the best fit to the YSO. These stages are defined using the parameters $\dot{M}_{env}$ (the envelope accretion rate), $M_\star$ (the central source mass), and M_{disk} (the circumstellar disk mass). In this evolutionary sequence, a Stage I YSO has $\dot{M}_{env}/M_\star > 10^{-6}$ yr^{-1}. Stage I YSOs have significant rotationally flattening infalling envelopes and may have disks. A Stage II YSO has $\dot{M}_{env}/M_\star < 10^{-6}$ yr^{-1} and $M_{disk}/M_\star > 10^{-6}$ yr^{-1}. These YSOs have optically thick disks and possibly very thin envelope remnants. Stage III YSOs have $\dot{M}_{env}/M_\star < 10^{-6}$ yr^{-1} and $M_{disk}/M_\star < 10^{-6}$ yr^{-1}. A Stage III YSO has an optically thin disk. Also given in Table 4.2 are physical parameters of the YSO model that was the best fit. These are the mass, temperature and radius of the central source; the age of the YSO; the envelope and disk accretion rates; the disk mass; the angle of inclination for viewing the system; the total luminosity of the YSO; and the estimated absorption.

YSO Name	Type	$M_\star$ Range ($M_\odot$)	Stage Range	Physical Parameters of Best-Fit Model									
				$M_\star$ ($M_\odot$)	$T_\star$ (K)	$R_\star$ ($R_\odot$)	Age (yr)	$\dot{M}_{env}$ ($M_\odot$/yr)	$\dot{M}_{disk}$ ($M_\odot$/yr)	M_{disk} ($M_\odot$)	i (°)	L_{tot} ($L_\odot$)	A_V (mag)
052934.30-710905.40	II/III	7-8	II	8	23000	3.6	3E+06	0.0E+00	5.7E-08	3.8E-02	76	3300	3.4
052935.23-710856.76	II/III	7-8	I,II	8	8600	17.3	1E+05	2.7E-05	2.8E-07	4.4E-02	70	1400	0.9
052938.38-710042.12	I/II	4-7	I	7	4700	29.7	1E+05	2.0E-05	1.9E-08	3.0E-03	41	390	0
052945.38-710501.68	III	7-8	I	7	4800	30.3	8E+04	7.7E-04	2.3E-08	6.7E-02	18	450	0.5
052954.38-710506.36	II	7-9	I,II	9	8500	21.4	6E+04	6.7E-04	1.1E-06	2.3E-01	41	2200	1.2
052958.56-710844.88	II	7-8	I,II	8	8600	17.3	1E+05	2.7E-05	2.8E-07	4.4E-02	70	1400	1.2
053003.96-710512.84	II	11	III	11	26000	4.1	3E+06	0.0E+00	2.1E-13	1.1E-07	49	7400	0.4
053015.84-710758.80	III	5-8	I	8	4700	36.3	4E+04	5.1E-05	3.4E-06	3.5E-01	18	588	1.2
053018.60-710800.60	I/II	9-10	I,III	9	4600	54.9	1E+04	1.4E-04	4.1E-06	7.0E-02	18	1200	0
053019.68-710750.16	I	21-46	I	46	14000	87.8	3E+03	2.8E-03	0.0E+00	0.0E+00	32	260000	0.4
053020.26-710748.00	II/III	11-17	I	14	6600	70.8	1E+04	2.3E-03	3.8E-05	8.9E-01	18	8700	0.2
053020.40-705430.24	I/II	7-14	I	10	6800	37.3	3E+04	3.9E-03	4.6E-08	5.3E-03	18	2700	5.2
053020.66-710738.64	I/II	15-29	I,II	17	33000	5.3	1E+06	0.0E+00	8.7E-07	1.5E-01	87	32000	0
053021.29-705437.44	II	9-24	I	10	6800	37.3	3E+04	3.9E-03	4.6E+08	5.3E-03	18	2700	1.4
053021.55-705409.00	II	6-7	II	6	19000	3.0	4E+06	0.0E+00	5.7E-07	8.7E-02	41	1100	2.6
053022.46-710742.96	I	12-36	I	33	12000	80.6	4E+03	1.7E-03	0.0E+00	0.0E+00	41	130000	0
053027.41-705421.96	II	6	II	6	18000	2.9	5E+06	0.0E+00	1.4E-08	3.7E-02	32	766	1.5
053035.69-710137.20	II	8-9	I,II	9	24000	3.7	2E+06	0.0E+00	1.1E-06	6.0E-02	70	4000	1.3
053036.22-710646.08	III	5-8	I	8	6000	31.8	5E+04	1.5E-03	4.0E-08	8.7E-03	18	1200	3.6
053046.61-710751.60	I	9-26	I,II,III	19	5500	176.8	5E+03	8.5E-04	0.0E+00	0.0E+00	32	26000	0
053047.16-710742.96	I	10-15	I	13	8400	40.5	2E+04	3.0E-03	1.3E-06	1.8E-02	18	7500	16.7
053048.17-710811.76	I	30-44	I	42	13000	88.2	3E+03	2.7E-03	0.0E+00	0.0E+00	57	220000	10.3
053048.79-710735.04	I	9-13	I	13	6800	57.7	2E+04	5.9E-03	8.7E-06	1.3E-02	18	6500	9.9
053049.51-710804.92	I	10-23	I	15	8900	47.3	1E+04	2.0E-04	3.0E-06	6.9E-02	87	13000	1.4
053050.23-710813.56	I	20-44	I	30	6200	314.1	2E+03	2.2E-03	0.0E+00	0.0E+00	70	140000	2.5
053056.23-710602.52	I/II	8-15	I	10	8300	28.0	4E+04	5.2E-04	2.7E-07	2.6E-03	18	3300	0.3
053056.69-710603.60	I/II	8-15	I	15	7000	71.6	1E+04	6.0E-03	5.5E-06	7.9E-03	18	11000	0.2
053056.71-710557.84	I/II	11-16	I,II	11	13000	18.3	5E+04	6.0E-05	3.0E-07	4.3E-02	81	7500	1.1
053057.12-710605.04	III	17	III	17	33000	5.3	1E+06	0.0E+00	8.7E-13	1.0E-06	63	32000	0.5
053104.20-710735.76	I/II	1-15	I	1	4000	8.0	1E+04	4.9E-06	4.7E-05	9.8E-02	18	153	1
053105.11-710756.28	I/II	8-12	I,II	11	5100	71.0	2E+04	1.8E-03	3.5E-05	2.2E-01	18	3200	3.8
053105.23-710709.84	III	9-10	I,III	10	15000	11.6	8E+04	2.8E-05	1.0E-04	5.6E-01	87	8400	0.1
053105.62-710700.48	I/II	4-11	I	4	4200	26.4	7E+03	1.2E-04	7.7E-05	3.2E-01	18	511	0
053115.84-710508.16	II	6-8	I,II	8	22000	3.4	4E+05	6.3E-05	8.3E-08	1.6E-02	18	2300	0.5
053117.50-710354.72	I	16-44	I	18	20000	17.5	2E+04	4.5E-04	0.0E+00	0.0E+00	81	48000	2.1
053117.62-710536.24	II	8-15	I,II	13	29000	4.6	2E+06	0.0E+00	4.2E-08	6.0E-02	87	14000	0.2
053120.95-710409.12	I	21-46	I	46	14000	87.8	3E+03	2.8E-03	0.0E+00	0.0E+00	32	260000	2.8
053121.46-710407.32	III	17	III	17	33000	5.3	1E+06	0.0E+00	8.7E-13	1.0E-06	63	32000	0
053121.48-710359.04	I	12-28	I	25	4500	302.7	2E+03	8.1E+04	0.0E+00	0.0E+00	41	34000	0
053122.54-710535.52	I	8-15	I,III	11	27000	4.2	3E+06	0.0E+00	5.6E+13	8.6E-07	76	8200	0.7
053122.78-710409.84	II	18-19	II,III	19	35000	5.6	9E+05	4.0E-07	3.6E-07	4.6E-02	87	40000	0
053127.53-710739.00	I/II	7-12	I,II	11	4500	76.4	8E+03	2.9E-03	2.4E-07	3.2E-02	18	2200	0
053130.36-710404.80	II	7-12	I,II,III	10	14000	12.9	8E+04	2.9E-05	9.5E-10	4.7E-03	87	5700	0

Table 4.2 Inferred Parameters of YSOs from Model YSO Fitting.

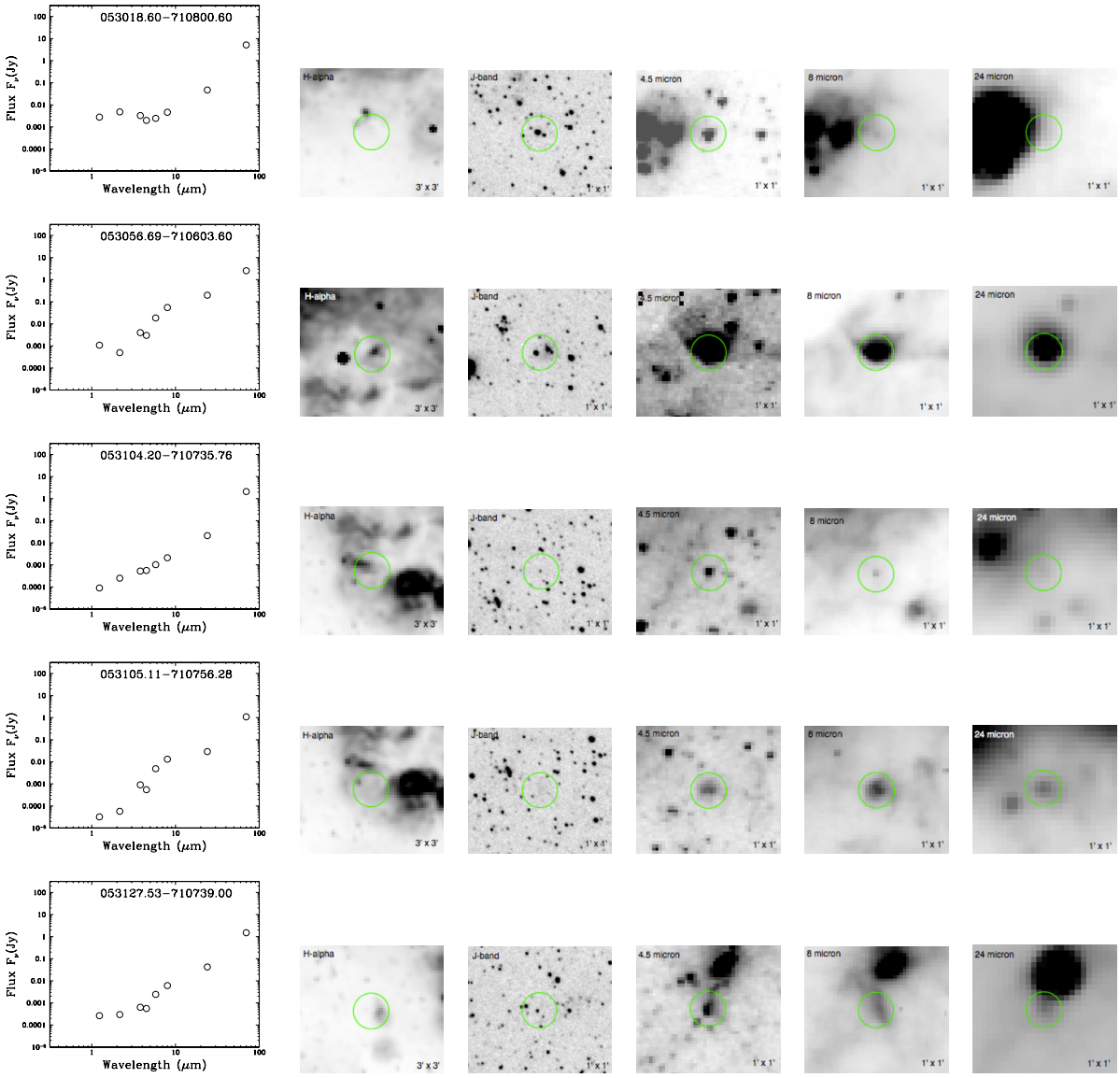

Figure 4.34 SEDs and sample multiwavelength images for the YSO candidate classified as a "probable" Type I/II YSO. The wavelength being displayed is at the upper left of each box, and the field of view is at the lower right. The green circles are centered on the source being examined.

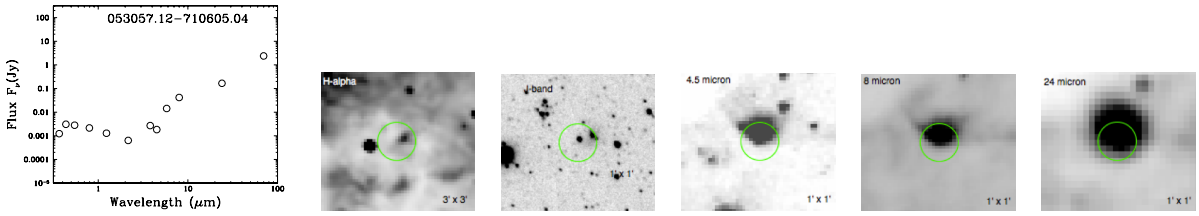

Figure 4.35 SEDs and sample multiwavelength images for the YSO candidate classified as a "probable" Type III YSO. The wavelength being displayed is at the upper left of each box, and the field of view is at the lower right. The green circles are centered on the source being examined and are not indicative of the flux aperture used in photometry.

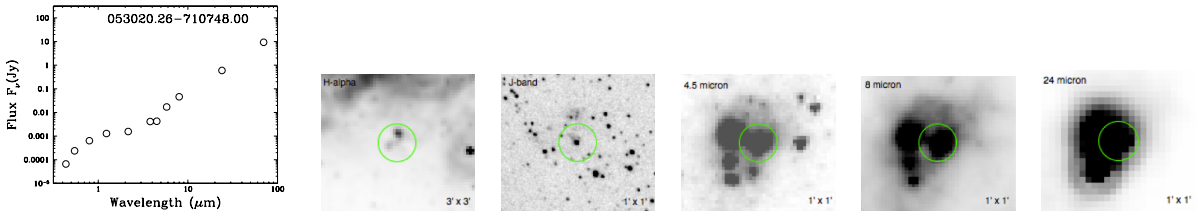

Figure 4.36 SEDs and sample multiwavelength images for the YSO candidate classified as a "probable" Type II/III YSO. The wavelength being displayed is at the upper left of each box, and the field of view is at the lower right. The green circles are centered on the source being examined and are not indicative of the flux aperture used in photometry.

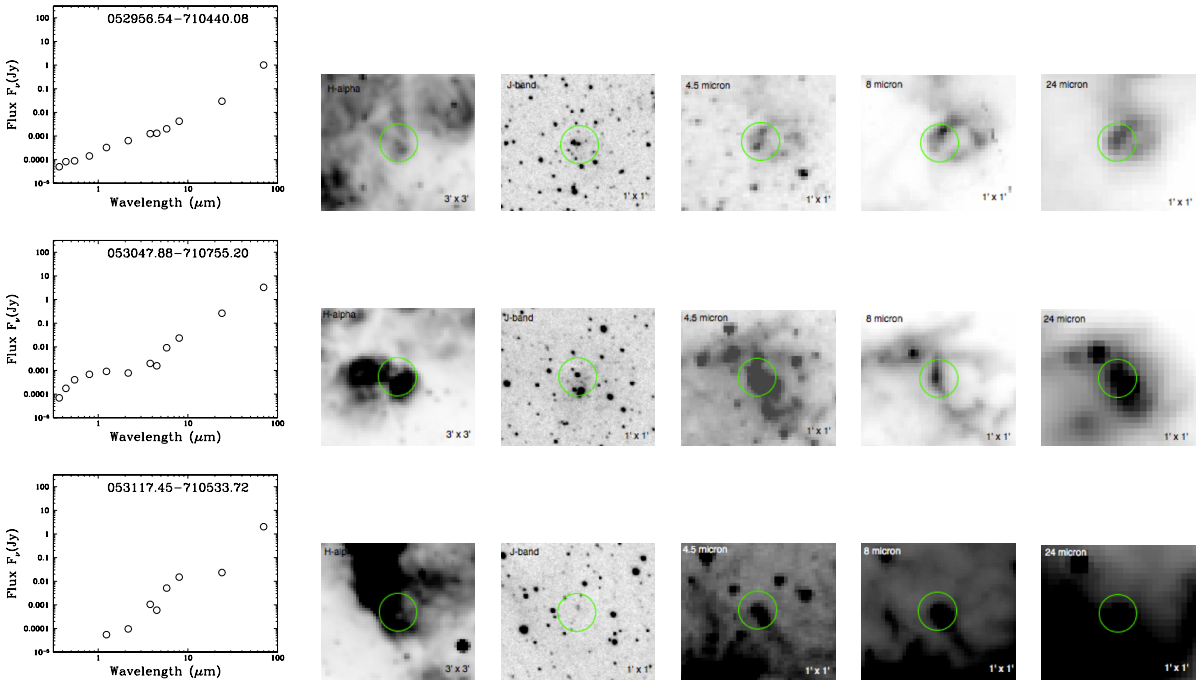

Figure 4.37 SEDs and sample multiwavelength images for the YSO candidates classified as "probable" multiple YSOs. The wavelength being displayed is at the upper left of each box, and the field of view is at the lower right. The green circles are centered on the source being examined and are not indicative of the flux aperture used in photometry.

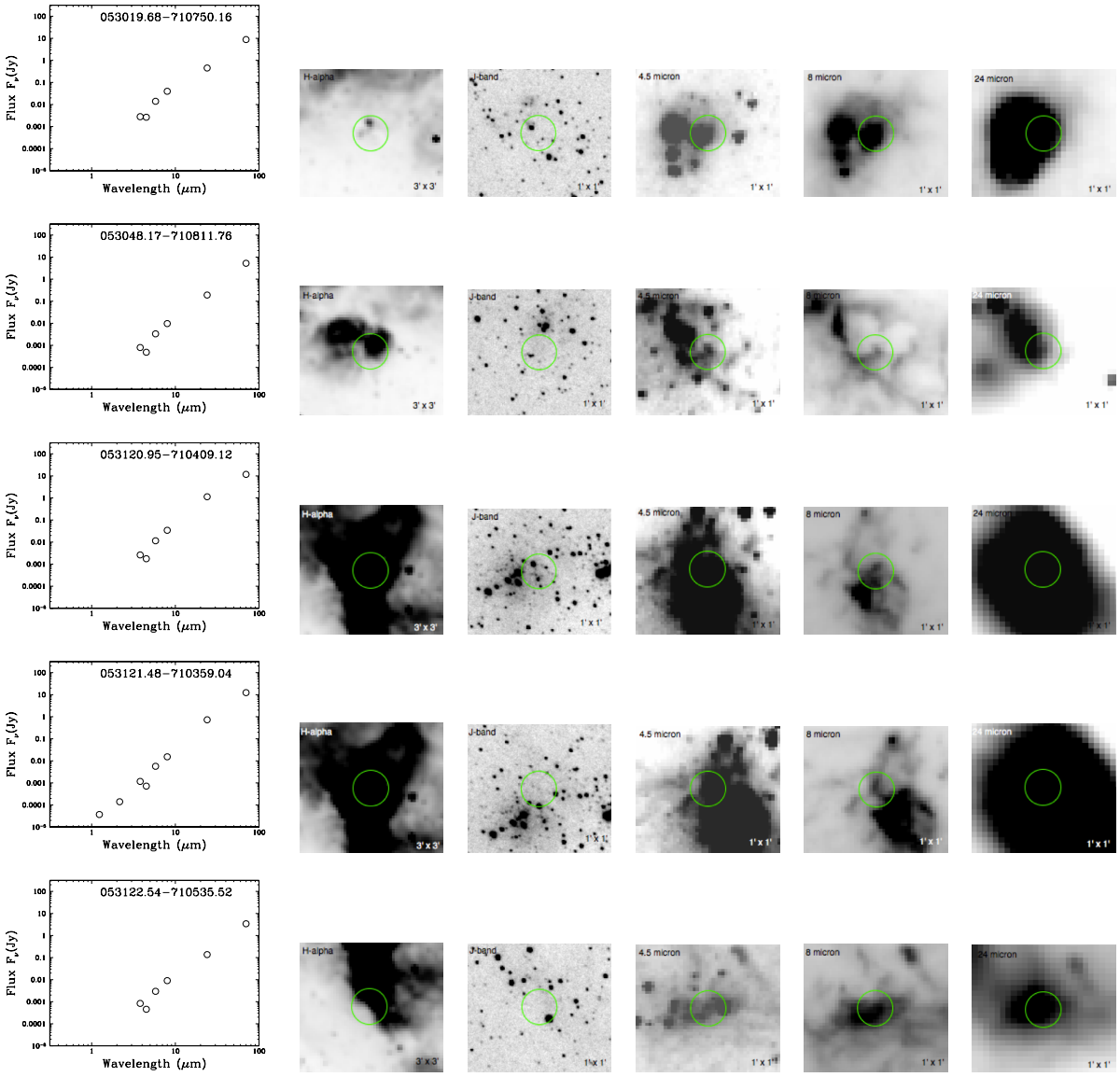

Figure 4.38 SEDs and sample multiwavelength images for the YSO candidates classified as a "possible" Type I YSOs. The wavelength being displayed is at the upper left of each box, and the field of view is at the lower right. The green circles are centered on the source being examined and are not indicative of the flux aperture used in photometry.

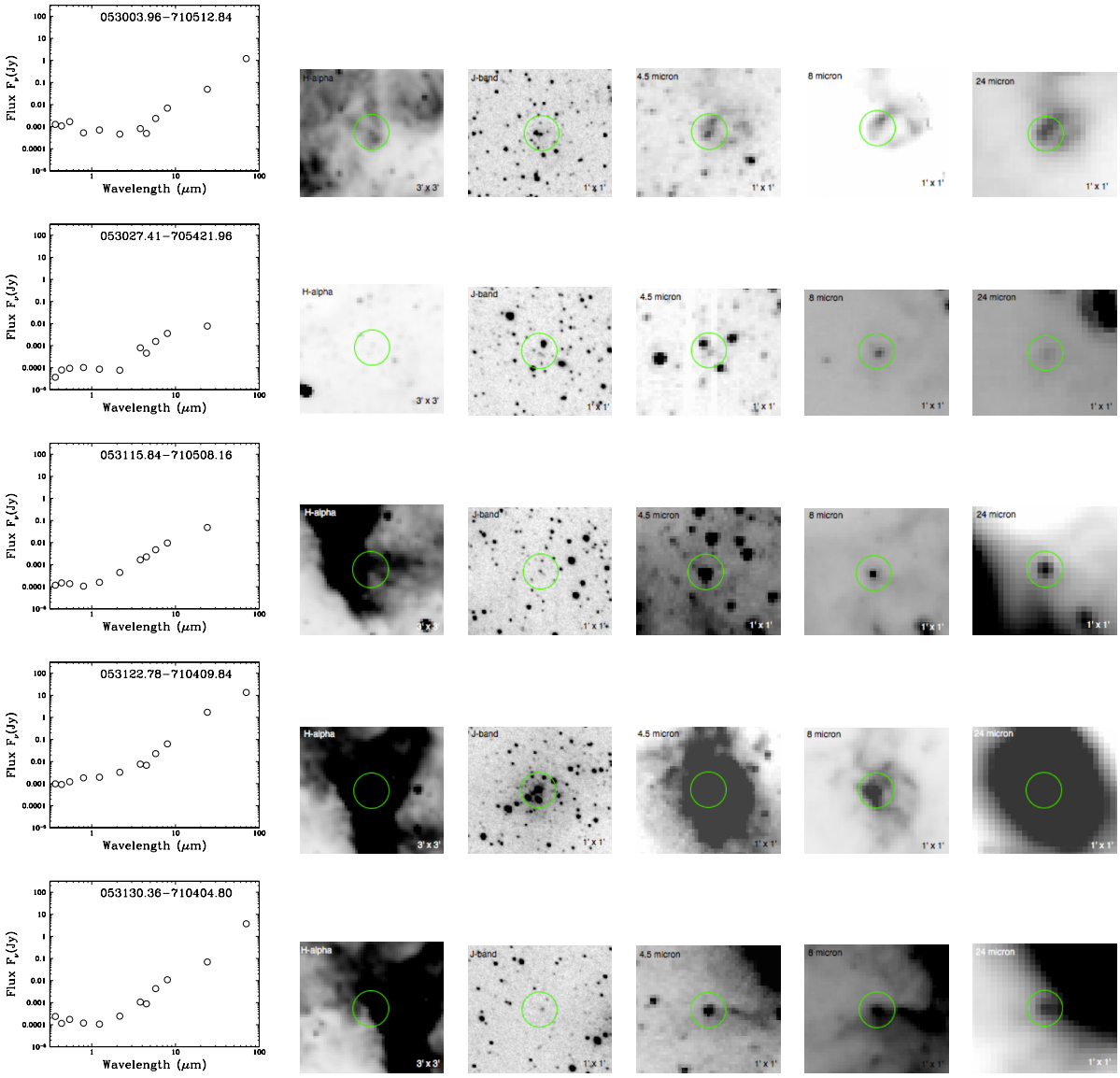

Figure 4.39 SEDs and sample multiwavelength images for the YSO candidates classified as "possible" Type II YSOs. The wavelength being displayed is at the upper left of each box, and the field of view is at the lower right. The green circles are centered on the source being examined and are not indicative of the flux aperture used in photometry.

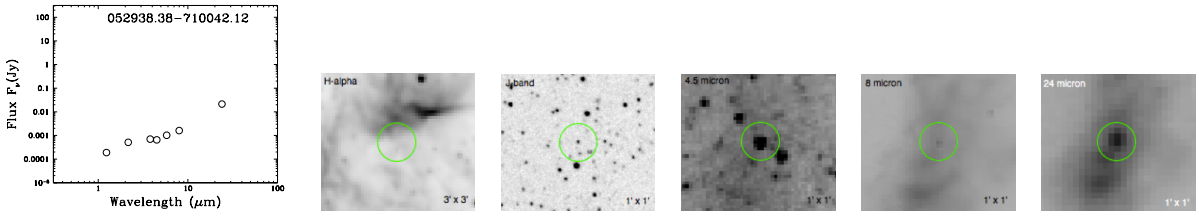

Figure 4.40 SEDs and sample multiwavelength images for the YSO candidate classified as a "possible" Type I/II YSO. The wavelength being displayed is at the upper left of each box, and the field of view is at the lower right. The green circles are centered on the source being examined and are not indicative of the flux aperture used in photometry.

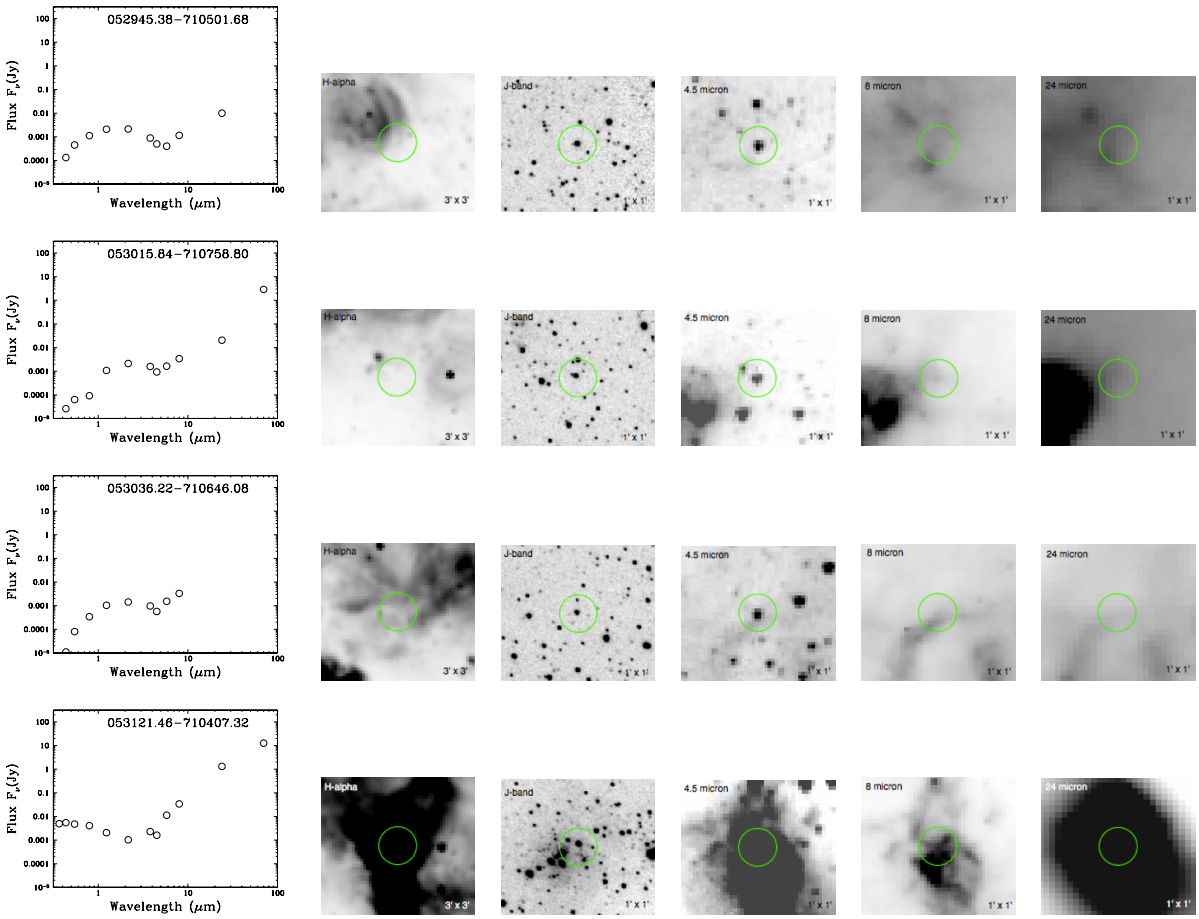

Figure 4.41 SEDs and sample multiwavelength images for the YSO candidates classified as "possible" Type III YSOs. The wavelength being displayed is at the upper left of each box, and the field of view is at the lower right. The green circles are centered on the source being examined and are not indicative of the flux aperture used in photometry.

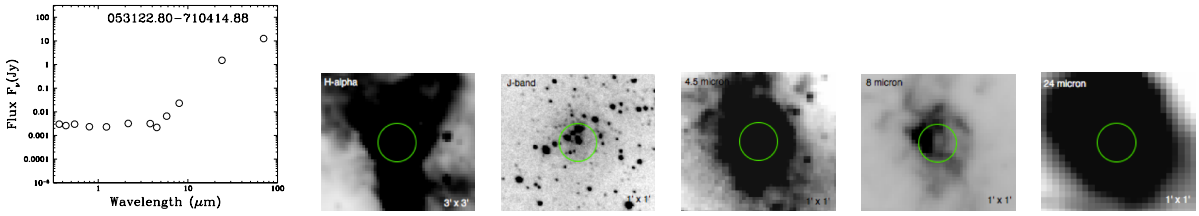

Figure 4.42 SEDs and sample multiwavelength images for the YSO candidate classified as a "possible" multiple YSOs. The wavelength being displayed is at the upper left of each box, and the field of view is at the lower right. The green circles are centered on the source being examined and are not indicative of the flux aperture used in photometry.

The SED fits are shown in Figures 4.43 through 4.50, organized by the evolutionary type I assigned the YSOs. In the plots for the fits, the flux data points are shown as filled circles. Upper limits for fluxes are shown as filled triangles. Error bars are shown for these data points, but they are usually smaller than the symbols on the plots. The solid black line on each plot shows the best-fit model (the model with the minimum χ^2 value). The radiation from the star reddened by the best-fit absorption is shown by the black dashed lines. The gray lines show "acceptable" models that represent a range of models that fit almost as well as the best-fit model for each YSO.

The SED fits for the 12 YSOs that I classified as Type I are shown in Figures 4.43 and 4.44. The best-fit model for each of these YSOs seems fairly well fit, though the upper limits sometimes input for the far-infrared flux values are often lower than the model would suggest. This is because when I input these upper limits, I also input a 95% confidence level for the upper limit value, instead of forcing the value to be the upper limit 100% of the time. As seen in Table 4.2, these Type I YSOs have relatively large ranges inferred for the central source masses. Also seen in the table, all 12 Type I YSOs were well-fit to a Stage I YSO model.

The SED fits for the 11 Type I/II YSOs are shown in Figures 4.45 and 4.46. These are generally well-fit to the best-fit model as well, though sometimes the upper limits on the far-infrared flux values look out of place. The inferred mass ranges for these are generally smaller than those of the Type I YSOs. All of the Type I/II YSOs were well-fitted to a Stage I or Stage II (sometimes both) YSO model.

The SEDs for the 11 Type II YSOs that were fitted to models are shown in Figures 4.47 and 4.48. These appear to generally be good matches to the models they were fit to. The inferred mass ranges for these Type II YSOs are generally smaller than for the previous YSO types, ranging from within one Solar mass to seven Solar masses. Nine out of the 11 Type II YSOs were well-fitted to a Stage II model YSO.

There were three Type II/III YSOs fitted to the model YSOs. The SEDs for these are shown in Figure 4.49. Visually, one of these looks particularly well-fitted to the best-fit model, and the other two look generally well-fitted. The mass range for two of these YSOs is one Solar mass, and the range for the third is six Solar masses. Two of them were well-fitted to Stage II model YSOs.

Six Type III YSOs were fit to the models, and their SEDs are shown in Figure 4.50. These have small mass ranges, from one to three Solar masses. Three of the six Type III YSOs were well-fitted to Stage III model YSOs.

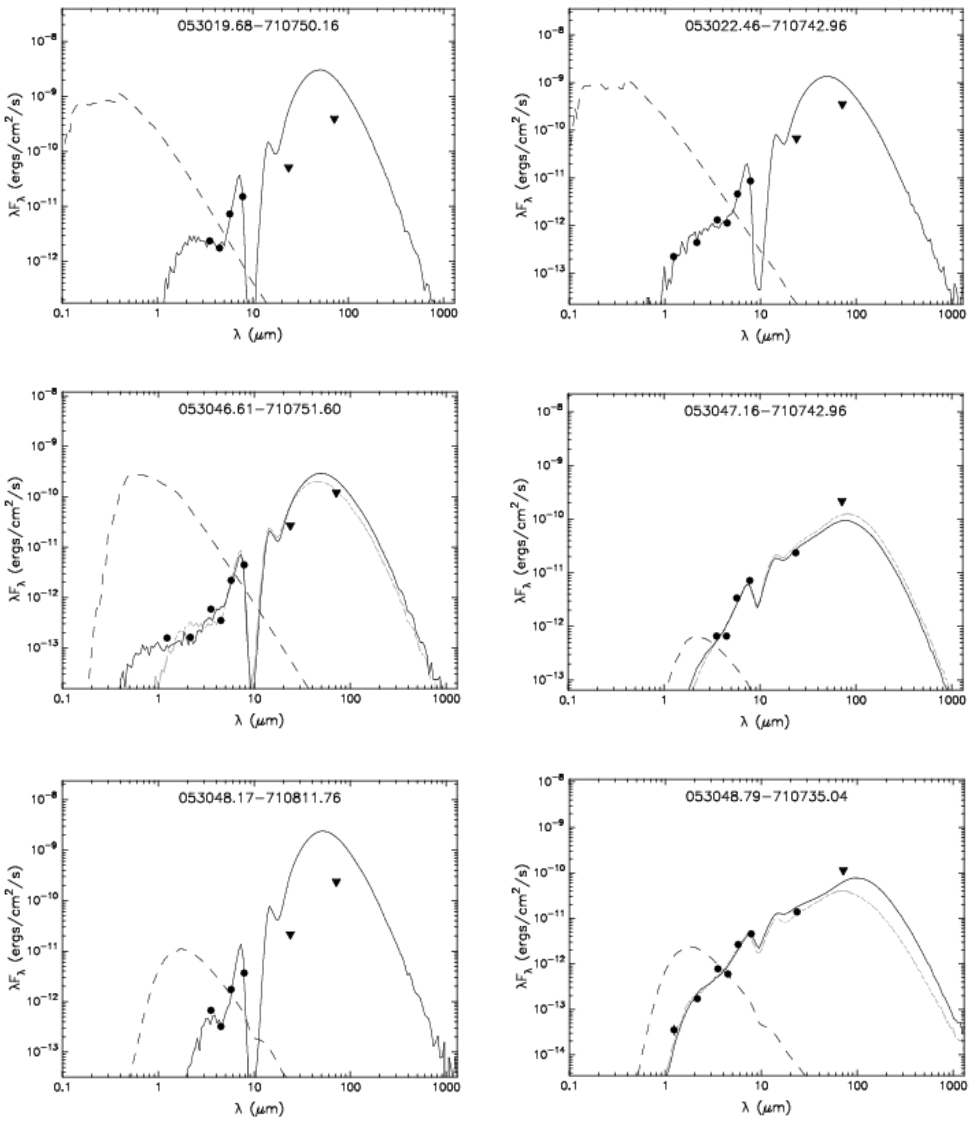

Figure 4.43 Model SED Fits of Type I YSOs. In each fit, flux data points are show as filled circles while upper limits are given as filled triangles. The solid black line shows the best-fit model, and the gray lines show a range of "acceptable" models. The radiation from the star reddened by the best-fit absorption is given by the black dashed line.

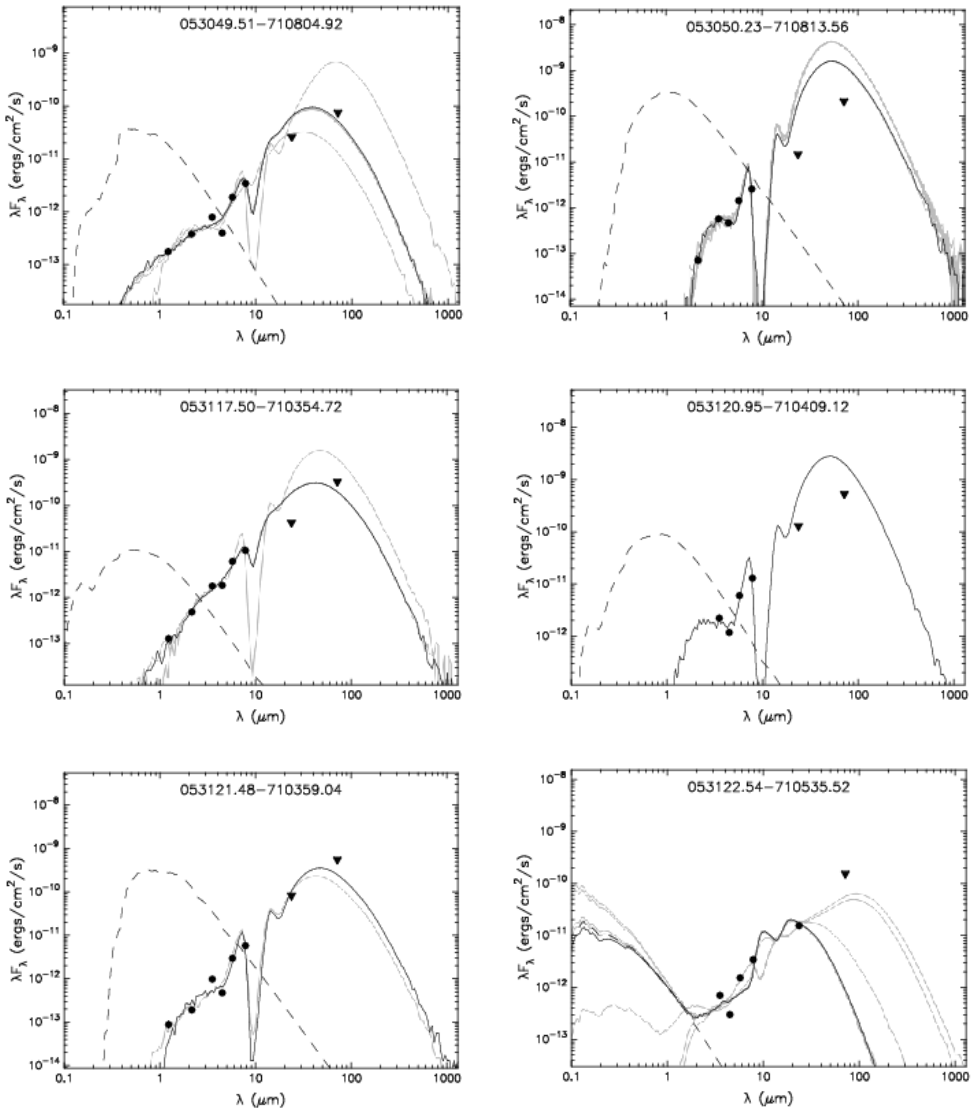

Figure 4.44 Model SED Fits of Type I YSOs. In each fit, flux data points are show as filled circles while upper limits are given as filled triangles. The solid black line shows the best-fit model, and the gray lines show a range of "acceptable" models. The radiation from the star reddened by the best-fit absorption is given by the black dashed line.

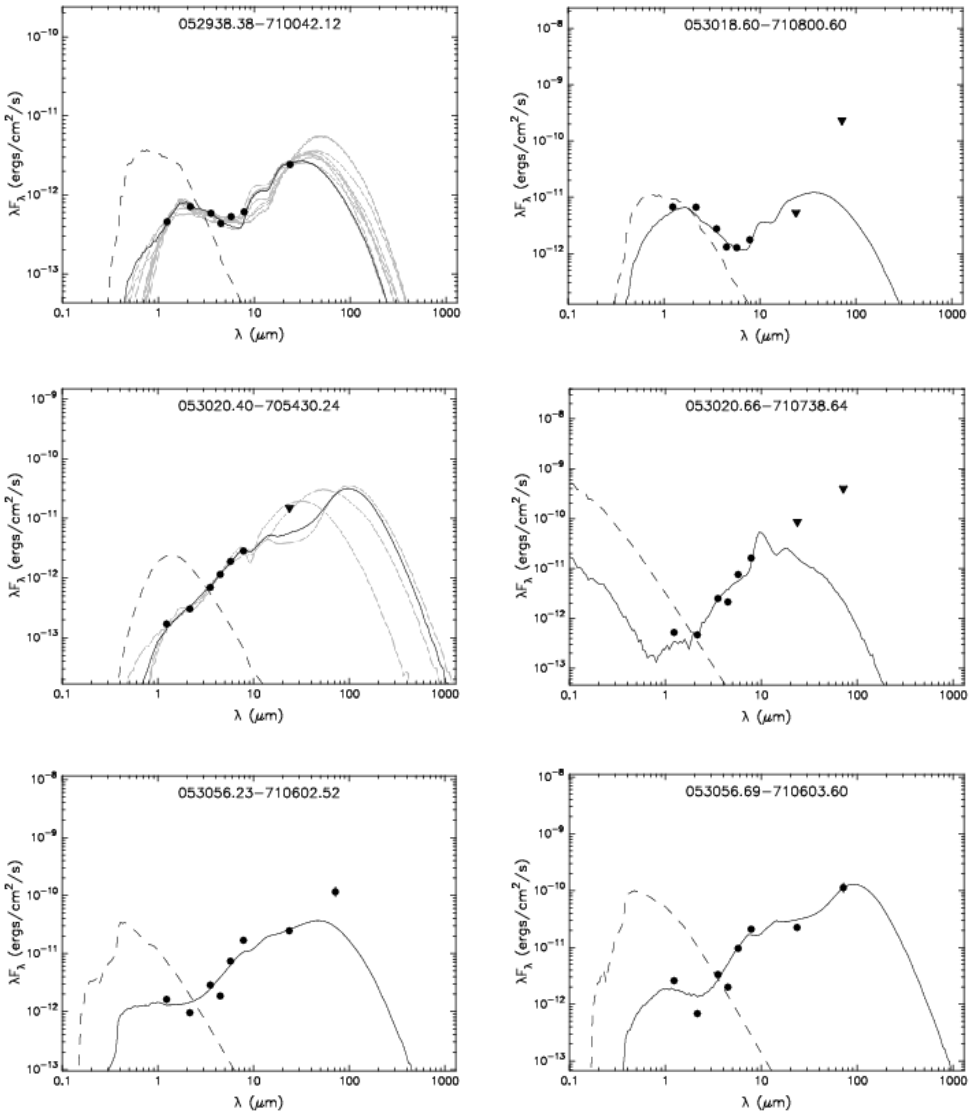

Figure 4.45 Model SED Fits of Type I/II YSOs. In each fit, flux data points are show as filled circles while upper limits are given as filled triangles. The solid black line shows the best-fit model, and the gray lines show a range of "acceptable" models. The radiation from the star reddened by the best-fit absorption is given by the black dashed line.

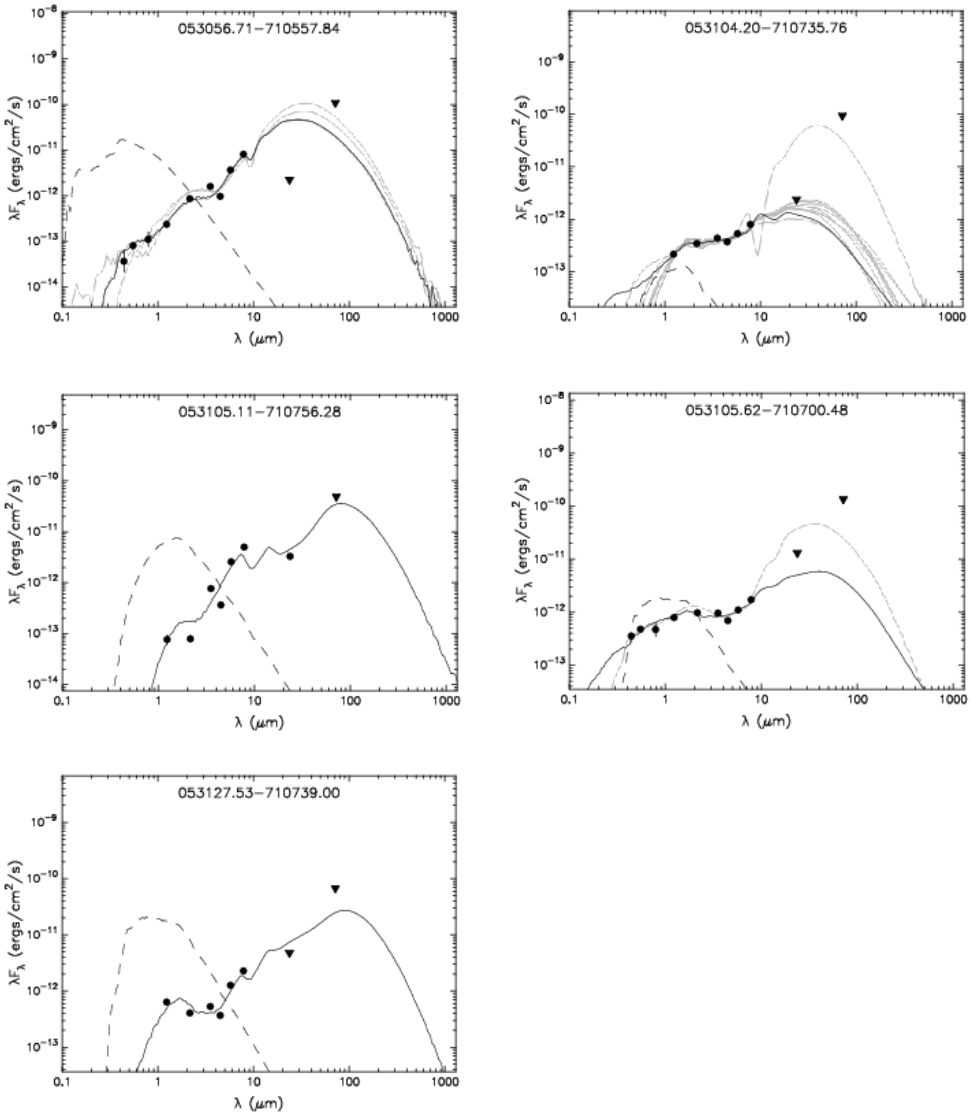

Figure 4.46 Model SED Fits of Type I/II YSOs. In each fit, flux data points are show as filled circles while upper limits are given as filled triangles. The solid black line shows the best-fit model, and the gray lines show a range of "acceptable" models. The radiation from the star reddened by the best-fit absorption is given by the black dashed line.

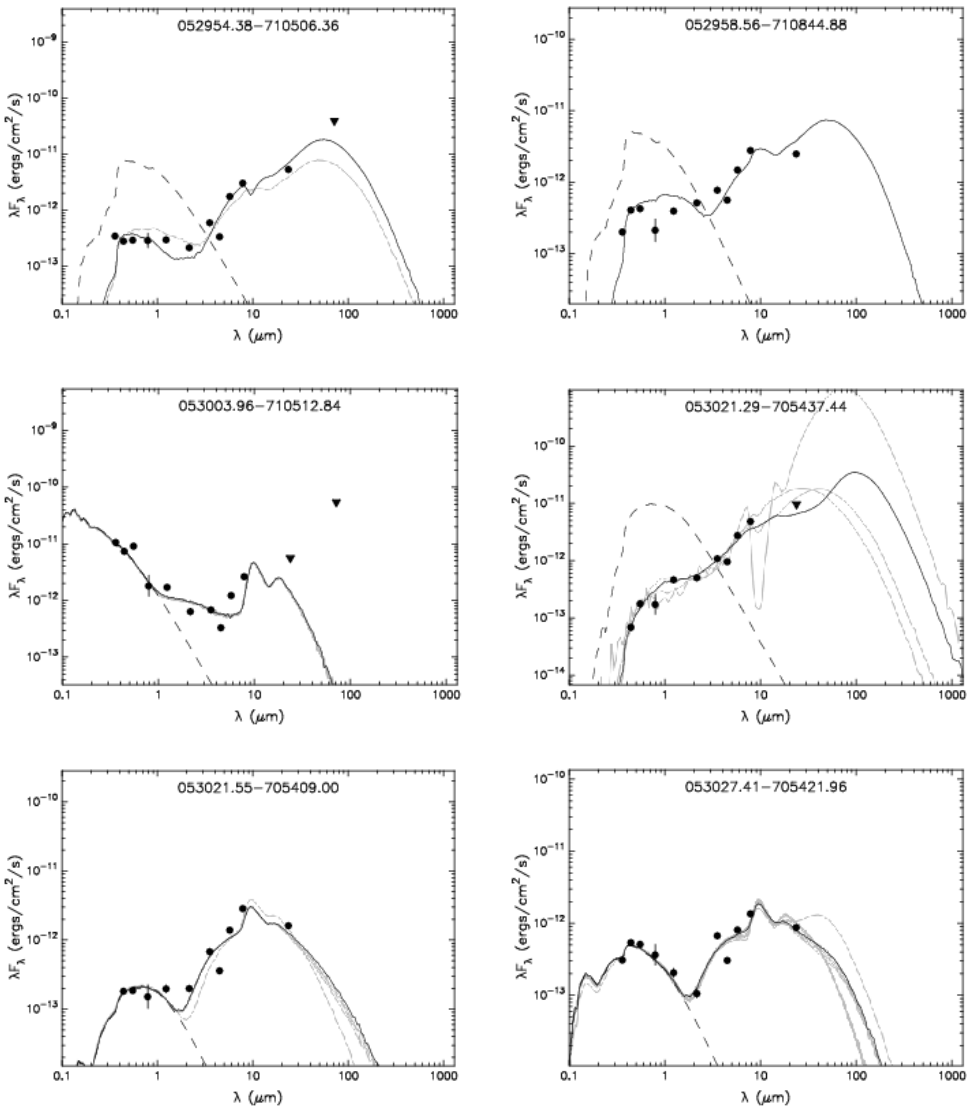

Figure 4.47 Model SED Fits of Type II YSOs. In each fit, flux data points are show as filled circles while upper limits are given as filled triangles. The solid black line shows the best-fit model, and the gray lines show a range of "acceptable" models. The radiation from the star reddened by the best-fit absorption is given by the black dashed line.

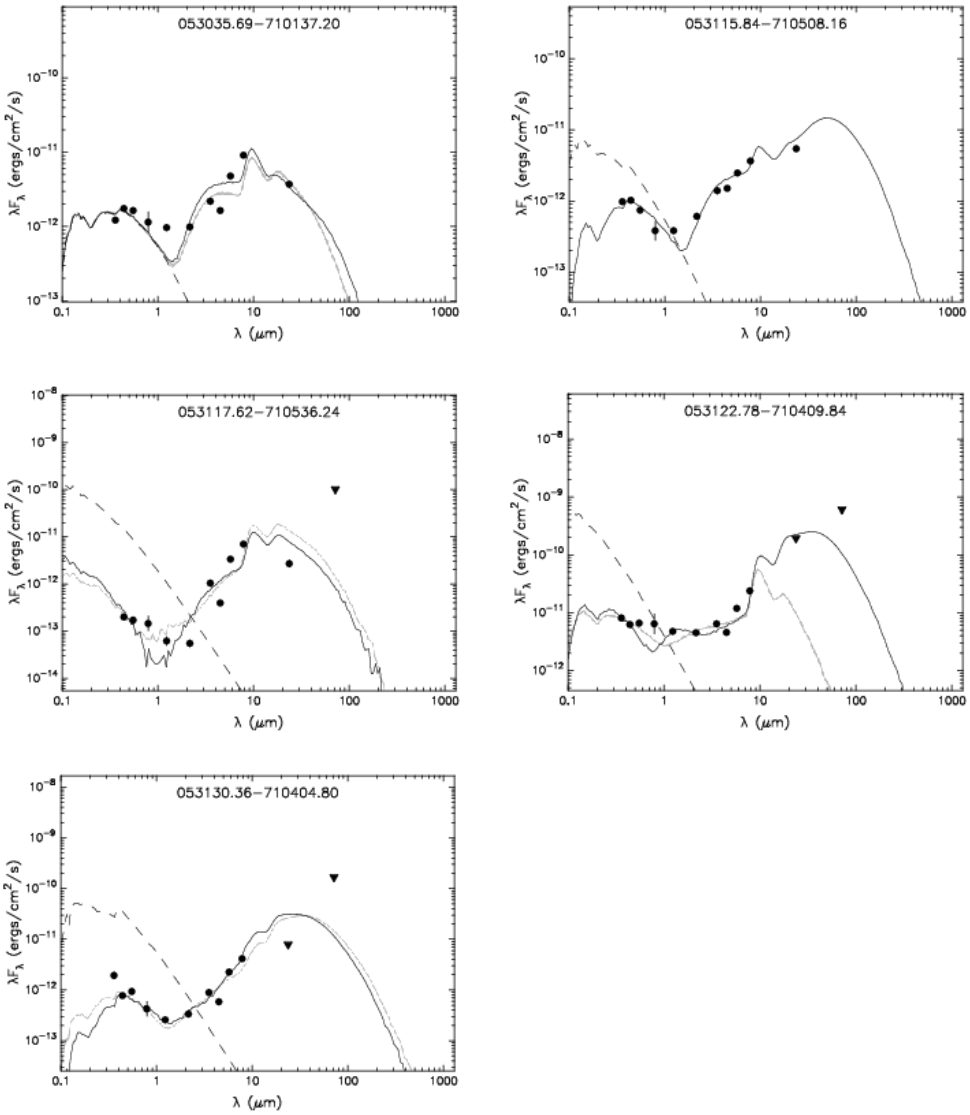

Figure 4.48 Model SED Fits of Type II YSOs. In each fit, flux data points are show as filled circles while upper limits are given as filled triangles. The solid black line shows the best-fit model, and the gray lines show a range of "acceptable" models. The radiation from the star reddened by the best-fit absorption is given by the black dashed line.

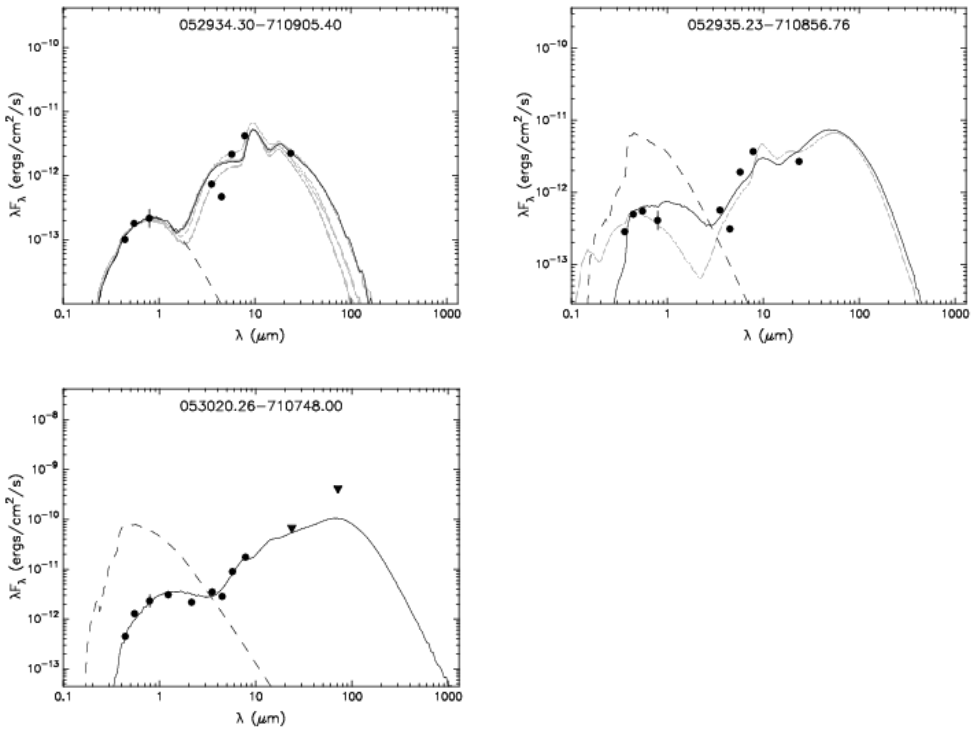

Figure 4.49 Model SED Fits of Type II/III YSOs. In each fit, flux data points are show as filled circles while upper limits are given as filled triangles. The solid black line shows the best-fit model, and the gray lines show a range of "acceptable" models. The radiation from the star reddened by the best-fit absorption is given by the black dashed line.

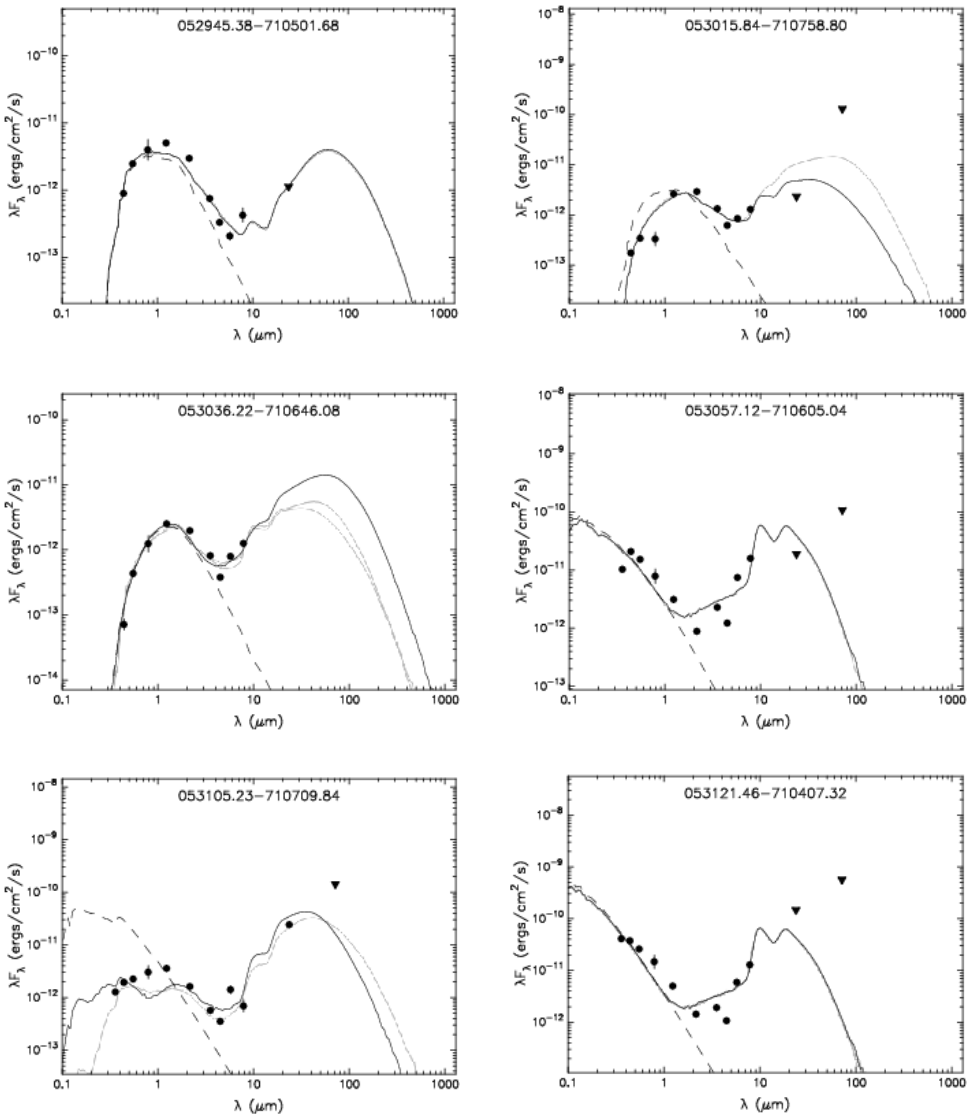

Figure 4.50 Model SED Fits of Type III YSOs. In each fit, flux data points are show as filled circles while upper limits are given as filled triangles. The solid black line shows the best-fit model, and the gray lines show a range of "acceptable" models. The radiation from the star reddened by the best-fit absorption is given by the black dashed line.

Chapter 5

Conclusions

5.1 Massive Star Formation in N206

This section investigates the spatial distribution of the YSOs in order to determine where and why star formation is occurring in the N206 region. The locations of YSOs with respect to components of the interstellar medium and to other populations of stars lend insight into these questions, as do the spatial distributions of the YSOs according to their masses and evolutionary stages.

5.1.1 Spatial Distribution of YSOs in N206

Figure 5.1 shows an Hα image of the H II complex N206, with the right half of the figure marking certain features in the complex. The Hα emission seen in the figure shows the location of H II, or ionized hydrogen, gas. The dominant Hα structure seen in N206 is a superbubble near the center of the image. This superbubble is likely to have been created by two mechanisms: shock waves moving outward from supernovae and strong stellar winds from massive O and B stars. The superbubble is 110 pc x 110 pc in size, and most of the Hα emission is coming from the eastern and southern sides of the bubble, where much of

the star formation is predicted to occur. The location of the superbubble is outlined on the right half of the figure. On the eastern side of N206 is a supernova remnant, SNR 532-710. A shell structure can be seen here, from the expanding shockwave of the supernova. This SNR is 30 pc x 30 pc and is outlined on the right half of the figure. N206 also contains two OB associations, LH 66 and LH 69, whose locations are given on the right half of the figure.

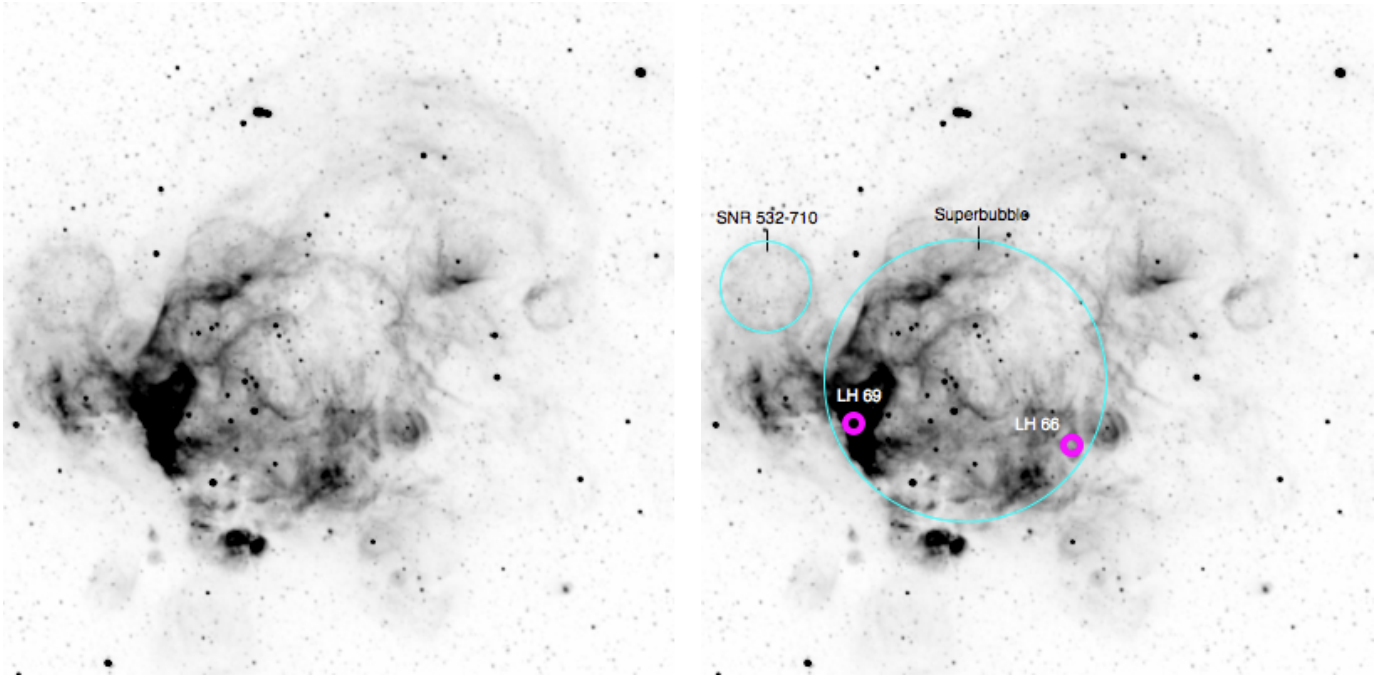

Figure 5.1 An Hα image of N206. The image is shown twice, with a superbubble, a supernova remnant (SNR), and two OB associations marked in the image on the right-hand-side.

Figure 5.2 shows the locations of the YSOs found in this study within N206, given as red circles. Contours showing the locations and densities of giant molecular clouds are also shown, in light blue.

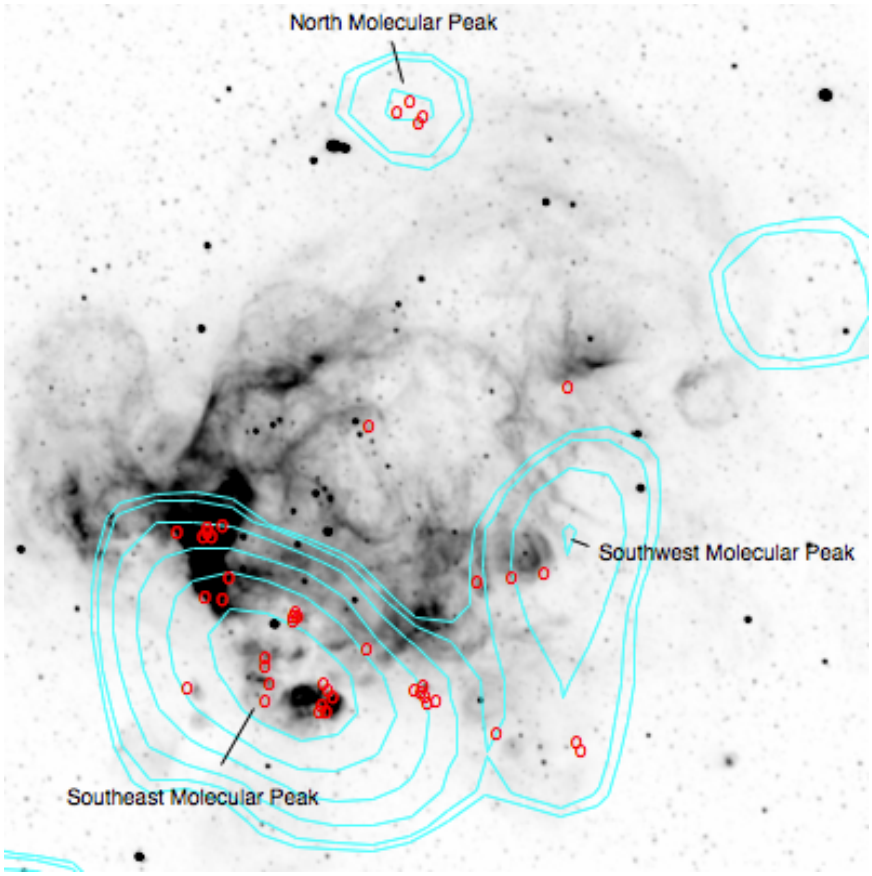

Figure 5.2 Spatial distribution of YSOs in N206. Molecular gas contours are shown in light blue, and locations of YSOs are shown by red circles.

As seen in Figure 5.2, about 70% of the YSOs are located along the eastern and southern edges of the superbubble, where much of the star formation is predicted to occur. About 90% of the YSOs are in or near Hα emission regions. Also seen in the figure, 41 of the 43 YSOs found are located in giant molecular clouds, and about 75% of the YSOs are grouped near the peaks of these clouds. The northern molecular cloud has four YSOs tightly distributed at the peak. There appears to be very little ionized hydrogen gas in this area. Near the peak of the southwestern molecular cloud there are three loosely distributed YSOs, two of which appear to be along the edge of an H II region and one of which lies on an Hα emission filament. There are several tight groups of YSOs distributed around the southeastern molecular cloud peak, some associated with Hα emission regions and some not.

The southwestern molecular peak corresponds to GMC LMC/M5303-7104, catalogued by Mizuno et al. (2001) [52]. The southeastern molecular peak corresponds to GMC LMC/M5316-7110. The northern peak does not correspond to a Mizuno et al. GMC. Mizuno et al. (2001) reported a FWHM line-width value (ΔV) for the catalogued molecular peaks that measures a velocity dispersion of molecular species in the clouds. This ΔV value represents the level of stellar energy feedback in the molecular clouds in the last few million years. The ΔV value measured at the southwestern molecular peak is 4.1 km/s, and the value at the southeastern peak is 6.9 km/s. This suggests that the southeastern peak has experienced more stellar energy feedback, from massive stellar winds and supernovae. Figure 5.2 shows that there are more YSOs around the peak with the highest ΔV value, suggesting further that the higher amount of stellar feedback is correlated with a higher amount of star formation.

The placement of so many YSOs along the southern and eastern edges of the superbubble suggests that star formation is being triggered in the GMC by the expanding bubble. There are also three YSOs on the western edge of the bubble, near the southwest molecular peak. This expansion may also have triggered the formation of the massive stars in the OB

associations near the rim of the bubble. Winds from these OB associations then may have contributed to further expansion of the bubble, triggering further star formation.

5.1.2 Mass Distribution of YSOs in N206

Figure 5.3 shows how the YSOs in N206 may be distributed by mass. The mass used is the estimated mass of the central source ($M_\star$) of the best-fit model for each YSO, so these values should be interpreted with caution. In this figure, the YSOs with $M_\star \geq 17$ $M_\odot$, which will become O-type stars, are shown by purple circles. The green circles show YSOs with 17 $M_\odot$ $> M_\star \geq 8$ $M_\odot$, representing B-type stars. A- and later-type (intermediate mass) stars, with $M_\star < 8$ $M_\odot$ are shown by red circles.

As seen in Figure 5.3, all of the most massive, O-type, YSOs are near the southeastern molecular cloud peak, with 75% of them in bright H II regions. Most of the B-type YSOs are also in this area. The southwestern molecular cloud peak has two B-type and one intermediate-type YSO near it. The northern molecular cloud peak has two B-type and two intermediate-type YSOs tightly grouped.

Elmegreen & Lada (1977) [53] say that strong winds from OB associations cause ionization and shock fronts that compress molecular clouds, making them unstable and triggering star formation. It is interesting that the O- and B-type YSOs appear to be correlated in location with a previous generation of O and B stars (the two OB associations, LH 66 and LH69). Of course, since this search is biased toward more massive YSOs, it may be that there would be more intermediate- and low-mass YSOs in that area also and that the star formation triggering is just generally high in that molecular cloud.

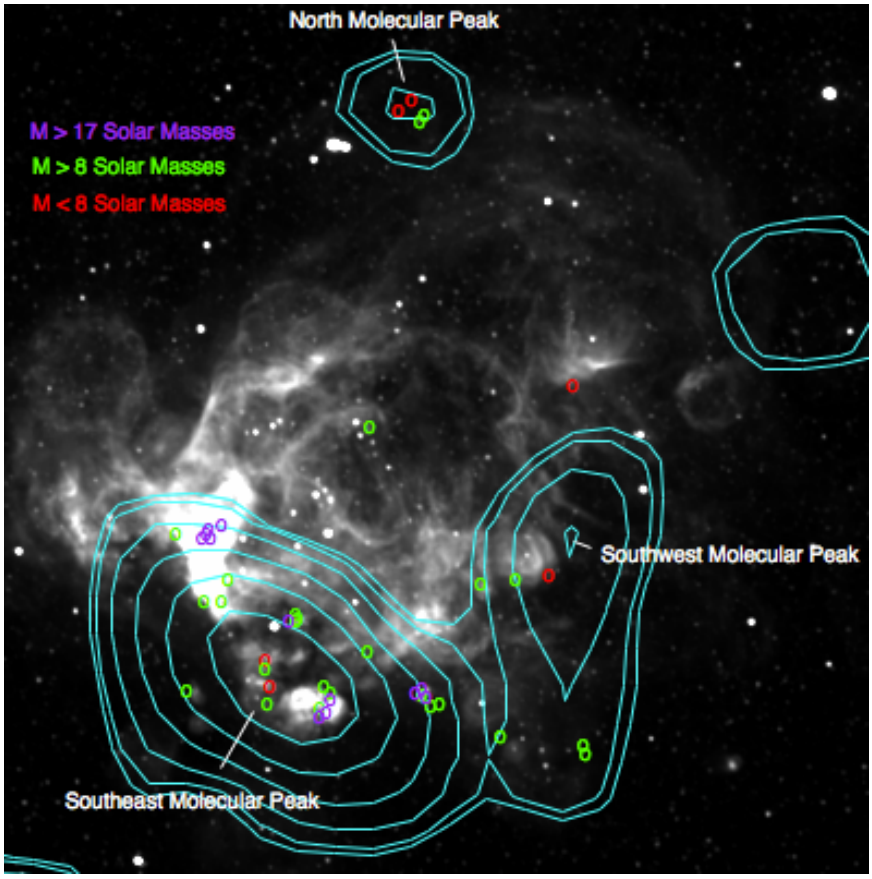

Figure 5.3 YSOs of different masses are shown in their locations in N206.

5.1.3 Age Distribution of YSOs in N206

Figure 5.4 shows how the different YSOs are distributed spatially according to the evolutionary types I assigned them. In the figure, the red circles mark the locations of the Type I youngest YSOs, orange circles are Type I/II, green circles are Type II, blue circles are Type II/III, and purple circles mark the Type III oldest YSOs. The evolutionary types used here are the ones assigned by me according to the shapes of the SEDs, not the evolutionary stages suggested by the models (though, in many cases, they are the same).

Past authors have looked at this distribution as an age distribution. If this could be treated as an age distribution and if the expansion of the superbubble is responsible for triggering the formation of these YSOs in N206, we would expect to see the younger (Type

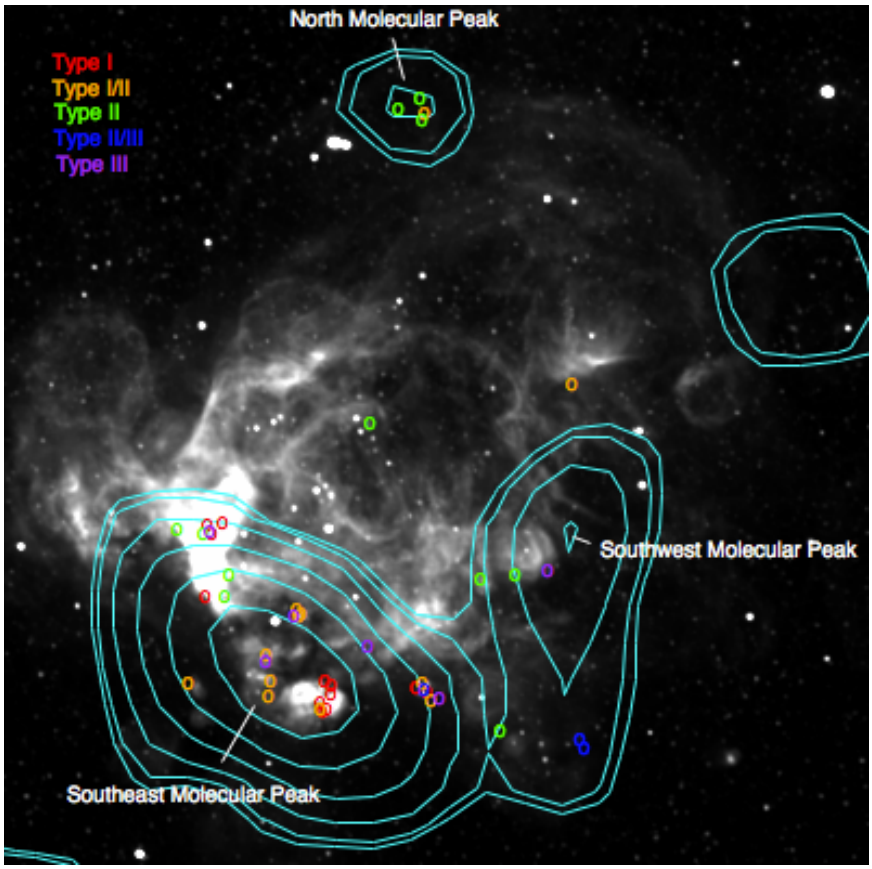

Figure 5.4 YSOs of different evolutionary types shown in their locations in N206.

I) YSOs closer to the outside of the rim of the bubble and the older (Type III) YSOs more toward the inside of the bubble. There are a few problems with this assessment, however. One problem is that higher-mass YSOs evolve faster than lower-mass YSOs and therefore go through the different evolutionary types faster. So a Type III YSO is not necessarily older than a Type I YSO. Mass needs to be considered. A second problem is a projection effect; in the image we are looking at a three-dimensional space in two dimensions. It is difficult to tell if YSOs that appear to be near the center of the superbubble are actually at the center or are at the edge of the bubble closer to us.

To account for mass, I looked at the distribution of evolutionary types separated by mass. These distributions are shown in Figures 5.5- 5.7. Perhaps with a larger sample size it would

be possible to see a pattern in the ages of the YSOs, but with so few YSOs it is difficult to distinguish such a pattern.

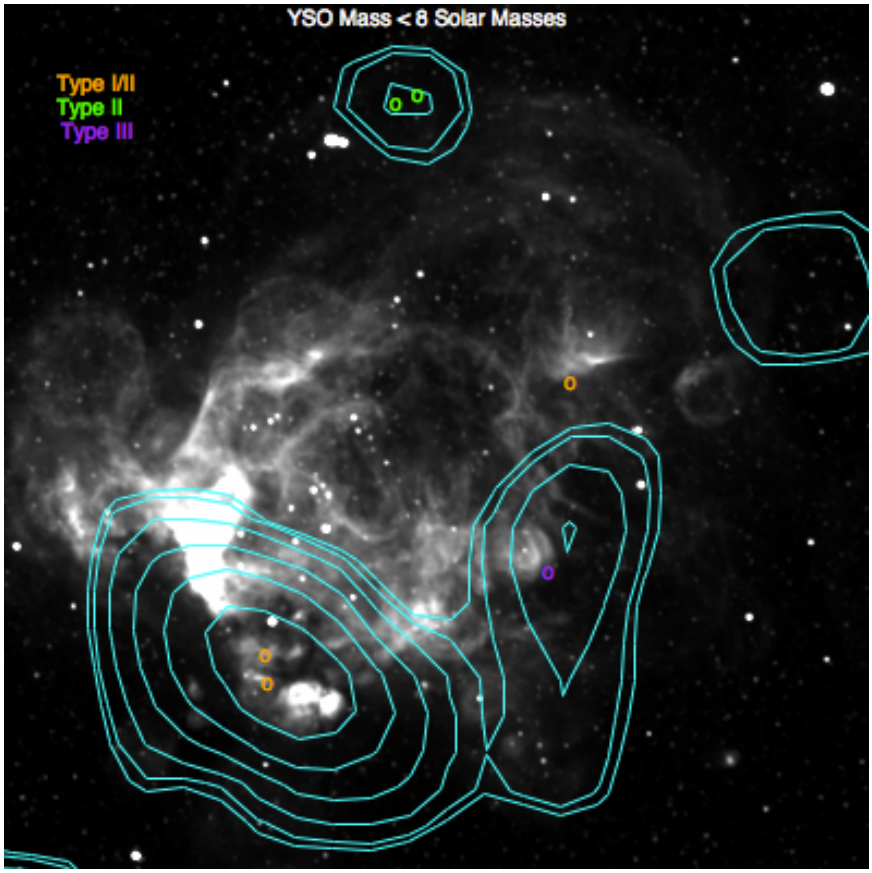

Figure 5.5 YSOs with masses less than 8 solar masses of different evolutionary types shown in their locations in N206.

It is interesting to note that most of the highest-mass YSOs are of early evolutionary types. Behrend & Maeder (2001) [54] have found that most of the growth for massive YSOs occurs during the last 10% of their pre-main sequence stage. The mass distribution of the massive YSOs in this study is consistent with these findings.

It is also interesting that no YSOs were found around the rim of the supernova remnant. Gorjian et al. (2004) [55] do predict that the SNR would contribute to the current star formation as might be expected by an expanding SNR shock wave. Romita et al. (2010) [26],

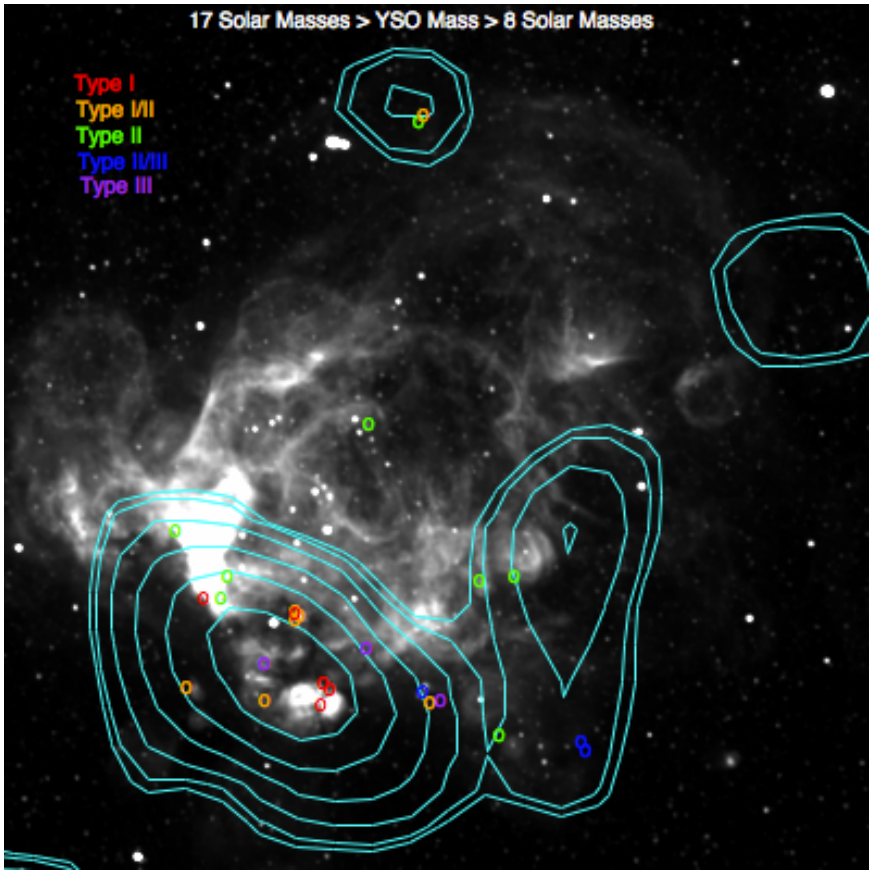

Figure 5.6 YSOs with masses between 8 and 17 solar masses of different evolutionary types shown in their locations in N206.

however, highlight some interesting things that have more recently been learned about this SNR. Desai et al. (2010) [56] studied the SNRs in the LMC, and based on the YSOs found in the LMC by Gruendl and Chu (2009) [1], they found no evidence that the SNR was triggering star formation in the region. Also, in their study of this SNR, Williams et al. (2005) [57] estimate an upper limit of 40,000 years for the age of the SNR, making the expansion velocity of the shock wave too high to compress the molecular gas [56]. If the expansion of a shock wave is high enough, it can disperse rather than compress molecular gas, making star formation impossible.

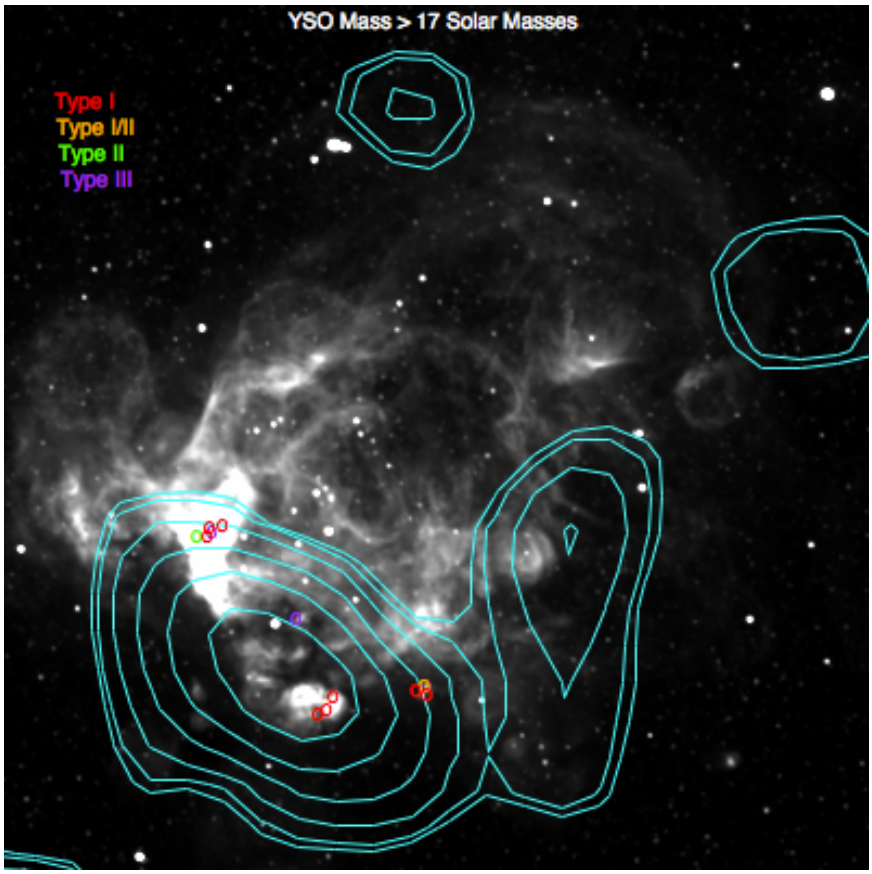

Figure 5.7 YSOs with masses greater than 17 solar masses of different evolutionary types shown in their locations in N206.

5.2 Previously Identified YSOs in N206

In this section, I compare the YSOs I identified and characterized in N206 with previous surveys that identified YSOs in the region. I conclude that my survey is an improvement over the past surveys and is a significant contribution to our knowledge of star formation in the LMC.

5.2.1 YSOs Identified by Whitney et al. (2008)

Whitney et al. (2008) [33] (hereafter called W08) surveyed the entire LMC for YSOs and found about 1000 YSO candidates. Seven of these candidates are in the N206 complex and

Table 5.1. N206 YSOs Identified by Whitney et al. (2008)

Whitney ID	Buehler ID	Whitney Class.	Buehler Class.
768	052935.23-710856.76	YSO	C II/III
769	052938.38-710042.12	YSO	GC I/II
780	053020.40-705430.24	YSOhp I	C I/II
781	053021.29-705437.44	YSOhp	C II
784	053035.69-710137.20	YSOhp	C II
797	053115.84-710508.16	YSOhp I	GC II
802	053130.62-705749.32	YSOhp	G

are listed in Table 5.1. The table lists each candidate by the ID assigned by W08. Also in the table are the name (ID) I assigned each candidate, the classification given by W08, and the classification given by myself. Five of these candidates, given a classification of "YSOhp", were determined by W08 to be "high probability" YSO candidates, more likely to be YSOs than the ones designated "YSO". I determined six of the seven W08 candidates to be YSO candidates. I classified four of these as "C", meaning "definite" candidate. Of these four, I determined one to be a Type I/II, two to be Type II, and one to by Type II/III. Two of the candidates I determined to be "GC", meaning "possible" YSO, "probable" galaxy. One of these was designated "high probability" YSO by W08. The last W08 candidate (802), I determined to be a galaxy. In fact, this is one of the candidates that corresponded with a previously identified galaxy, 2MASS J05315772-7100494. W08 had determined this source to be a "high probability" YSO candidate. They do report having looked up all of their sources in the SIMBAD database and finding 80 of their sources to be galaxies or evolved stars. They do not, however, report this source as being a probable background galaxy.

For their YSO search, W08 used the SAGE Point Source Catalog of the LMC to provide their point sources. Just as in my search, their selection criteria for YSO candidates utilized

the *Spitzer* observations at [4.5 μm] and [8.0 μm]. They additionally used the other *Spitzer* wavelengths of [3.6 μm], [5.8 μm], and [24 μm], as well as a *Ks*-band measurement to select their YSOs. Using these wavelengths, their selection criteria for YSOs are as follows:

$$[3.6] < 6.76 + 1.10 \times ([3.6] - [24]) \text{ and } [3.6] > 13.86 - 0.91 \times ([3.6] - [24])$$

$$\text{or } [4.5] < 7.26 + 1.02 \times ([4.5] - [24]) \text{ and } [4.5] > 10.79 - 0.53 \times ([4.5] - [24])$$

$$\text{or } [3.6] < 10.6 + 3.50 \times ([3.6] - [4.5]) \text{ and } [3.6] > 13.35 - 2.41 \times ([3.6] - [4.5])$$

$$\text{or } [3.6] - [4.5] > 1.5$$

$$\text{or } [3.6] - [8.0] > 3.5 \text{ and } [3.6] < 13.5$$

$$\text{or } [3.6] - [8.0] > 4.5 \text{ and } [3.6] \geq 13.5$$

$$\text{or } [3.6] - [8.0] > 1.5 \text{ and } [3.6] - [8.0] \leq 3.5$$

$$\text{and } [3.6] < 13.5$$

$$\text{or } [5.8] < 7.83 + 0.89 \times ([5.8] - [24]) \text{ and } [5.8] > 10.79 - 0.81 \times ([5.8] - [24])$$

$$\text{or } [8.0] < 7.59 + 1.06 \times ([8.0] - [24]) \text{ and } [8.0] > 11.0 - 1.33 \times ([8.0] - [24])$$

$$\text{or } 24 < 3.72 + 0.95 \times ([8.0] - [24]) \text{ and } [24] > 9.76 - 1.79 \times ([8.0] - [24])$$

$$\text{or } [4.5] > 11.91 - 2.54 \times ([4.5] - [5.8]) \text{ and } [4.5] < 9.44 + 3.57 \times ([4.5] - [5.8])$$

$$\text{or } [8.0] < 12.52 - 0.73 \times ([4.5] - [8.0]) \text{ and } [8.0] > 28.30 - 18.29 \times ([4.5] - [8.0])$$

$$\text{and } [8.0] > 10.58 - 1.49 \times ([4.5] - [8.0])$$

$$\text{or } [4.5] - [8.0] > 3.7$$

$$\text{or } [4.5] - [8.0] > 2.7 \text{ and } [8.0] < 8.0$$

$$\text{or } [4.5] < 11.12 + 0.94 \times ([4.5] - [8.0]) \text{ and } [4.5 > 24.0 - 13.0 \times ([4.5] - [8.0])$$

$$\text{and } [4.5] > 11.13 - 0.89 \times ([4.5] - [8.0])$$

$$\text{or } [5.8] < 10.92 + 0.89 \times ([5.8] - [8.0]) \text{ and } [5.8] > 16.66 - 6.60 \times ([5.8] - [8.0])$$

$$\text{or } K > 12.5 \text{ and } K < 14.0$$

$$\text{and } K - [4.5] > 1.5 \text{ and } K - [4.5] < 3.5$$

$$\text{or } K > 12.5 \text{ and } K < 13.5$$

$$\text{and } K - [3.6] > 1.0 \text{ and } K - [3.6] < 2.5$$

This is a much longer list of criteria than I used to select my initial YSO candidates, utilizing several more color-magnitude diagrams. They used such an extensive list of color-selection criteria because they did not assess individual sources based on their morphologies. They needed a way to confidently rule out as many non-YSOs as possible over the entire LMC. Two diagrams from W08 are shown in Figure 5.8. In these color-magnitude diagrams, known populations are shown, with YSO candidates being selected to the right of the solid purple lines and above the dashed purple line.

Figure 5.9 shows the [8.0] vs. ([4.5] - [8.0]) color-magnitude diagram that I used in my initial YSO candidate selection. The green dashed line shows the galaxy cut I used, above which YSO candidates were selected. The magenta dashed lines show the color-selection criteria used in this color-magnitude space by W08. According to this criteria, sources to the right of this line would be considered as YSO candidates. The green filled circles show my final YSO candidates' locations. If this criteria had been applied to the point sources in

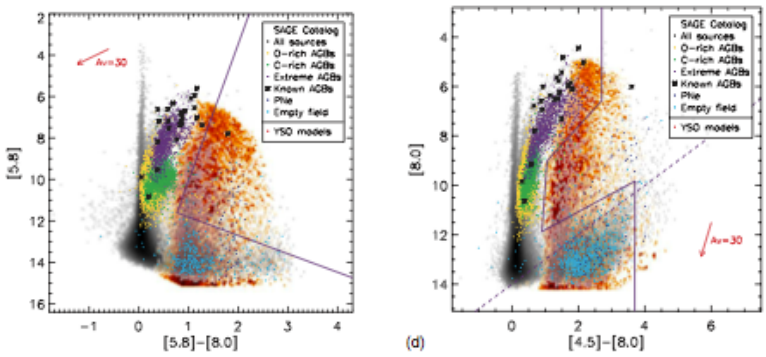

Figure 5.8 Two Color-Magnitude Diagrams used by Whitney et al. (2008) to Select YSO Candidates.

this study, six of my YSO candidates would not have even been considered. That explains why these were not identified by W08.

A possible explanation for Whitney et al. (2008) not identifying the remaining 40 YSOs in my catalog that fit their color-selection criteria is that initial point sources were located in different ways in the two studies. W08 used the point sources in the SAGE catalog of the LMC. This catalog used strict parameters for defining point sources, excluding any that looked slightly extended, which excludes any irregular point sources. Also, W08 applied a high signal-to-noise threshold that would have excluded sources near other bright sources and sources superposed on bright backgrounds, such as diffuse dust. Chen et al. (2009) [2] also found that they were able to identify 60 YSOs in N44, while W08 only identified 13, because of the same point source identification parameters, so this result is not surprising.

The technique used by W08 to identify YSOs in the LMC seems like a good first-run for locating these objects while looking across the entire galaxy, but their candidate selection criteria may have been too complex, and my search for YSOs in N206 seems more complete and significantly increases the number of YSO candidates identified in the region.

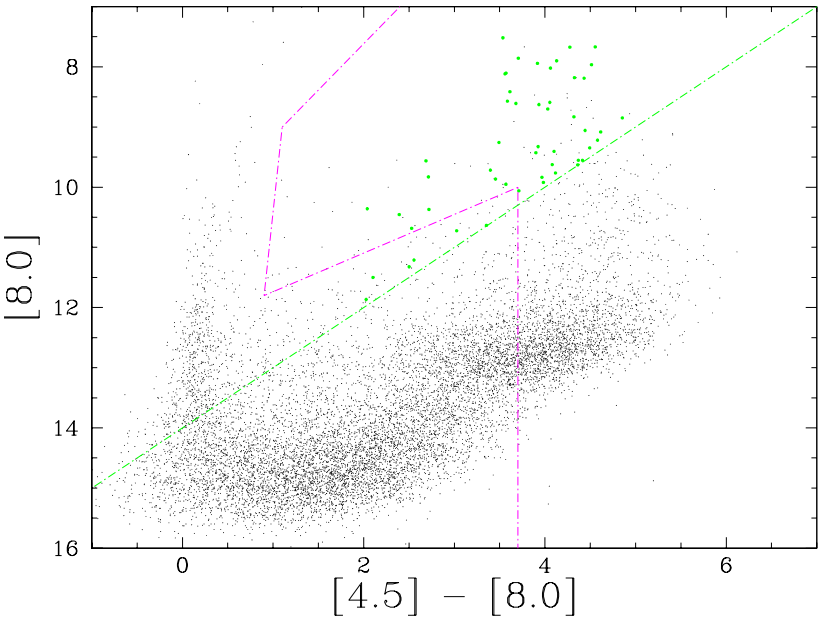

Figure 5.9 Color-Selection Criteria of Whitney et al. (2008) Applied to IRAC [4.5 μm] and [8.0 μm] Point Sources Found in This Study.

5.2.2 YSOs Identified by Gruendl & Chu (2009)

Gruendl & Chu (2009) [1] (hereafter called GC09) also surveyed the entire LMC, searching for YSOs. They report finding 1172 YSO candidates, 27 of which are in the N206 region. These sources are given in Table 5.2. The table lists the candidates by the name assigned by GC09. Also in the table are the name (ID) I assigned each candidate, the classification given by GC09, and the classification given by myself.

Table 5.2. N206 YSOs Identified by Gruendl & Chu (2009)

GC09 ID	Buehler ID	GC09 Class.	Buehler Class.
052934.42-710905.3	052934.30-710905.40	C	C II/III
052935.27-710856.7	052935.23-710856.76	C	C II/III
052938.44-710042.3	052938.38-710042.12	CD	GC I/II
052938.47-705520.9	052938.47-705520.64	CG	G
052954.46-710506.4	052954.38-710506.36	C	C II
052956.56-710440.0	052956.54-710440.08	C	CSD mult. II
052958.60-710844.8	052958.56-710844.88	C	C II
053020.33-710748.9	053020.26-710748.00	C	CS II/III
053020.41-705430.1	053020.40-705430.24	C	C I/II
053020.79-710738.6	053020.66-710738.64	C	C I/II
053021.30-705437.4	053021.29-705437.44	C	C II
053021.59-705408.7	053021.55-705409.00	C	C II
053022.50-710743.0	053022.46-710742.96	C	C I
053023.18-710556.3	053023.11-710556.40	C	C mult. II
053023.48-710747.2	– –	C	– –
053035.72-710137.1	053035.69-710137.20	C	C II
053046.79-710844.5	053046.75-710844.88	C	C mult. I/II
053047.27-710743.1	053047.16-710742.96	C	C I
053048.70-710735.2	053048.79-710735.04	CD	C I
053104.24-710736.0	053104.20-710735.76	CG	CSD I/II
053105.08-710756.3	053105.11-710756.28	C	CD I/II
053105.65-710700.5	053105.62-710700.48	C	C I/II
053115.89-710508.2	053115.84-710508.16	CG	GC II
053117.52-710354.7	053117.50-710354.72	C	C I
053122.85-710409.9	053122.78-710409.84	C	GC II
053123.76-710735.1	053123.57-710735.40	C	C mult. I
053130.39-710405.1	053130.36-710404.80	C	GDC II

As in my study, GC09 examined each candidate based on its brightness, source morphology, SED, and location in color magnitude space. They additionally examined each candidate based on its surrounding environment, its location with respect to molecular clouds and Hα emission specifically. Through this examination, they assigned each candidate a "definite", "probable", and 'possible" designation, just as in the current study. Out of the 27 GC09 YSO candidates, I determine 25 of them to be candidates. I determined one GC09 YSO candidate to be a galaxy. GC09 had classified it as a "probable" candidate and a "possible" galaxy.

Out of the 22 candidates that GC09 determined to be 'definite", I determined 16 of them to also be 'definite". Three of these I also classified as being multiples. One of these GC09 'definite" candidates was not in my survey. This source is not found in my initial IR point source catalog. This is likely due to the fact that the GC09 survey and this survey used different point source detection criteria. So it is not surprising that one survey would find point sources that the other survey would not. I determined three of the GC09 "definite" candidates to be "probable" YSO candidates and two of them to be "possible" YSO candidates.

GC09 determined five of their YSO candidates to be "probable" YSOs. Out of these, I determined one to be a "probable" YSO, three to be "possible" YSOs, and one to be a galaxy. In my classification, this source was classified as a galaxy based on the J- and K-band images, which have higher angular resolution than the *Spitzer* images. GC09 only had these measurements for certain areas of the LMC, and they did not have J- and K-band measurements for this source, or they would have likely classified it as a galaxy as well.

The 24 YSO candidates identified in this survey that are not in the GC09 candidate list were also not included in their list of infrared point sources, so they weren't even considered. They likely missed them because of the different point source detection parameters used. I used a lower threshold of detection than they did, allowing me to find sources that were on a

bright background or were near other bright sources. This allowed me to "go deeper", which I could do since I was dealing with a smaller region than the entire LMC.

Based on the findings of my study, the GC09 survey of N206 appears more accurate than the survey done by W08, but my current survey looks more complete than both previous surveys in its identification of YSO candidates. This is not surprising, since I had a much smaller region to work with and could invest more time in distinguishing features of individual point sources.

5.2.3 YSOs Identified by Romita et al. (2010)

Surprisingly, the YSO survey in N206 that seems to differ the most from mine is the one performed by Romita et al. (2010) [26] (hereafter called R10). This is surprising because R10 searched for YSOs in only the N206 region and not in the rest of the LMC. R10 report 116 YSO candidates in the N206 complex. These sources are given in Table 5.3. The table lists the candidates by the name assigned by R10. Also in the table are the name (ID) I assigned each candidate, the classification given by R10, and the classification given by myself. R10 fit YSO candidate SEDs to the Robitaille et al. models for YSO SEDs, and R10 assigned a classification based on the best-fit model. In the 'R10 Class.' column of Table 5.3, a classification of "UN"was given to four candidates. These candidates were well-fit by a wide range of YSO models and are considered unclassified YSO candidates by R10.

Table 5.3. N206 YSOs Identified by Romita et al. (2010)

R10 ID	Buehler ID	R10 Class.	Buehler Class.	Comments
Y023	– –	III	– –	
Y030	052938.47-705520.64	I	G	
Y033	052938.38-710042.12	I/II	GC I/II	
Y034	053020.40-705430.24	I	C I/II	
Y038	– –	I	– –	no R10 [8.0 μm] flux
Y039	– –	I	– –	
Y043	– –	I	– –	
Y046	– –	I	– –	no R10 [8.0 μm] flux
Y048	– –	t/mult.	– –	
Y061	053124.31-710735.76	I	C mult. II	no R10 [8.0 μm] flux
Y062	– –	t/mult.	– –	no R10 [8.0 μm] flux
Y066	052958.56-710844.88	I	C II	no R10 [8.0 μm] flux
Y071	– –	II	– –	no R10 [8.0 μm] flux
Y078	– –	II	– –	no R10 [8.0 μm] flux
Y081	– –	I	– –	no R10 [8.0 μm] flux
Y085	– –	t/mult.	– –	no R10 [8.0 μm] flux
Y091	– –	I	– –	
Y101	– –	I/II	– –	
Y102	– –	t/mult.	– –	no R10 [8.0 μm] flux
Y104	– –	I	– –	
Y106	– –	I	– –	no R10 [8.0 μm] flux
Y108	– –	I	– –	no R10 [8.0 μm] flux
Y115	– –	I	– –	no R10 [8.0 μm] flux
Y116	– –	I	– –	
Y124	– –	II	– –	
Y131	053022.46-710742.96	I	C I	
Y137	– –	I/II	– –	no R10 [8.0 μm] flux
Y139	053123.57-710735.40	I	C mult. I	
Y142	– –		– –	no R10 [8.0 μm] flux
Y152	– –	I	– –	no R10 [8.0 μm] flux
Y155	– –	II	– –	no R10 [8.0 μm] flux
Y162	052935.23-710856.76	I	C II/III	

Table 5.3 (continued)

R10 ID	Buehler ID	R10 Class.	Buehler Class.	Comments
Y196	– –	I	– –	
Y201	– –	I	– –	no R10 [8.0 μm] flux
Y202	– –	I	– –	
Y203	– –	II	– –	
Y206	– –	I	– –	
Y208	– –	I	– –	no R10 [8.0 μm] flux
Y209	– –	I/II	– –	
Y211	– –	II	– –	
Y214	– –	II	– –	
Y222	– –	I	– –	
Y226	– –	II	– –	
Y227	– –	I	– –	
Y232	– –	I	– –	
Y234	– –	II	– –	
Y237	– –	II	– –	
Y239	– –	II	– –	
Y240	– –	t/mult.	– –	
Y243	– –	III	– –	
Y244	– –	II	– –	
Y248	– –	II	– –	
Y249	– –	t/mult.	– –	
Y251	– –	t/mult.	– –	
Y252	– –	I	– –	
Y258	– –	I	– –	
Y259	– –	I	– –	
Y260	– –	I	– –	
Y264	– –	I/II	– –	
Y266	– –	I/II	– –	
Y267	– –	t/mult.	– –	
Y268	– –	I/II	– –	
Y269	– –	III	– –	
Y271	– –	I	– –	

Table 5.3 (continued)

R10 ID	Buehler ID	R10 Class.	Buehler Class.	Comments
Y272	– –	I/II	– –	
Y273	– –	I/II	– –	
Y277	– –	I	– –	
Y278	053105.62-710700.48	I/II	C I/II	
Y280	– –	t/mult.	– –	
Y285	– –	t/mult.	– –	
Y286	– –	t/mult.	– –	
Y288	– –	I/II	– –	
Y289	053104.20-710735.76	I	CSD I/II	
Y291	– –	t/mult.	– –	
Y297	– –	I	– –	
Y302	– –	I/II	– –	
Y308	– –	I	– –	
Y313	– –	III	– –	
Y314	– –	t/mult.	– –	
Y319	– –	II	– –	
Y320	– –	I/II	– –	
Y325	– –	III	– –	
Y326	– –	I	– –	
Y327	– –	I	– –	
Y329	– –	I	– –	
Y333	– –	t/mult.	– –	
Y336	– –	II	– –	
Y340	– –	II	– –	
Y344	– –	II	– –	
Y346	– –	I	– –	
Y350	– –	I	– –	
Y354	– –	I	– –	
Y358	– –	II/III	– –	
Y359	– –	III	– –	
Y375	– –	II/III	– –	
Y376	– –	I	– –	

Table 5.3 (continued)

R10 ID	Buehler ID	R10 Class.	Buehler Class.	Comments
Y379	NIR	UN	– –	
Y380	– –	I	– –	
Y383	NIR	I	– –	
Y385	– –	I/II	– –	
Y386	– –	I/II	– –	
Y389	– –	II	– –	
Y398	– –	II	– –	
Y400	NIR	I	– –	
Y401	NIR	UN	– –	
Y404	NIR	UN	– –	
Y405	– –	II/III	– –	
Y408	– –	II	– –	
Y409	NIR	I	– –	
Y411	– –	UN	– –	
Y418	NIR	I/II	– –	
Y420	NIR	III	– –	no R10 [4.5 μm] flux
Y421	NIR	I/II	– –	
Y425	NIR	I	– –	
Y426	NIR	III	– –	
Y450	053130.62-705749.32	III	G	

It is striking how many YSO candidates are not common between this survey and my survey. Out of the 116 YSO candidates of R10, I included only nine in my list of candidates. Two of the R10 YSO candidates I found to be galaxies. One of these, called Y450 by R10, I found to correspond in space to a previously identified galaxy, 2MASS J05315772-7100494. In Table 5.3, some candidates are labeled "NIR" under the 'Buehler ID' column. These candidates are not in the region of space I searched for YSOs. R10 and I searched slightly different regions surrounding the N206 complex.

For 19 of the R10 candidates, R10 does not find a flux at [8.0 μm], and for one of them

they do not find a [4.5 μm] flux. I required all of my candidates to have flux values at both [4.5 μm] and [8.0 μm], due to my color-selection criteria. I do, however, have a counterpart for one of these candidates in my catalog, as shown in the above Table, where I was able to find an [8.0 μm] flux and R10 were not.

R10 used the same color-selection criteria for their initial YSO candidates that were used by W08. They then extended it a bit, "going deeper", into areas of color-magnitude space that would include fainter and possibly more evolved YSOs. This includes the region of color-magnitude space that is dominated by background galaxies. Figure 5.10 shows the location of the R10 YSOs that have [4.5 μm] and [8.0 μm] flux measurements in the [8.0] vs. ([4.5] - [8.0]) color-magnitude diagram. It also shows the color-magnitude criteria that I applied to find my initial candidates. The wedge shows the area where I would have included candidates. As can be seen, most of the R10 candidates are below the cut that I used to exclude most background galaxies from my list of candidates. That explains why they are not included in my list.

R10 used the SAGE LMC point source catalog, just as W08 had done, to provide their initial point sources. This again excludes slightly irregular sources. R10 also likely would have used the same high signal-to-noise threshold that W08 used (because they were in collaboration), which excluded sources on bright backgrounds. This is likely why they missed several candidates that are in my list.

R10 used their color-selection criteria to find initial candidates and then fit these candidates to the same YSO models I fit my SEDs to. They only included sources in their final candidate list if they were "well-fit" to the model SEDs. They did not assess each source individually beforehand, looking at source morphology, etc., as I did. Figure 5.11 shows the spatial distribution of YSO candidates found by R10. There may be a slightly higher concentration of YSO candidates along the dusty ridges shown in red, green, and blue, the candidates mostly appear to be fairly evenly distributed around the N206 region. There are

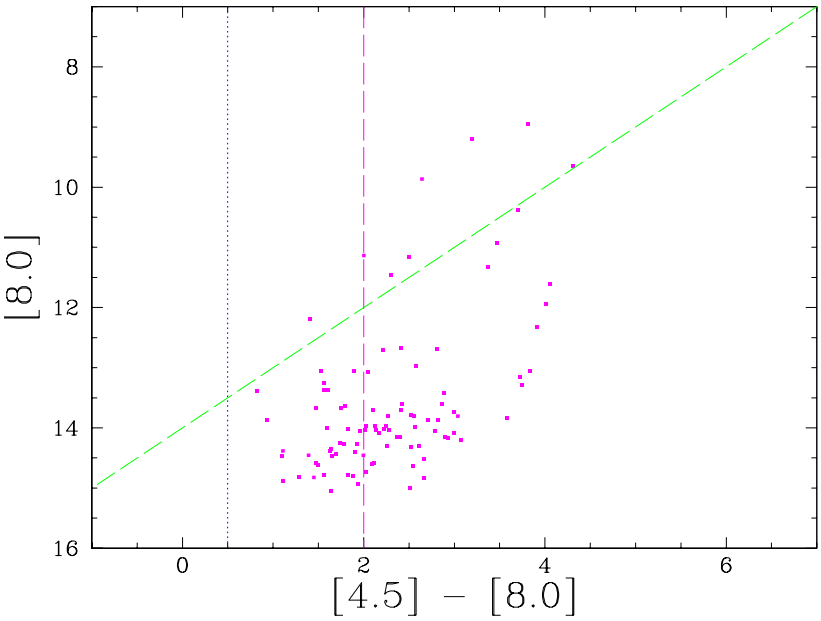

Figure 5.10 My Color-Selection Criteria for Finding Initial YSOs applied to the YSO Candidates Identified by Romita et al. (2010).

candidates seemingly randomly distributed through areas with little or no Hα emission and in regions where there are not giant molecular clouds. It is difficult to see any clear pattern of star-formation propagation in this figure.

R10 do say that there is a possibility that many of their sources not located within the dusty regions could be background galaxies. Their spatial distribution of YSOs does appear to be what would be expected from a background galaxy distribution. I think there is a risk that the SEDs of background galaxies could be "well-fit" by the YSO models, especially since R10 only had at most 8 data points to fit 14 parameters. I think they may have relied too heavily on the model fitter and that there is great merit in individual assessment of sources. I conclude, therefore, that my study would likely include many fewer false positives that the survey done by R10 and is an improvement over all three past surveys of YSOs in N206.

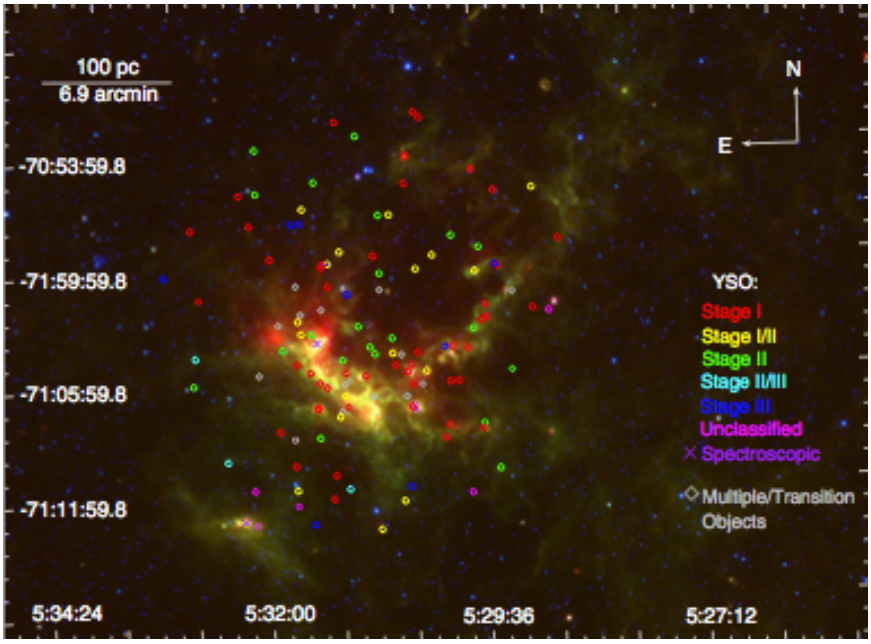

Figure 5.11 Spatial Distribution of YSO Candidates Found by Romita et al. (2010) in N206.

Chapter 6

Future Research Possibilities

6.1 N206 as Part of LMC-9

N206 is in a region of the LMC called LMC-9. LMC-9 contains other H II complexes as well: N198, N199/200, N204, and N205 (shown in Figure 6.1). LMC-9 has been classified as a supergiant shell, created by several expanding bubbles from supernovae over time. The idea of it being one coherent shell has been debated lately. I would like to extend my survey to the other H II complexes in LMC-9, to better understand this region. I would like to apply the same techniques as I have in N206 to find YSO candidates and look at their spatial distributions in the complexes to determine how star formation may be triggered. I could look for common patterns in star-formation triggering among the H II complexes of LMC-9.

I may be able to characterize the current star-formation rate for each of the H II complexes inside the LMC-9 region by comparing the masses, types, and spatial distributions of the candidate YSOs found in each region. To calculate the current star-formation rate, I should be able to estimate the total mass derived from theory for all of the YSOs in a given region and divide this mass by a formation timescale. This approach was used by Whitney et al. (2008) [33]to determine the star-formation rate for the entire LMC. In that study, they

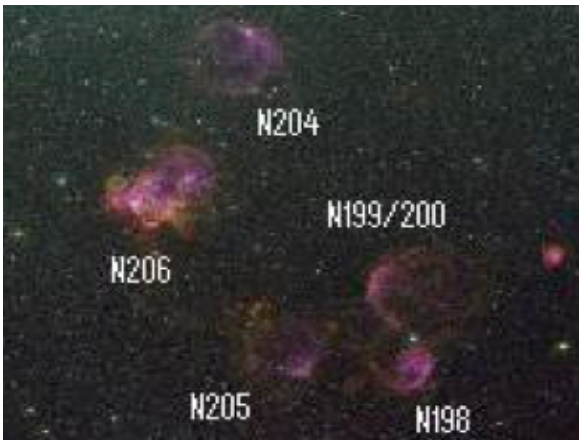

Figure 6.1 H II Complexes in the LMC-9 Supergiant Shell.

derived a formation timescale of about 2 x 10^5 years. This timescale was derived using candidate YSOs that are quite young and relatively massive. If my searches continue to be biased toward massive YSOs as well, I can use a similar timescale. Otherwise I will need to derive a new one.

If I can estimate the mass of the remaining molecular gas in the LMC-9 regions, I may also be able to estimate the efficiency of star-formation in each of these regions. In this case, I would divide the total YSO mass in a region by the mass of the remaining molecular gas. This technique was also used by Whitney et al. (2008) [33] for the entire LMC. I can use the results to examine whether the efficiency of star formation (as well as the rate of star formation) varies for different H II regions within LMC-9. I could then attempt to explain any variations that I do find between the different regions.

Finally, I can examine the H I gas kinematics using Australian Telescope Compact Array (ATCA) observations that have been constructed into an H I data cube by Kim et al. (2003) [58]. The motion and velocity of the H I gas in the environments surrounding the YSOs will help further determine if dynamic triggering of star formation is occurring in these regions. I can also look at the LMC-9 region on a larger scale to see if the H I kinematics suggest that any of the H II regions are somehow associated with one another.

6.2 Find Low-Mass YSOs

An important component of the star-formation properties of a galaxy is the mass function for YSOs. This tells how the YSOs are distributed in mass. We can't know this without being able to identify low-mass YSOs. Low-mass YSOs are difficult to distinguish from background galaxies in color-magnitude space, so most YSO surveys of the LMC have so far been biased toward high- and intermediate-mass YSOs. I would like to extend my search for YSOs into the region of color-magnitude space that background galaxies dominate to look for candidate low-mass YSOs. High-resolution spectra and images of low0mass YSOs could help distinguish them from background galaxies. Additionally, Hintz (1995) [59] found a method of distinguishing stellar sources from galaxies based on their magnitudes and angular sizes in *B, V,* and *I* flux measurements. It would be interesting to explore this technique to see if it helps to distinguish candidate low-mass YSOs from background galaxies. We could also see if this relation holds in infrared measurements. I think finding low-mass YSOs in the LMC and completing the YSO mass function is going to be a next big step in studying the star-formation properties of this galaxy.

Bibliography

[1] R. A. Gruendl and Y.-H. Chu, "High- and Intermediate-Mass Young Stellar Objects in the Large Magellanic Cloud," ApJS **184,** 172 (2009).

[2] C.-H. R. Chen, Y.-H. Chu, R. A. Gruendl, K. D. Gordon, and F. Heitsch, "Spitzer View of Young Massive Stars in the Large Magellanic Cloud H II Complex N 44," ApJ **695,** 511 (2009).

[3] M. W. Werner and coauthors, "The Spitzer Space Telescope Mission," The Astrophysical Journal Supplement Series **154,** 1–9 (2004).

[4] C. J. Lada, "Star Formation: From OB Associations to Protostars," IAUS **115,** 1L (1987).

[5] R. B. Larson, "Turbulence and Star Formation in Molecular Clouds," Royal Astronomical Society, Monthly Notices **194,** 809–826 (1981).

[6] L. Blitz and J. P. Williams, "Molecular Clouds (A Review)," presented at the 2nd Crete Conference: The Physics of Star Formation and Early Stellar Evolution (March 1999).

[7] B. G. Elmegreen and J. Scalo, "Interstellar Turbulence I: Observations and Processes," Annual Review of Astronomy & Astrophysics **42,** 211–273 (2004).

[8] C. Melioli, E. M. de Gouveia Dal Pino, R. de La Reza, and A. Raga, "Star Formation Triggered by SN Explosions: An Application to the Stellar Association of Beta Pictoris," MNRAS **373,** 811–818 (2006).

[9] J. P. Williams, L. Blitz, and C. F. McKee, "The Structure and Evolution of Molecular Clouds: From Clumps to Cores to the IMF," arXiv (May 2000).

[10] V. G. Ortega, R. de la Reza, E. Julinski, and B. Bazzanella, "New Aspects of the Formation of the Beta Pictoris Moving Group," ApJ **609,** 243–246 (2004).

[11] C. F. McKee and E. C. Ostriker, "Theory of Star Formation," Annu. Rev. Astron. Astrophys. **45,** 565–687 (2007).

[12] D. R. Alves, "A Review of the Distance and Structure of the Large Magellanic Cloud," New Astronomy Reviews **48,** 659–665 (2004).

[13] H. Zhao and N. W. Evans, "The So-Called "Bar" in the Large Magellanic Cloud," ApJ **545,** L35–L38 (2000).

[14] A. Subramaniam and S. Subramanian, "The Mysterious Bar of the Large Magellanic Cloud: What Is It?," ApJ Letters **703,** L37–L40 (2009).

[15] K. Bekki and M. Chiba, "Formation and Evolution of the Magellanic Clouds-I. Origin of Structural, Kinematic, and Chemical Properties of the Large Magellanic Cloud," MNRAS **356,** 680–702 (2005).

[16] C. Mastropietro, A. Burkert, and B. Moore, "Ram-Pressure Induced Star Formation in the LMC," Publications of the Astronomical Society of Australia **25,** 138–148 (2008).

[17] K. Glatt, E. K. Grebel, and A. Koch, "Ages and Luminosities of Young SMC/LMC Star Clusters and the Recent Formation History of the Clouds," A&A **517,** 50G (2010).

[18] C. Mastropietro, B. Moore, L. Mayer, J. Wadsley, and J. Stadel, "The Gravitational and Hydrodynamical Interaction Between the Large Magellanic Cloud and the Galaxy," MNRAS **363,** 509–520 (2005).

[19] L. Girardi, C. Chiosi, G. Bertelli, and A. Bressan, "Age Distribution of LMC Clusters From Their Integrated UBV Colors: History of Star Formation," A&A **298,** 87G (1995).

[20] G. Pietrzynski and A. Udalski, "The Optical Gravitational Lensing Experiment. Ages of About 600 Star Clusters from the LMC," Acta Astronomica **50,** 337–354 (2000).

[21] E. Chiosi, A. Vallenari, E. V. Held, L. Rizzi, and A. Moretti, "Age Distribution of Young Clusters and Field Stars in the Small Magellanic Cloud," A&A **452,** 179–193 (2006).

[22] K. S. deBoer, "Bow Shock Induced Star Formation in the LMC: A Large Scale View," In *The Magellanic Clouds and Other Dwarf Galaxies, Proceedings of the Bonn/Bochum-Graduiertenkolleg Workshop*, T. R. . J. M. Braun, ed., pp. 125–128 (1998).

[23] M. J. Blondiau, J. Kerp, U. Mebold, and U. Klein, "The X-Ray Shadow in the South-East of the Large Magellanic Cloud," Astronomy and Astrophysics **323,** 585–592 (1997).

[24] E. K. Grebel and W. Brandner, "The Recent Star-Formation History of the Large Magellanic Cloud," In *The Magellanic Clouds and Other Dwarf Galaxies, Proceedings of the Bonn/Bochum-Graduiertenkolleg Workshop*, T. R. . J. M. Braun, ed., pp. 151–154 (1998).

[25] W. K. Mueller and W. D. Arnett, ApJ **210,** 670 (1976).

[26] K. A. Romita and coauthors, "Young Stellar Objects in the Large Magellanic Cloud Star-Forming Region N206," ApJ **721,** 357–368 (2010).

[27] S. Kim, M. A. Dopita, L. Staveley-Smith, and M. S. Bessell, "H I Shells in the Large Magellanic Cloud," AJ **118,** 2797 (1999).

[28] R. McCray and M. Kafatos, "Supershells and Propagating Star Formation," ApJ **317,** 190–196 (1987).

[29] G. Bertelli, M. Mateo, C. Chiosi, and A. Bressan, "The Star Formation History of the Large Magellanic Cloud," ApJ **388,** 400–414 (1992).

[30] J. A. Holtzman and coauthors, "Observations and Implications of the Star Formation History of the Large Magellanic Cloud," AJ **118,** 2262–2279 (1999).

[31] J. Harris and D. Zaritsky, "A Method for Determining the Star Formation History of a Mixed Stellar Population," ApJ Supp. **136,** 25–40 (2001).

[32] L. T. Gardiner and M. Noguchi, "N-Body Simulations of the Small Magellanic Cloud and the Magellanic Stream," MNRAS **278,** 191–208 (1996).

[33] B. A. Whitney and coauthors, "*Spitzer* SAGE Survey of the Large Magellanic Cloud. III. Star Formation and 1000 New Candidate Young Stellar Objects," AJ **136,** 18–43 (2008).

[34] R. C. Kennicutt, F. Bresolin, D. J. Bomans, G. D. Bothun, and I. B. Thompson, "Large Scale Structure of the Ionized Gas in the Magellanic Clouds," AJ **109,** 594–604 (1995).

[35] M. Meixner and coauthors, "Spitzer Survey of the Large Magellanic Cloud: Surveying the Agents of a Galaxy's Evolution (SAGE). I. Overview and Initial Results," AJ **132,** 2268M (2006).

[36] D. Zaritsky, J. Harris, I. B. Thompson, and E. K. Grebel, "The Magellanic Clouds Photometric Survey: The Large Magellanic Cloud Stellar Catalog and Extinction Map," AJ **128,** 1606 (2004).

[37] M. F. Skrutskie and coauthors, "The Two Micron All Sky Survey (2MASS)," AJ 131 (2006).

[38] K. G. Henize, "Catalogues of H-alpha Emission Stars and Nebulae in the Magellanic Clouds," ApJS **2,** 315 (1956).

[39] L. G. Book, Y.-H. Chu, and R. A. Gruendl, "Structure of Supergiant Shells in the Large Magellanic Cloud," ApJS 175 (2008).

[40] N. JPL, "Spitzer Space Telescope," http://www.spitzer.caltech.edu (Accessed April 15, 2006).

[41] G. G. Fazio and coauthors, "The Infrared Array Camera (IRAC) for the Spitzer Space Telescope," ApJS **154,** 10F (2004).

[42] G. H. Rieke and coauthors, "The Multiband Imaging Photometer for Spitzer (MIPS)," ApJS **154,** 25 (2004).

[43] R. C. Smith and the MCELS Team, "The UM/CTIO Magellanic Cloud Emission-line Survey," In *New Views of the Magellanic Clouds, IAU Symposium # 190*, J. H. . D. B. Y.-H. Chu, N. Suntzeff, ed., p. 28 (Brigham Young University, Provo, UT, 1999).

[44] Y. Fukui, N. Mizuno, R. Yamaguchi, A. Mizuno, and T. Onishi, "On the Mass Spectrum of Giant Molecular Clouds in the Large Magellanic Cloud," PASJ **53L,** 41F (2001).

[45] P. M. Harvey and coauthors, "The Spitzer c2d Survey of Large, Nearby, Interstellar Clouds. II. Serpens Observed with IRAC," ApJ **644,** 307H (2006).

[46] M. A. T. Groenewegen, "The Mid- and Far-Infrared Colours of AGB and Post-AGB Stars," A&A **448,** 181 (2006).

[47] C. J. Lonsdale and coauthors, "SWIRE: The SIRTF Wide-Area Infrared Extragalactic Survey," PASP **115,** 897 (2003).

[48] J. A. Surace and coauthors, *The SWIRE ELAIS N1 Image Atlases and Source Catalogs* (Spitzer Science Center, Pasadena, 2004).

[49] W. A. Joye and E. Mandel, "New Features of SAOImage DS9," Astronomical Data Analysis Software and Systems XII ASP Conference Series **295,** 489 (2003).

[50] M. Rowan-Robinson and coauthors, "Spectral Energy Distributions and Luminosities of Galaxies and Active Galactic Nuclei in the Spitzer Wide-Area Infrared Extragalactic (SWIRE) Legacy Survey," AJ **129,** 1183 (2005).

[51] T. P. Robitaille, B. A. Whitney, R. Indebetouw, K. Wood, and P. Denzmore, "Interpreting Spectral Energy Distributions From Young Stellar Objects I," ApJ 167 (2006).

[52] N. Mizuno and coauthors, "A CO Survey of the LMC with NANTEN: II. Catalog of Molecular Clouds," PASJ **53,** 971M (2001).

[53] B. G. Elmegreen and C. J. Lada, "Sequential Formation of Subgroups in OB Associations," ApJ **214,** 725 (1977).

[54] R. Behrend and A. Maeder, "Formation of Massive Stars by Growing Accretion Rate," Astronomy and Astrophysics **373,** 190 (2001).

[55] V. Gorjian and coauthors, "Infrared Imaging of the Large Magellanic Cloud Star-Forming Region Henize 206," ApJS **154,** 275–280 (2004).

[56] K. M. Desai and coauthors, "Supernova Remnants and Star Formation in the Large Magellanic Cloud," AJ **140,** 584 (2010).

[57] R. M. Williams and coauthors, "Supernova Remnants in the Magellanic Clouds. V. The Complex Interior Structure of the N206 Supernova Remnant," ApJ **628,** 704 (2005).

[58] S. Kim and coauthors, "A Neutral Hydrogen Survey of the Large Magellanic Cloud: Aperture Synthesis and Multibeam Data Combined," ApJS **148,** 473 (2003).

[59] E. G. B. Hintz, "Multicolor, Two-Dimensional Photometric Study of Galaxies in Rich Abell Clusters," Ph.D. dissertation (Brigham Young University, Provo, UT, 1995).

[60] E. Kontizas and coauthors, "A Catalogue of Carbon Stars in the LMC," A&A **369,** 932 (2001).

Appendix A

Candidate Spectral Energy Distributions

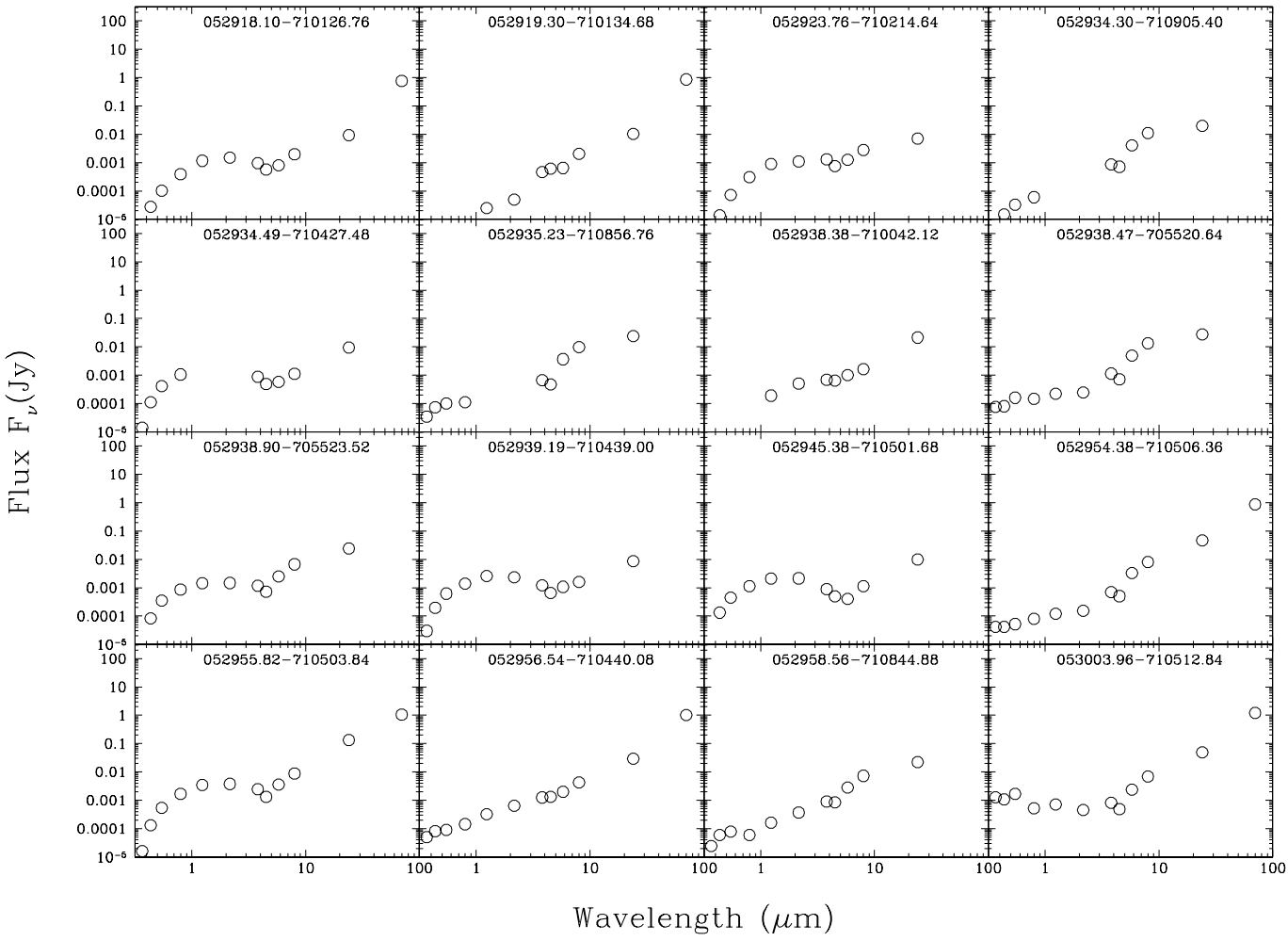

Figure A.1 Spectral energy distributions for candidate young stellar objects.

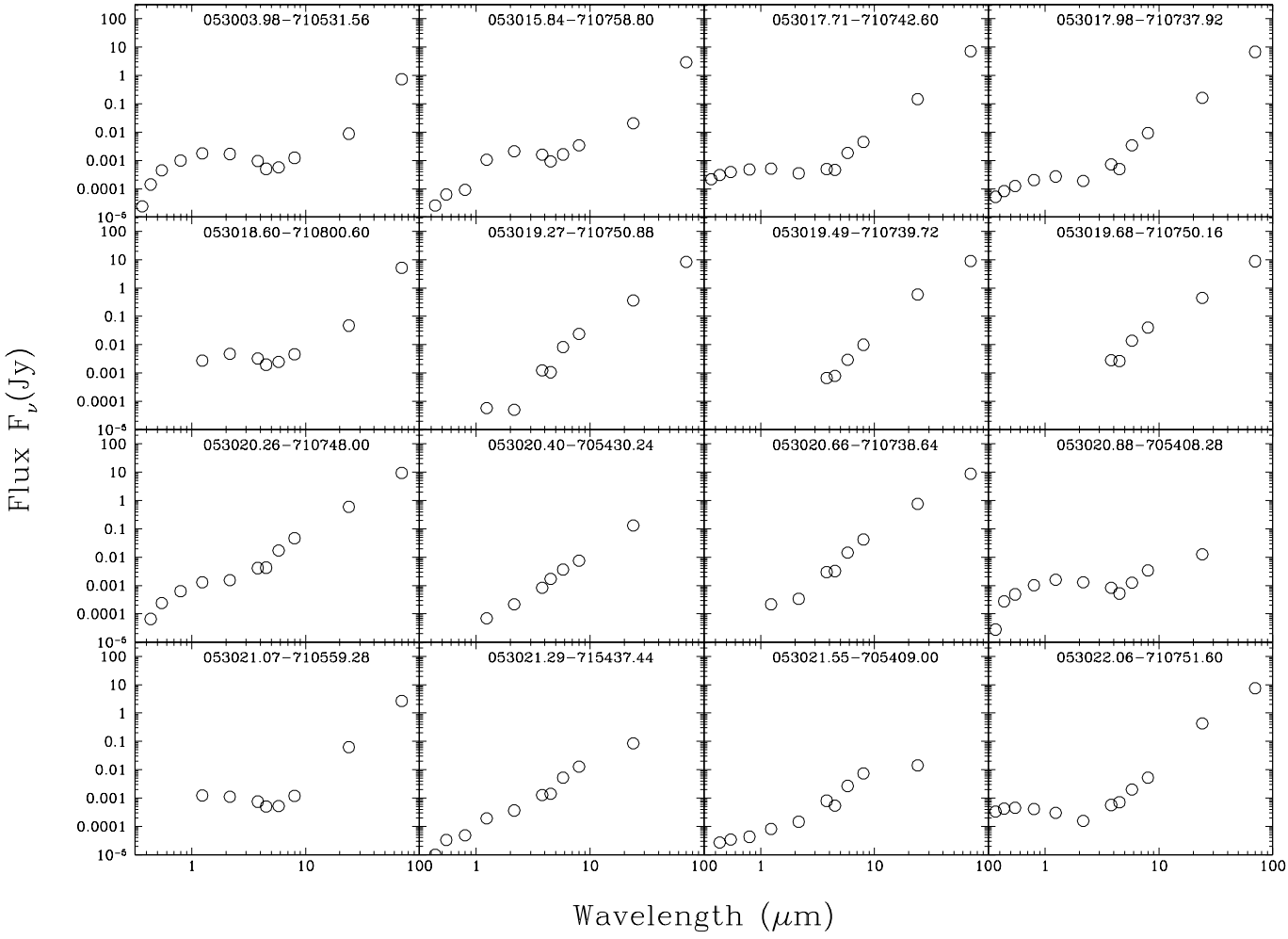

Figure A.2 Spectral energy distributions for candidate young stellar objects. Continued from previous figure.

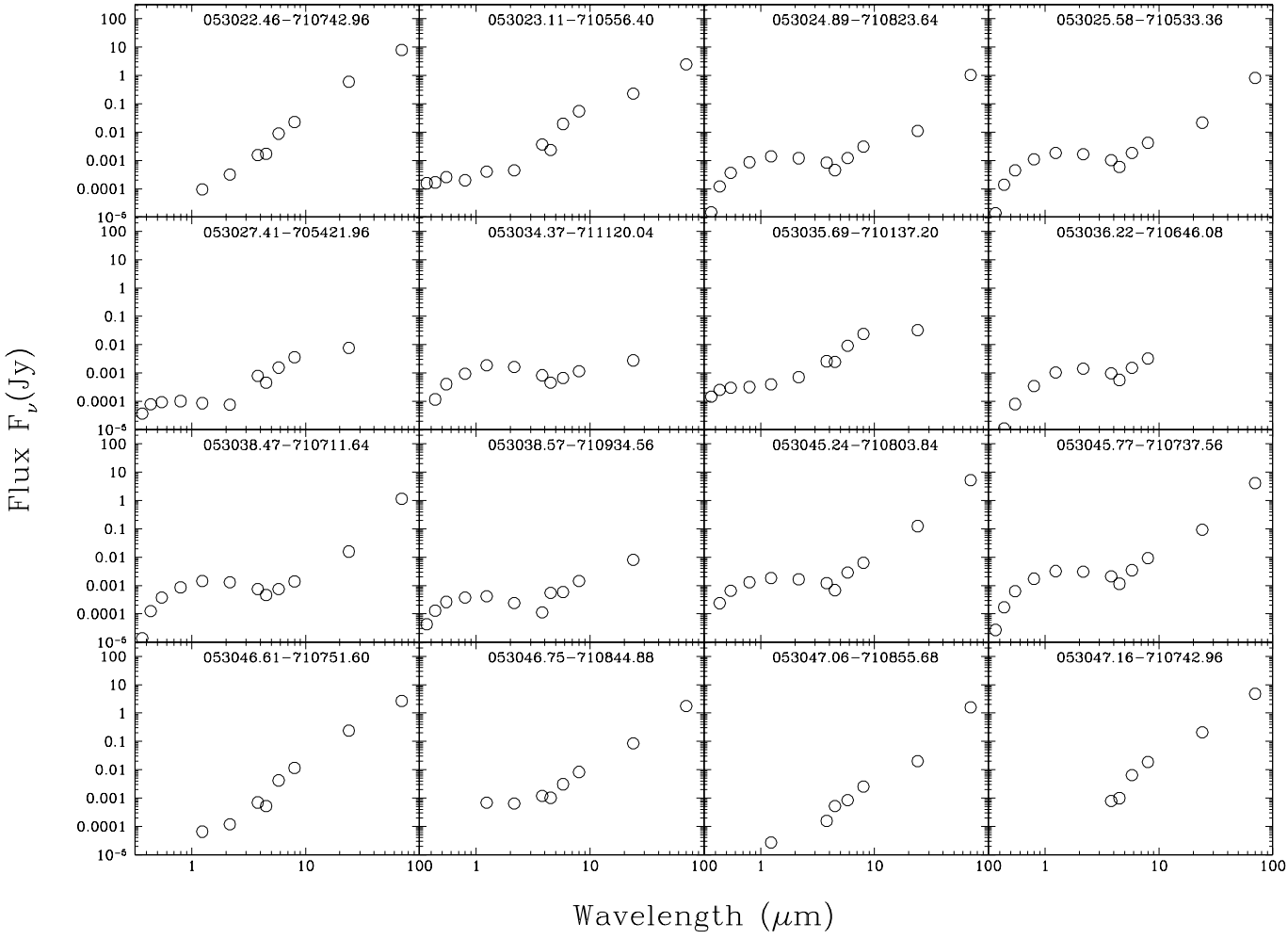

Figure A.3 Spectral energy distributions for candidate young stellar objects. Continued from previous figure.

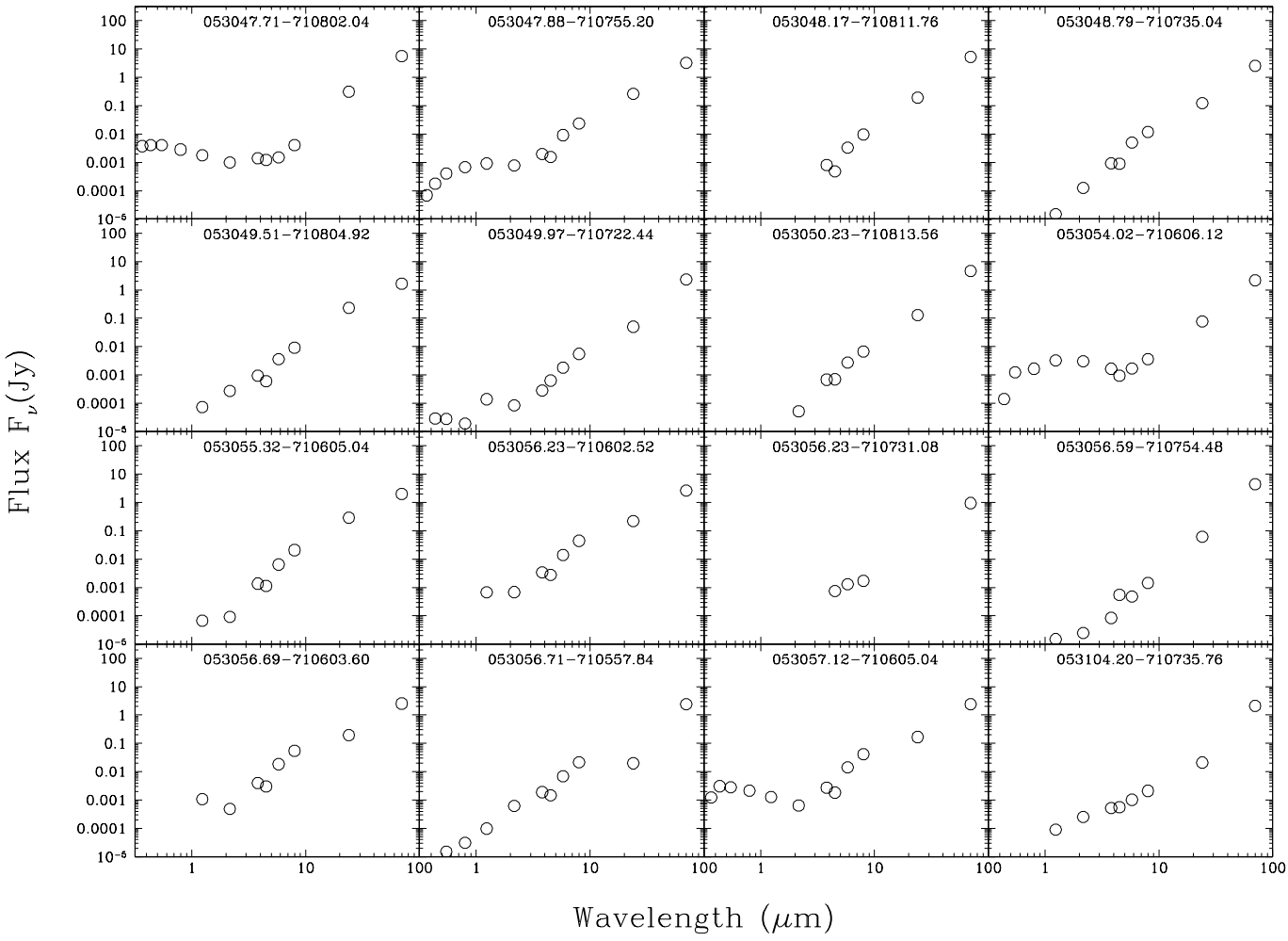

Figure A.4 Spectral energy distributions for candidate young stellar objects. Continued from previous figure.

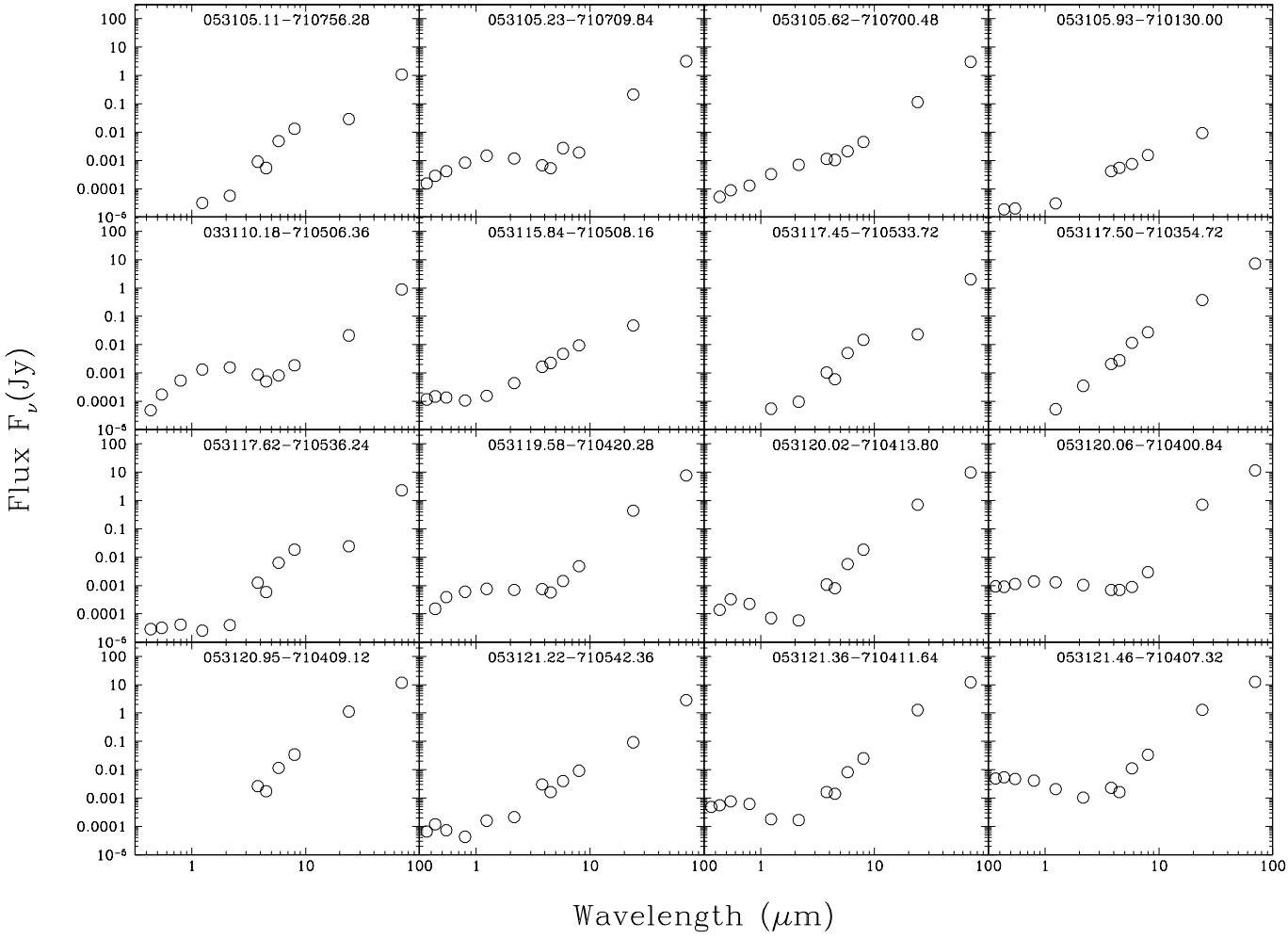

Figure A.5 Spectral energy distributions for candidate young stellar objects. Continued from previous figure.

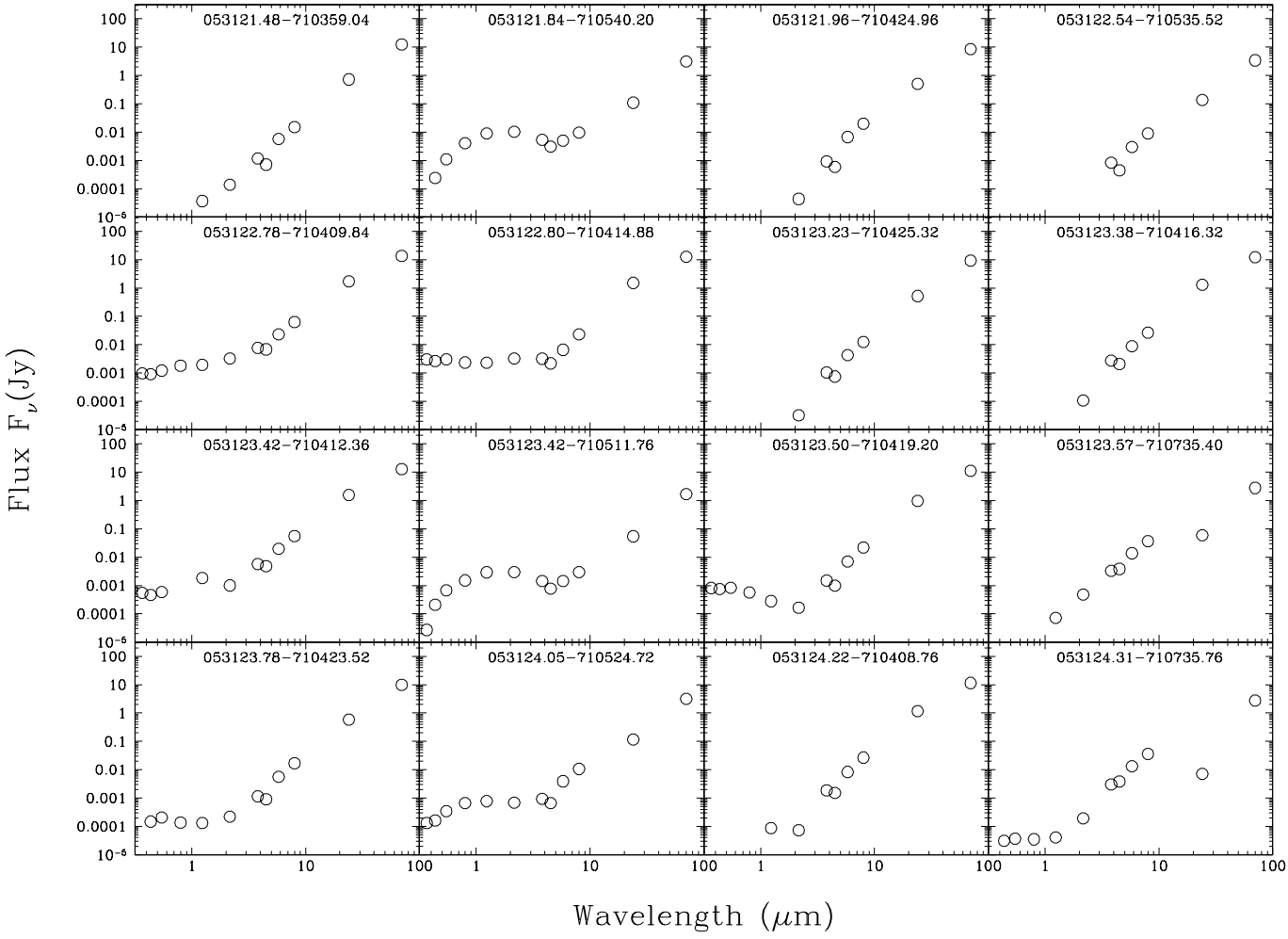

Figure A.6 Spectral energy distributions for candidate young stellar objects. Continued from previous figure.

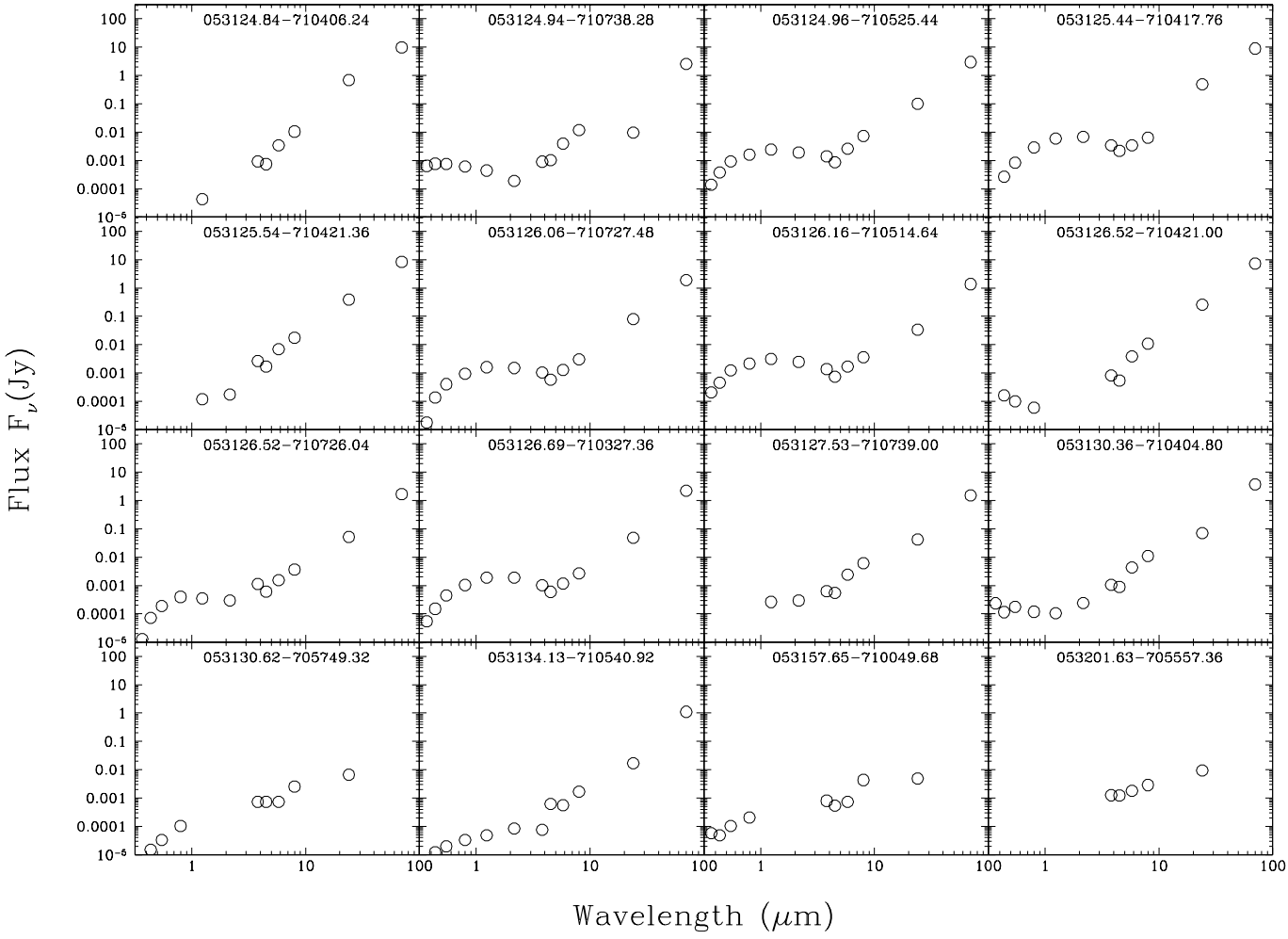

Figure A.7 Spectral energy distributions for candidate young stellar objects. Continued from previous figure.

Appendix B

Photometry of Known N206 Objects

Table B.1. Multiwavelength Photometry of Known AGB Stars in N206

Identifier	RA	Dec	U	B	V	I
(1)	(2)	(3)	(4)	(5)	(6)	(7)
			J	K	[3.6]	[4.5]
			(8)	(9)	(10)	(11)
			[5.8]	[8.0]	[24]	[70]
			(12)	(13)	(14)	(15)
KDM2001 4259	05:28:27.79	-71:01:47.40	—- —-	18.15 (0.03)	15.90 (0.02)	13.76 (0.03)
			—- —-	—- —-	10.09 (0.01)	10.02 (0.01)
			9.73 (0.01)	9.46 (0.01)	8.95 (0.05)	—- —-
KDM2001 4274	05:28:36.05	-70:59:23.20	—- —-	18.41 (0.05)	16.17 (0.03)	13.94 (0.03)
			—- —-	—- —-	10.40 (0.01)	10.57 (0.01)
			10.35 (0.01)	10.08 (0.01)	—- —-	—- —-
KDM2001 4307	05:28:56.05	-71:07:37.30	—- —-	19.32 (0.04)	17.30 (0.08)	15.43 (0.03)
			—- —-	—- —-	12.30 (0.01)	12.48 (0.01)
			12.35 (0.02)	12.04 (0.03)	10.21 (0.11)	—- —-
KDM2001 4325	05:29:08.80	-71:10:34.40	20.08 (0.16)	18.44 (0.03)	16.61 (0.02)	14.80 (0.03)
			—- —-	—- —-	11.77 (0.01)	11.96 (0.01)
			11.82 (0.02)	11.52 (0.01)	4.61 (0.01)	—- —-
KDM2001 4346	05:29:16.99	-70:56:55.40	—- —-	19.62 (0.04)	17.05 (0.03)	14.57 (0.03)
			13.02 (0.01)	11.58 (0.01)	11.04 (0.01)	11.16 (0.01)
			10.92 (0.01)	10.51 (0.01)	9.54 (0.18)	—- —-
KDM2001 4354	05:29:19.81	-71:11:37.30	—- —-	19.10 (0.04)	16.62 (0.03)	13.91 (0.03)
			—- —-	—- —-	9.84 (0.01)	10.02 (0.01)
			9.83 (0.01)	9.44 (0.01)	8.70 (0.05)	—- —-
KDM2001 4361	05:29:22.95	-70:56:34.40	—- —-	21.16 (0.12)	17.15 (0.04)	14.12 (0.03)
			12.53 (0.01)	10.78 (0.01)	10.06 (0.01)	10.28 (0.01)
			10.20 (0.01)	9.65 (0.01)	9.55 (0.10)	—- —-
KDM2001 4365	05:29:23.71	-70:56:55.40	—- —-	19.31 (0.04)	16.96 (0.03)	14.52 (0.03)
			12.81 (0.01)	11.44 (0.01)	10.98 (0.01)	11.13 (0.01)
			10.96 (0.01)	10.72 (0.01)	—- —-	—- —-
KDM2001 4431	05:29:56.97	-71:11:24.60	—- —-	19.25 (0.08)	20.62 (0.25)	14.75 (0.03)
			12.82 (0.01)	11.46 (0.01)	11.22 (0.01)	11.32 (0.01)
			11.11 (0.01)	10.89 (0.01)	—- —-	—- —-

Table B.1 (continued)

Identifier	RA	Dec	U	B	V	I
(1)	(2)	(3)	(4)	(5)	(6)	(7)
			J	K	[3.6]	[4.5]
			(8)	(9)	(10)	(11)
			[5.8]	[8.0]	[24]	[70]
			(12)	(13)	(14)	(15)
KDM2001 4433	05:29:57.38	-71:04:58.60	—- —-	19.46 (0.04)	17.33 (0.07)	14.79 (0.03)
			13.02 (0.01)	11.32 (0.01)	10.70 (0.01)	10.98 (0.01)
			10.74 (0.02)	9.90 (0.03)	4.55 (0.01)	—- —-
KDM2001 4436	05:30:00.65	-71:15:22.40	20.25 (0.20)	18.58 (0.04)	16.71 (0.02)	15.21 (0.03)
			—- —-	—- —-	12.82 (0.01)	12.84 (0.01)
			12.71 (0.03)	12.61 (0.03)	—- —-	—- —-
KDM2001 4483	05:30:22.94	-71:05:28.30	—- —-	19.39 (0.05)	16.69 (0.03)	14.08 (0.03)
			12.51 (0.01)	10.88 (0.01)	10.20 (0.01)	10.39 (0.01)
			10.13 (0.01)	9.59 (0.01)	6.93 (0.04)	—- —-
KDM2001 4508	05:30:32.87	-71:00:56.00	—- —-	19.06 (0.05)	16.26 (0.03)	13.55 (0.03)
			11.75 (0.01)	10.21 (0.01)	9.74 (0.01)	9.92 (0.01)
			9.76 (0.01)	9.33 (0.01)	9.19 (0.08)	—- —-
KDM2001 4522	05:30:41.77	-70:50:35.7	20.73 (0.16)	18.66 (0.04)	16.45 (0.03)	14.51 (0.03)
			—- —-	—- —-	11.47 (0.01)	11.60 (0.01)
			11.40 (0.01)	11.30 (0.01)	—- —-	—- —-
KDM2001 4533	05:30:49.83	-71:03:24.30	19.04 (0.09)	17.97 (0.03)	16.14 (0.03)	13.88 (0.03)
			12.43 (0.01)	11.08 (0.01)	10.63 (0.01)	10.78 (0.01)
			10.44 (0.01)	10.23 (0.01)	7.95 (0.07)	—- —-
KDM2001 4582	05:31:17.29	-70:52:22.20	—- —-	19.60 (0.05)	17.05 (0.03)	14.28 (0.03)
			—- —-	—- —-	10.03 (0.01)	10.26 (0.01)
			10.19 (0.01)	9.66 (0.01)	9.29 (0.05)	—- —-
KDM2001 4593	05:31:21.73	-70:58:00.20	—- —-	19.20 (0.04)	16.85 (0.03)	14.36 (0.03)
			—- —-	—- —-	10.85 (0.01)	11.07 (0.01)
			10.94 (0.01)	10.57 (0.01)	9.53 (0.10)	—- —-
KDM2001 4618	05:31:33.61	-71:10:43.50	—- —-	20.37 (0.08)	17.01 (0.03)	14.17 (0.05)
			12.48 (0.01)	10.75 (0.01)	10.20 (0.01)	10.42 (0.01)
			10.35 (0.01)	9.80 (0.01)	9.32 (0.05)	—- —-

Table B.1 (continued)

Identifier	RA	Dec	U	B	V	I
(1)	(2)	(3)	(4)	(5)	(6)	(7)
			J	K	[3.6]	[4.5]
			(8)	(9)	(10)	(11)
			[5.8]	[8.0]	[24]	[70]
			(12)	(13)	(14)	(15)
KDM2001 4635	05:31:43.21	-71:04:32.40	—- —-	17.97 (0.06)	16.10 (0.03)	13.88 (0.03)
			12.12 (0.01)	10.79 (0.01)	10.42 (0.01)	10.56 (0.01)
			10.43 (0.01)	10.35 (0.01)	7.69 (0.17)	—- —-
KDM2001 4663	05:31:56.78	-71:10:59.10	—- —-	20.71 (0.08)	16.94 (0.03)	13.88 (0.03)
			12.07 (0.01)	10.24 (0.01)	9.57 (0.01)	9.76 (0.01)
			9.63 (0.01)	9.00 (0.01)	8.62 (0.02)	—- —-
KDM2001 4673	05:32:00.78	-70:54:07.30	—- —-	19.56 (0.05)	17.19 (0.05)	14.75 (0.03)
			—- —-	—- —-	10.93 (0.01)	11.04 (0.01)
			10.77 (0.01)	10.50 (0.01)	10.25 (0.13)	—- —-
KDM2001 4678	05:32:04.81	-71:10:10.60	20.31 (0.25)	18.80 (0.04)	16.57 (0.03)	14.33 (0.03)
			12.65 (0.01)	11.22 (0.01)	10.92 (0.01)	11.04 (0.01)
			10.86 (0.01)	10.62 (0.01)	7.24 (0.01)	—- —-
KDM2001 4692	05:32:10.29	-71:03:28.70	—- —-	19.10 (0.09)	16.53 (0.04)	13.87 (0.03)
			—- —-	—- —-	9.99 (0.01)	10.14 (0.01)
			10.03 (0.01)	9.55 (0.01)	—- —-	—- —-
KDM2001 4708	05:32:22.35	-70:55:02.80	—- —-	21.20 (0.21)	17.86 (0.09)	14.89 (0.03)
			—- —-	—- —-	10.41 (0.01)	10.61 (0.01)
			10.51 (0.01)	9.92 (0.01)	10.01 (0.09)	—- —-
KDM2001 4716	05:32:25.55	-70:52:04.90	—- —-	19.93 (0.05)	16.20 (0.05)	13.29 (0.04)
			—- —-	—- —-	9.13 (0.01)	9.20 (0.01)
			9.07 (0.01)	8.58 (0.01)	8.18 (0.02)	—- —-
KDM2001 4805	05:33:13.63	-71:02:47.40	19.90 (0.20)	19.30 (0.04)	16.83 (0.03)	14.16 (0.03)
			—- —-	—- —-	9.81 (0.01)	9.76 (0.01)
			9.29 (0.01)	8.34 (0.01)	7.12 (0.01)	—- —-
KDM2001 4809	05:33:14.89	-71:04:06.50	19.55 (0.12)	18.83 (0.04)	17.85 (0.13)	—- —-
			—- —-	—- —-	9.34 (0.01)	9.42 (0.01)
			9.39 (0.01)	8.80 (0.01)	8.56 (0.02)	—- —-

Table B.1 (continued)

Identifier	RA	Dec	U	B	V	I
(1)	(2)	(3)	(4)	(5)	(6)	(7)
			J	K	[3.6]	[4.5]
			(8)	(9)	(10)	(11)
			[5.8]	[8.0]	[24]	[70]
			(12)	(13)	(14)	(15)
KDM2001 4885	05:34:03.89	-71:02:12.10	—- —-	19.47 (0.04)	16.99 (0.03)	14.41 (0.12)
			—- —-	—- —-	10.76 (0.01)	10.89 (0.01)
			10.74 (0.01)	10.40 (0.01)	10.45 (0.15)	—- —-

Note. — Column (1): identifier from SIMBAD database (KDM2001 refers to the catalogue of carbon stars in the LMC published by [60]), Columns (2) & (3): RA and Dec coordinates, Columns (4)-(15): photometric magnitudes (and errors) of 12 wavelengths from U to 70 μm. Any magnitude error of < 0.01 was rounded to a value 0.01.

Table B.2. Multiwavelength Photometry of Known Galaxies in N206

Identifier	RA	Dec	U	B	V	I
(1)	(2)	(3)	(4)	(5)	(6)	(7)
			J	K	[3.6]	[4.5]
			(8)	(9)	(10)	(11)
			[5.8]	[8.0]	[24]	[70]
			(12)	(13)	(14)	(15)
2MASS J05263354-7053498	05:26:33.55	-70:53:49.82	— —	20.53 (0.08)	19.27 (0.13)	17.90 (0.10)
			— —	— —	13.80 (0.02)	13.60 (0.02)
			13.43 (0.07)	10.75 (0.02)	7.90 (0.01)	— —
GC2009 J052803.02-711513.6	05:28:03.02	-71:15:13.60	— —	21.68 (0.18)	20.73 (0.08)	20.32 (0.15)
			— —	— —	14.28 (0.02)	13.60 (0.02)
			12.62 (0.04)	11.48 (0.02)	7.98 (0.02)	— —
2MFGC 4459	05:28:10.47	-71:42:50.25	— —	18.94 (0.11)	17.45 (0.17)	— —
			— —	— —	13.41 (0.02)	13.47 (0.04)
			12.62 (0.04)	11.37 (0.04)	8.10 (0.02)	— —
2MASSI J0530201-710748	05:30:20.07	-71:07:48.46	— —	19.46 (0.04)	17.95 (0.08)	16.45 (0.03)
			15.41 (0.03)	14.36 (0.03)	12.09 (0.02)	11.58 (0.01)
			9.54 (0.02)	7.81 (0.02)	2.77 (0.01)	-2.69 (0.11)
GC2009 J053044.89-712358.6	05:30:44.89	-71:23:58.60	19.58 (0.12)	19.98 (0.05)	19.53 (0.06)	18.83 (0.07)
			— —	— —	15.00 (0.03)	14.01 (0.02)
			12.92 (0.04)	11.89 (0.02)	7.92 (0.02)	— —
2MASSI J0531228-710413	05:31:22.90	-71:04:13.67	14.43 (0.07)	15.46 (0.04)	15.20 (0.11)	15.04 (0.10)
			14.58 (0.02)	13.30 (0.02)	11.88 (0.03)	11.63 (0.03)
			10.01 (0.07)	8.13 (0.05)	1.61 (0.01)	-3.05 (0.09)
2MASS J05313060-7057491	05:31:30.60	-70:57:49.15	— —	21.06 (0.13)	20.11 (0.08)	18.43 (0.08)
			— —	— —	13.96 (0.01)	13.49 (0.01)
			13.01 (0.02)	11.00 (0.01)	7.56 (0.01)	— —
2E 0532.3-7131[a]	05:31:32.40	-71:29:47.00	— —	20.17 (0.06)	20.05 (0.07)	— —
			— —	— —	15.91 (0.06)	15.39 (0.07)
			14.44 (0.14)	13.42 (0.11)	8.42 (0.02)	— —
GC2009 J053154.74-705056.4	05:31:54.74	-70:50:56.40	21.30 (0.33)	20.71 (0.10)	20.16 (0.10)	19.92 (0.14)
			— —	— —	14.23 (0.01)	13.72 (0.01)
			12.71 (0.02)	11.44 (0.01)	7.85 (0.01)	— —

Table B.2 (continued)

Identifier	RA	Dec	U	B	V	I
(1)	(2)	(3)	(4)	(5)	(6)	(7)
			J	K	[3.6]	[4.5]
			(8)	(9)	(10)	(11)
			[5.8]	[8.0]	[24]	[70]
			(12)	(13)	(14)	(15)
2MASS J05315646-7120308	05:31:56.47	-71:20:30.83	21.04 (0.31)	19.98 (0.06)	20.11 (0.33)	— —
			— —	— —	14.46 (0.02)	13.92 (0.02)
			13.13 (0.05)	11.46 (0.01)	7.58 (0.01)	— —
2MASS J05315772-7100494	05:31:57.72	-71:00:49.49	18.74 (0.23)	19.81 (0.13)	18.86 (0.12)	17.68 (0.11)
			— —	— —	13.84 (0.01)	13.81 (0.02)
			13.00 (0.03)	10.42 (0.01)	7.95 (0.06)	— —
GC2009 J053258.09-705112.9	05:32:58.09	-70:51:12.90	19.17 (0.06)	18.88 (0.05)	18.61 (0.06)	18.02 (0.04)
			— —	— —	14.63 (0.02)	13.73 (0.02)
			12.79 (0.03)	11.69 (0.02)	8.17 (0.02)	— —
2MASS J05341110-7106108	05:34:11.10	-71:06:10.90	— —	20.25 (0.12)	19.24 (0.09)	17.78 (0.06)
			— —	— —	13.96 (0.01)	13.87 (0.01)
			13.47 (0.03)	11.24 (0.01)	9.07 (0.04)	— —
GC2009 J053424.17-710748.4	05:34:24.17	-71:07:48.40	20.43 (0.27)	19.84 (0.08)	19.06 (0.14)	18.60 (0.20)
			— —	— —	14.34 (0.01)	13.67 (0.01)
			13.09 (0.03)	11.54 (0.01)	7.17 (0.01)	— —
2MASS J05353014-7106319	05:35:30.15	-71:06:31.91	18.87 (0.11)	19.56 (0.06)	18.28 (0.07)	17.32 (0.06)
			— —	— —	13.72 (0.01)	13.27 (0.01)
			12.62 (0.02)	10.42 (0.01)	6.51 (0.01)	— —
6dFGS gJ053543.3-710634	05:35:43.33	-71:06:34.00	18.57 (0.09)	18.34 (0.08)	18.05 (0.16)	— —
			— —	— —	12.97 (0.01)	12.97 (0.01)
			12.27 (0.03)	10.51 (0.01)	7.73 (0.02)	— —

[a] Emission-line galaxy

Note. — Column (1): identifier from SIMBAD database (GC2009 refers to Gruendl & Chu (2009) [1], who classified these objects as galaxies), Columns (2) & (3): RA and Dec coordinates, Columns (4)-(15): photometric magnitudes (and errors) of 12 wavelengths from U to 70 μm.

Index